

Biology of Human Sodium Glucose Transporters

ERNEST M. WRIGHT, DONALD D. F. LOO, AND BRUCE A. HIRAYAMA

*Department of Physiology, David Geffen School of Medicine at University of California Los Angeles,
Los Angeles, California*

I. Introduction	734
II. 1987 BC	735
III. Expression Cloning	737
A. The intestinal brush-border transporter	737
B. Stoichiometry of Na^+ to glucose transport	738
C. Reversible transport	739
IV. Genes	741
A. Chromosomal location	741
B. Gene mapping	741
C. Human gene family (SLC5)	741
D. Functional characterization	742
V. Expression	743
A. mRNA	743
B. Proteins	744
C. PET imaging	745
VI. Prokaryote SGLTs	746
VII. Structure	747
A. Amino acid sequences	747
B. Secondary structure	748
C. Monomer	749
D. Protein	749
E. Circular dichroism	749
F. Crystal structure	750
G. LeuT superfamily	751
VIII. Sugar Selectivity	752
A. Monosaccharides	752
B. Glucosides	754
C. Inhibitors	755
IX. Ion Selectivity	757
X. Kinetics	758
A. Steady-state kinetics	758
B. Pre-steady-state kinetics	761
C. Conformational dynamics	767
D. Substrate and drug interactions	768
XI. Kinetic Modeling	769
A. Model	769
B. Experimental basis	769
C. Voltage sensitivity	770
D. Estimating parameters	770
E. Testing	770
F. Distribution of conformations	771
XII. Structure and Function	773
XIII. Multifunctional Proteins	774
A. Na^+ uniport	774
B. Water and urea channels	775
C. Coupled water, urea, and glucose transport	775
D. Glucose sensor	775
E. Glucose sensing in the gut	776
F. Glucose sensing in the brain	776
XIV. Physiology and Pathophysiology	777

A. Regulation of expression	777
B. Intestinal absorption	778
C. Oral rehydration therapy	780
D. Glucose galactose malabsorption	780
E. Enteric infection	782
F. Renal reabsorption	782
G. Familial renal glucosuria	783
H. Bile, milk, and saliva	785
I. Cancer	785
J. Diabetes	786
XV. Outlook	787
XVI. Unresolved Problems	787

Wright EM, Loo DDF, Hirayama BA. Biology of Human Sodium Glucose Transporters. *Physiol Rev* 91: 733–794, 2011; doi:10.1152/physrev.00055.2009.—There are two classes of glucose transporters involved in glucose homeostasis in the body, the facilitated transporters or uniporters (GLUTs) and the active transporters or symporters (SGLTs). The energy for active glucose transport is provided by the sodium gradient across the cell membrane, the Na^+ glucose cotransport hypothesis first proposed in 1960 by Crane. Since the cloning of SGLT1 in 1987, there have been advances in the genetics, molecular biology, biochemistry, biophysics, and structure of SGLTs. There are 12 members of the human SGLT (SLC5) gene family, including cotransporters for sugars, anions, vitamins, and short-chain fatty acids. Here we give a personal review of these advances. The SGLTs belong to a structural class of membrane proteins from unrelated gene families of antiporters and Na^+ and H^+ symporters. This class shares a common atomic architecture and a common transport mechanism. SGLTs also function as water and urea channels, glucose sensors, and coupled-water and urea transporters. We also discuss the physiology and pathophysiology of SGLTs, e.g., glucose galactose malabsorption and familial renal glucosuria, and briefly report on targeting of SGLTs for new therapies for diabetes.

I. INTRODUCTION

Sodium-glucose transporters, also known as Na^+ /glucose cotransporters or symporters (SGLTs), have a historical place in the field of membrane transport. Half a century ago it was established that glucose transport across the small intestine occurred by active transport, i.e., the sugar could be absorbed uphill against its concentration gradient both *in vivo* and *in vitro*, and this uptake was blocked by metabolic poisons. Nonmetabolized glucose analogs were also actively transported, and the process was located at the brush-border membrane of the enterocytes lining the intestine. An explanation for active transport of glucose, and other molecules, was completely lacking until Bob Crane proposed the Na^+ /glucose cotransport hypothesis in 1960 at the Symposium on Membrane Transport and Metabolism in Prague (94). In this model, the energy for uphill glucose transport was provided by the sodium gradient across the brush-border membrane, and the sodium gradient was maintained by the Na^+/K^+ pump.

The model proposed by Crane is reproduced in Figure 1. It shows the brush-border membrane of the intestinal epithelium with the digestive surface and the diffusion barrier (plasma membrane). Glucose, liberated from dietary sucrose at the digestive surface, is transported across the plasma membrane by a sodium-glucose carrier complex. Glucose transport is driven by the inward Na^+ gradient maintained by the Na^+ pump. Strophanthidin inhibits the Na^+ pump causing the Na^+ gradient to dissi-

pate and remove the driving force for uphill glucose transport. Phlorizin, a plant glucoside, directly inhibits cotransport. This simple scheme accounts for “active” transport of glucose across the intestinal brush-border membrane and the requirement for energy input from the cell. The model remains valid to this day, apart from some minor details such as the site of phlorizin inhibition (extracellular) and the location of the Na^+/K^+ pump (basolateral membrane). A personal account of Crane’s road to the Na^+ /glucose cotransport hypothesis is available (26).

The cotransport hypothesis was initially not well received by physiologists, but Peter Mitchell, who was also a participant at the Prague Symposium, later generalized the concept to include both cotransport and exchange (148). He clearly recognized that coupled transport could be extended to active transport in bacteria, i.e., H^+ /sugar cotransport. Mitchell defined coupled transport as secondary active transport and coined the term *sympart* that has been retained by biochemists. Readers interested in a wider historical perspective are referred to the monograph by Robinson (184).

In the 1960s and 1970s, the Na^+ cotransport hypothesis was vigorously tested and extended to include the “active” transport of other molecules and ions, not only in the intestine and kidney but in such organs as the brain and thyroid gland (196). The active transport of ions and molecules in plants and bacteria was also demonstrated to be due to “sympart” with protons as the driving cations. As work progressed, Na^+ symporters in bacteria and H^+ symporters in mammals have been identified. The most

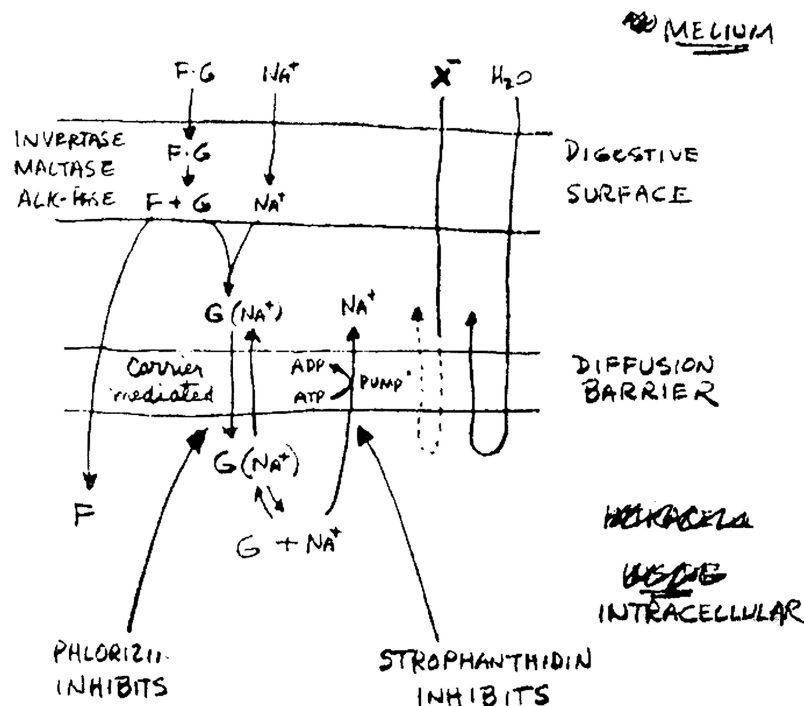


FIG. 1. The cotransport model drawn by Crane on August 24, 1960 in Prague. The redrawn figure was included in the Appendix to the presubmitted paper (23, 25). (Figure kindly provided by Bob Crane.)

convincing evidence for cotransport came with technical innovations: 1) introduction of plasma membrane vesicles ("Kabackosomes," Ref. 85). Intestinal brush-border membrane vesicles were then used to show Na⁺ gradient-driven accumulation of glucose in the intravesicular space (76). 2) The use of isolated intestinal cells directly demonstrated Na⁺-coupled glucose transport (93). These advances have been fully reviewed in this journal and elsewhere (24, 27, 75, 92, 195, 196).

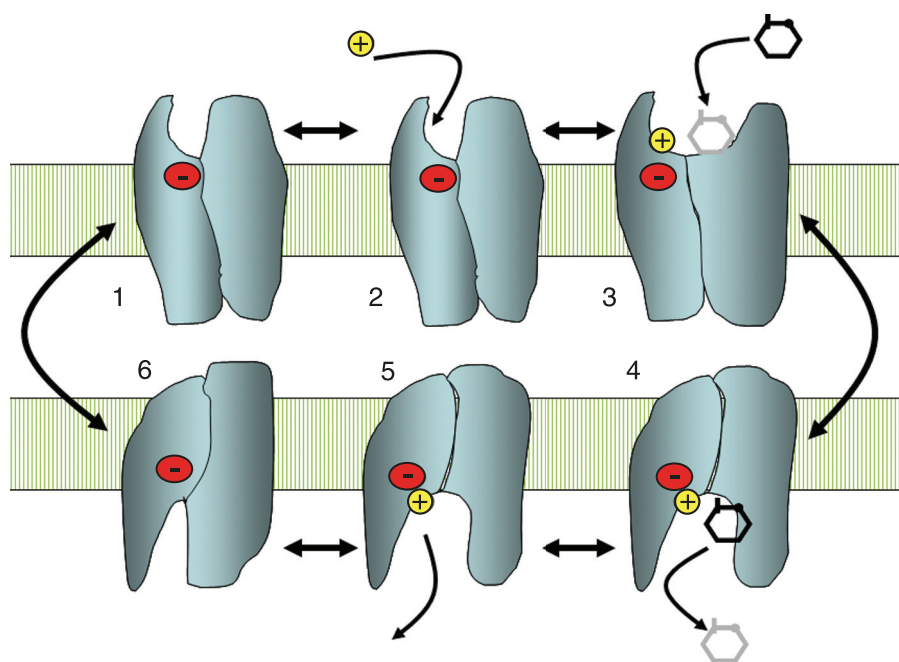
Our review begins in 1987 with the cloning of the intestinal Na⁺/glucose cotransporter (SGLT1) (61), and here we focus on the biology of human SGLTs in health and disease. As more transporters were cloned, it was found that SGLT1 was the first member of a large group of proteins in the SGLT (SSS) gene family (<http://pfam.sanger.ac.uk>). There are 12 members of the human family (SLC5), and they include Na⁺ cotransporters for sugars, myo-inositol, iodide, short-chain fatty acids, and choline (251). A major shock came with solving the crystal structure of vSGLT (48) when we discovered that members of unrelated gene transporter families share the same basic core structure, suggesting a common mechanism (1). It has also gradually emerged that SGLTs are expressed throughout the body, indicating their importance in organs other than the intestine and kidney, e.g., SGLT1 is active in specific regions of the brain such as the hippocampus. This review will cover these advances, but it should be emphasized that this is a rather egocentric view of the SGLTs.

II. 1987 BC

In the quarter of a century following its publication and before cloning (BC), the Na⁺/glucose transport hypothesis was extensively tested in the intestine and kidney using in vitro techniques and radioactive tracers (³H- and ¹⁴C-labeled sugars as well as ²²Na and ²⁴Na) and/or electrical assays. It was established that the natural sugars D-glucose and D-galactose, and their nonmetabolized homologs, 3-O-methyl-D-glucoside and α -methyl-D-glucopyranoside, were all transported across the brush-border membrane in a Na⁺-dependent, phlorizin-sensitive manner, but 2-deoxy-D-glucose and fructose were not. Transport was associated with a depolarization of the membrane potential, and the rate of transport was voltage dependent. Na⁺ was required in the extracellular solutions to drive uphill transport, but Na⁺ could be mimicked by H⁺ and Li⁺ and not K⁺, Rb⁺, Cs⁺, or choline⁺. In terms of sugar selectivity, it was established that hexoses with equatorial -OH groups at carbons 2 and 3 were transported, but 2-deoxy-D-glucose, 3-deoxy-D-glucose, D-mannose, and D-xylose were not. Several glucosides and β -glucopyranosides were also found to be transported, e.g., 3-O-methyl-D-glucoside, and β -phenyl-D-glucopyranoside but others, notably phlorizin (215), were potent competitive inhibitors. At least in the case of the chick intestine, it was demonstrated that there was a tight stoichiometry between ²²Na and ¹⁴C sugar transport with a coupling coefficient of 2.

A great deal of effort was directed at unraveling the kinetics of cotransport, but this resulted in conflicting models largely due to limitations of the methods. Experimental limitations included the following: 1) flux measurements are prone to error at low specific activities of the tracers; 2) difficulty of measuring initial rates of transport under well-defined *cis*- and *trans*-conditions; 3) uncontrolled membrane potential; 4) presence of other transport systems (diffusion, uniport); and 5) possibility of multiple transporters in natural membranes. Even under the best of circumstances, e.g., voltage-clamped membrane vesicles or isolated cells, it was difficult to counter all these limitations.

Probably the most succinct discussion of the kinetics of intestinal Na^+ /glucose cotransport was provided by Stan Schultz in 1985 (195). His model, Figure 2, was a rapid equilibrium, ordered, six-state scheme where one external Na^+ binds first to produce a conformational change permitting sugar binding and then Na^+ /glucose cotransport. The empty carrier was modeled as a negatively charged protein ($z = -1$) that was sensitive to membrane potential. Although this simple equilibrium model requires eight independent parameters that are difficult to estimate, the general predictions were consistent with the experimental data, e.g., maximum transport is independent of external Na^+ concentration, and the apparent K_m for sugar is Na^+ dependent and voltage sensitive. While it was clear that the transporter is reversible, little was known about the kinetics of efflux due to the inherent experimental hurdles at the time. Further progress was hindered by the difficulty in teasing out the kinetics of the partial reactions.



The SGLT1 protein was not definitively identified until 20 years after the cotransport hypothesis was proposed. This was finally accomplished by the Semenza and Wright labs through the use of azido-phlorizin-photoaffinity labeling, antibodies, and group specific reagents (79, 169, 192). We demonstrated that the lysine reagents phenyl-isothiocyanate (PITC) and fluorescein isothiocyanate (FITC) labeled the protein in the absence of Na^+ and d-glucose. Specific labeling of the transporter was then achieved by pretreating the membranes with PITC in the presence of Na^+ and glucose, washing, and then labeling with FITC in the presence or absence of Na^+ and glucose. The fluorescently labeled protein was then identified as a 73-kDa band on SDS-PAGE. Na^+ specifically quenched the fluorescence of FITC bound to a lysine at or near the glucose binding site, and this was interpreted as a conformation change that permitted sugar binding (169).

During this period evidence emerged that there are at least two different Na^+ /glucose transporters. First, microperfusion studies in the kidney revealed that the early proximal tubule absorbed glucose with a K_m (2 mM) higher than in the late proximal tubule (0.5 mM) (5). Second, it was found that brush-border membrane vesicles prepared from the renal outer cortex and outer medulla have low- (K_m 6 mM) and high-affinity (K_m 0.3 mM) transporters (223, 224). The low-affinity SGLT transporter had an apparent coupling stoichiometry of 1 Na^+ :1 sugar, whereas for the high-affinity transporter, it was 2 Na^+ :1 sugar. The low-affinity transporter became to be known as SGLT2, and the high-affinity transporter was determined to be SGLT1 (245). Third, different inherited defects of glucose transport were found in the intestine and

FIG. 2. A mechanical model for Na^+ -coupled sugar transport. This is a 6-state rapid equilibrium, alternating access model, based on that proposed by Schultz (195). States 1–3 face outward, and states 4–6 face inward. The unloaded negatively charged carrier (state 1) has low affinity for external sugar before sodium binds. After external Na^+ and sugar binding, the tertiary Na^+ /sugar/carrier undergoes a conformational change to present the Na^+ and sugar binding sites to the cytoplasm where the ligands are released, either Na^+ or glucose first. The unloaded carrier (state 6) then undergoes a further conformation change to reexpose the binding sites to the external surface of the membrane. The voltage dependence of Na^+ /sugar cotransport could arise from the electrodiffusion of Na^+ in and out of the binding site at each side of the membrane, and/or the translocation (reorientation) of the charged form of the carrier from one surface to the other.

kidney, i.e., intestinal glucose galactose malabsorption (GGM) was not associated with a major defect in renal glucose reabsorption (193), while congenital defects in renal reabsorption (familial renal glucosuria, FRG) were not accompanied by defects in intestinal absorption (244, 250).

III. EXPRESSION CLONING

The mid-1980s brought astonishing progress in the cloning of membrane proteins as exemplified by the successes with the facilitated glucose transporter GLUT1 (150) and the red cell Cl/HCO₃ exchanger (97). These clones were isolated from cDNA libraries by screening with antibodies and/or synthetic oligonucleotide probes based on partial amino acid sequences. We were determined to clone SGLT1 and initiated a program to purify and sequence FITC-labeled SGLT from rabbit brush borders (Brian Pearce), recruit a postdoctoral fellow with experience in DNA sequencing (Matthias Hediger), and an undergraduate student (Tyson Ikeda) to develop a heterologous expression system to study the functional properties of clones. Michael Coady, a new graduate student, also joined the team. Cameron Gunderson, who had just returned to UCLA from a postdoctoral position at University College in London, advised us to use *Xenopus laevis* oocytes as an expression system. Soon thereafter we established that native oocytes did not exhibit an endogenous sodium glucose cotransporter as determined by uptakes of α-methyl-D-glucopyranoside (αMDG) in the presence and absence of Na⁺. However, injection of intestinal poly(A)⁺ RNA into the oocytes increased the rate of Na⁺-dependent αMDG uptake by an order of magnitude compared with H₂O-injected control oocytes. This established that oocytes were a good system to study the function of cloned SGLTs.

Unfortunately, our attempt to purify and sequence SGLT1 peptides failed, so by necessity we used transport assays in oocytes to screen intestinal cDNA libraries. To simplify the task, Matthias Hediger used preparative gel electrophoresis to fractionate mRNA, and he isolated an enriched fraction (2.0–2.6 kb) containing the mRNA coding for SGLT1 (62). cDNA was synthesized from this fraction, and a plasmid library was constructed in the Bluescript expression vector. Synthetic RNA was prepared from cDNA from pools of clones, and this was used to screen for transport activity in the oocyte expression assay. One pool of clones gave a positive signal, and this group was further subdivided until a single clone was isolated: pMJC424, selected by Mike Coady on 4/24/1987, increased Na⁺-dependent αMDG uptake by more than 1,000-fold (61). Soon thereafter, human SGLT1 was cloned (64).

A. The Intestinal Brush-Border Transporter

Is SGLT1 the intestinal brush-border transporter? This question was resolved by comparing and contrasting the properties of the cloned transporter expressed in oocytes with the Na⁺/glucose cotransporter in the intestinal brush-border membranes (82). The ion specificity, sugar specificity, and sodium activation plots were similar: neither choline, nor K⁺, nor Li⁺ could efficiently replace Na⁺ in driving sugar transport; sugar transport had a Na⁺ Hill coefficient of close to 2; and other hexoses inhibited αMDG transport while mannitol and L-glucose did not. Furthermore, the properties of the cloned rabbit and human transporters were similar when expressed in mammalian cell lines (COS7), insect cells (Sf9 cells), or bacteria (10, 176, 202, 228). The apparent αMDG affinity ($K_{0.5}$) was 0.1–0.5 mM in oocytes, CO7 cells, and *Escherichia coli*. The kinetics for αMDG transport across intestinal brush-border membranes is more complex: apparently with high- and low-affinity systems in brush-border membrane vesicles ($K_{0.5}$ values of 0.04 and 0.6 mM, Ref. 82); and an unexplained discrepancy between these apparent affinities and those measured *in vivo*, 10–30 mM for glucose, galactose, and αMDG in rats (31). This discrepancy also holds for the apparent inhibitor constant for phlorizin, 0.2 μM for rat SGLT1 in oocytes to 100 μM *in vivo* (6, 163).

The cloned SGLT1 expressed in oocytes is electrogenic (11, 226). Figure 3A shows that 10 mM αMDG depolarized the membrane potential by 70 mV (from -35 to +35 mV), and under voltage clamp (-50 mV), the sugar

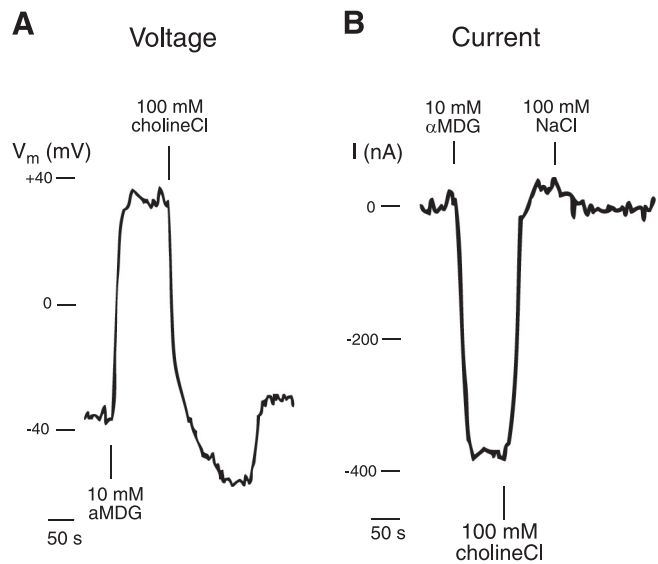


FIG. 3. Electrical properties of hSGLT1 expressed in oocytes. The oocyte was bathed in 100 mM NaCl buffer (in mM: 100 NaCl, 2 KCl, 1 MgCl₂, 10 HEPES/Tris, pH 7.5) at 20°C. A: depolarization of the membrane potential after addition of 10 mM αMDG. B: inward current produced by 10 mM αMDG when the same oocyte was voltage-clamped at -50 mV. (From D. D. F. Loo and E. M. Wright, unpublished data.)

induced an inward current of 400 nA (Fig. 3B). Neither membrane depolarization nor inward currents are observed in the absence of Na^+ in SGLT1 expressing oocytes or in control oocytes. The electrophysiological properties of SGLT1 can be then used to explore sugar and ion specificity.

Figure 4A shows an experiment with hSGLT1 (37). The addition of 1 mM α MDG rapidly produced an inward current of 800 nA, and this was reversed by washing out the sugar in a Na^+ -free buffer (choline Cl). Restoring the external Na^+ buffer brought the current back to the starting level. No inward sugar-induced currents were observed in the absence of Na^+ (choline Cl), i.e., the sugar-induced currents are inward Na^+ currents. The addition of the β -glucoside indican (2 mM) also produced a reversible inward current, but the β -glucoside esculin (10 mM) did not. Phlorizin alone (100 μM) did not induce an inward current but rather inhibits a small inward current, and this suggests that SGLT1 transports a modest amount of Na^+ in the absence of sugar (226). There was no effect of phlorizin in control oocytes or in hSGLT1 oocytes in the absence of Na^+ . The final part of this experiment shows the second trial with α MDG produced an inward current similar to the first and that esculin partially inhibits the α MDG current. This simple experiment suggests that indican is a substrate for hSGLT1, while esculin is not but instead behaves as an inhibitor (37).

An advantage of the electrical assays for SGLT1 sugar transport kinetics is that radioactive substrates are not required. This is illustrated for two sugars in Figure 4B, where we measured the kinetics of both α MDG and 3-fluoro-3-deoxy-D-glucose at an external NaCl concentration of 100 mM and a membrane potential of -50 mV (38). Both sugars have close to the same maximum velocity (maximum sugar currents of 860 and 775 nA) but different apparent affinities ($K_{0.5}$ values of 0.5 and 9 mM). The α MDG $K_{0.5}$ is similar to that obtained with radioactive tracer uptakes. A further advantage of the electrophysiological assays is that it is possible to obtain a complete data set on a single oocyte for the kinetics of sugar transport as a function of the membrane potential and the external sodium, sugar, and inhibitor concentrations (presented below). Clearly, the magnitude of the maximum currents depends on the level of SGLT expression that varies from cell to cell.

Taken together with studies of glucose-galactose malabsorption (see sect. XIVD), these data show that the clone isolated from the small intestine is in fact the brush-border SGLT1.

B. Stoichiometry of Na^+ to Glucose Transport

The ability of SGLTs to accumulate sugar is critically dependent on the stoichiometry of the Na^+ and sugar

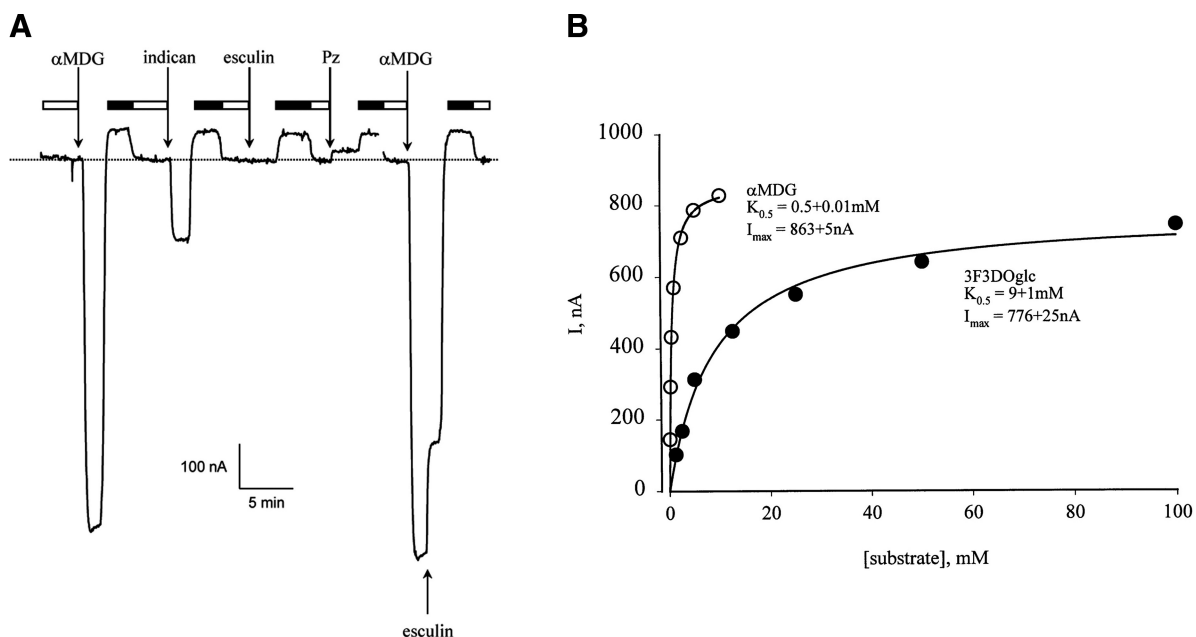


FIG. 4. *A:* Na^+ current was measured in a single hSGLT1 injected oocyte in the presence of different glycosides (37). The membrane potential was clamped at -50 mV. The horizontal line indicated the baseline current in Na^+ medium in the absence of substrate. The addition of 1 mM α MDG and 2 mM indican induced inward currents, 100 mM Pz reduced the baseline current, and 10 mM Esulin did not produce a current but inhibited the α MDG current by 30%. After the addition of each sugar, the oocyte was washed out in Na^+ -free medium (black box) followed by Na^+ medium (blank box). *B:* kinetics of α MDG and 3F3DOGlc in a single oocyte expressing hSGLT1 by measuring sugar-induced currents as a function of sugar concentration (38). Kinetic constants (means \pm SE), $K_{0.5}$, and I_{\max} were obtained by fitting the sugar-dependent currents for each sugar concentration to the equation, $I = I_{\max} \times [S] / (K_{0.5} + [S])$. The apparent affinities for each sugar in each SGLT are summarized in Table 2.

fluxes, i.e., $[S]_i/[S]_o = ([Na^+]_o/[Na^+]_i)^n \exp(VF/RT)^n$, where $[S]$ and $[Na^+]$ are the intracellular (i) and extracellular (o) sugar and Na^+ concentrations, respectively; V is the membrane potential, F is the Faraday constant, R is the gas constant, T is the absolute temperature, and n is the coupling coefficient. This relationship gives the theoretical equilibrium intracellular sugar concentration for a given Na^+ electrochemical potential gradient, and it assumes that there is no sugar metabolism and no other route of sugar transport into or out of the cell. Thus, for the same Na^+ electrochemical potential gradient, e.g., $V = -36$ mV and $[Na^+]_o/[Na^+]_i = 5$, increasing the stoichiometry from 1 to 2 increases the theoretical sugar concentration ratio by 20-fold (see Ref. 92). An experimental problem in establishing the stoichiometry using thermodynamics has been the uncertainty in determining the membrane potential, the internal Na^+ and sugar concentrations, and sugar metabolism. This has been overcome by measuring reversal potentials with defined ion and nonmetabolized sugar concentrations on each side of the membrane (17, 81).

We determined stoichiometry by simultaneously measuring currents and radioactive tracer fluxes into single oocytes expressing rabbit SGLT1 (139). The experimental protocol is illustrated in Figure 5A, where the baseline current of an oocyte is recorded in the absence of sugar and radioactive tracers. The current was then recorded continuously while superfusing the oocyte with $200 \mu M \alpha$ MDG and $10 mM^{22}NaCl$ for 10 min. The integrated sugar-induced currents (charge expressed in moles) are plotted against the ^{22}Na uptakes in Figure 5B and give a slope of 1.0 ± 0.1 , i.e., the sugar-induced

current through SGLT1 is exclusively a Na^+ current. Similar experiments were carried out to measure $50-500 \mu M [^{14}C]\alpha$ MDG uptakes, and Figure 5C shows that plotting charge versus sugar uptakes has a slope of 1.6 ± 0.3 . With a higher Na^+ concentration ($100 mM NaCl$ at -110 mV), the Na^+ to α MDG coupling ratio is 1.9 ± 0.1 . These results are in close agreement with reversal potential measurements on hSGLT1 (17, 81) and the radioactive tracer experiments on chick intestinal cells (93). The stoichiometry for pig SGLT3 is also 2/1 (34).

C. Reversible Transport

Two major approaches have been used to study reverse transport: the first was to express rabbit SGLT1 in oocytes and employ isolated patch-clamp techniques to measure the kinetics of Na^+ /glucose outward currents (47, 191), and the second was to express hSGLT in bacteria, prepare right-side-out and inside-out membrane vesicles, and measure the transport kinetics of sugar uptake using radioactive tracer techniques (176).

The patch-clamp approach is illustrated in Figure 6A. Currents were recorded from an isolated patch of oocyte plasma membrane expressing SGLT1. The pipette solution contained a buffer with $10 mM NaCl$ and no sugar (the extracellular solution) while the bath (intracellular solution) contained $0-500 mM NaCl$ and $0-500 mM$ sugar. The sugar-dependent currents across the membrane were recorded at voltages between -150 and $+50$ mV (intracellular side with respect to the extracellular side). In this particular experiment, the current was recorded with an

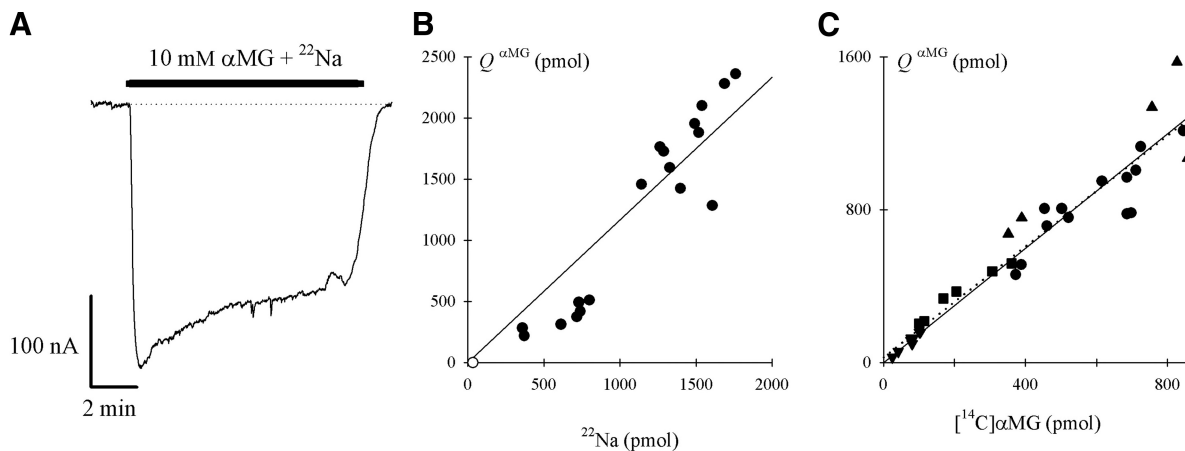


FIG. 5. Stoichiometry of Na^+ /glucose cotransport. A: sugar-dependent current (with membrane potential clamped at -70 mV) was continuously monitored in an oocyte expressing rabbit SGLT1 (139). Baseline current was stable in $10 mM Na^+$ before superfusing $10 mM \alpha$ MDG together with $10 mM^{22}Na$ for 10 min (shown by the solid bar) before washing out with $10 mM Na^+$ (without tracer). The sugar-dependent inward charge ($Q_{\alpha\text{MDG}}$), i.e., integral of the sugar-induced current over 10 min, was -1.4×10^{-4} Coulombs, equivalent to $1,425$ pmol of monovalent charge. ^{22}Na accumulation in this oocyte was $1,398$ pmol (having subtracted the mean basal ^{22}Na accumulation over 10 min in control oocytes), yielding a charge-to- ^{22}Na ratio of 1:1. B: charge/ ^{22}Na stoichiometry for rSGLT1. Sugar-dependent charge ($Q_{\alpha\text{MDG}}$) and ^{22}Na accumulation over 10 min at $10 mM Na^+$ were simultaneously determined at -70 mV in 19 oocytes expressing rSGLT1. The charge/ ^{22}Na stoichiometry was 1.0 ± 0.1 (SE). C: Na^+/α MDG stoichiometry for rSGLT1. $Q_{\alpha\text{MDG}}$ was compared with the accumulation of $50-500 \mu M [^{14}C]\alpha$ MDG over 1–10 min, at -70 mV. The mean Na^+/α MDG coupling coefficient was 1.6 ± 0.3 at -70 mV.

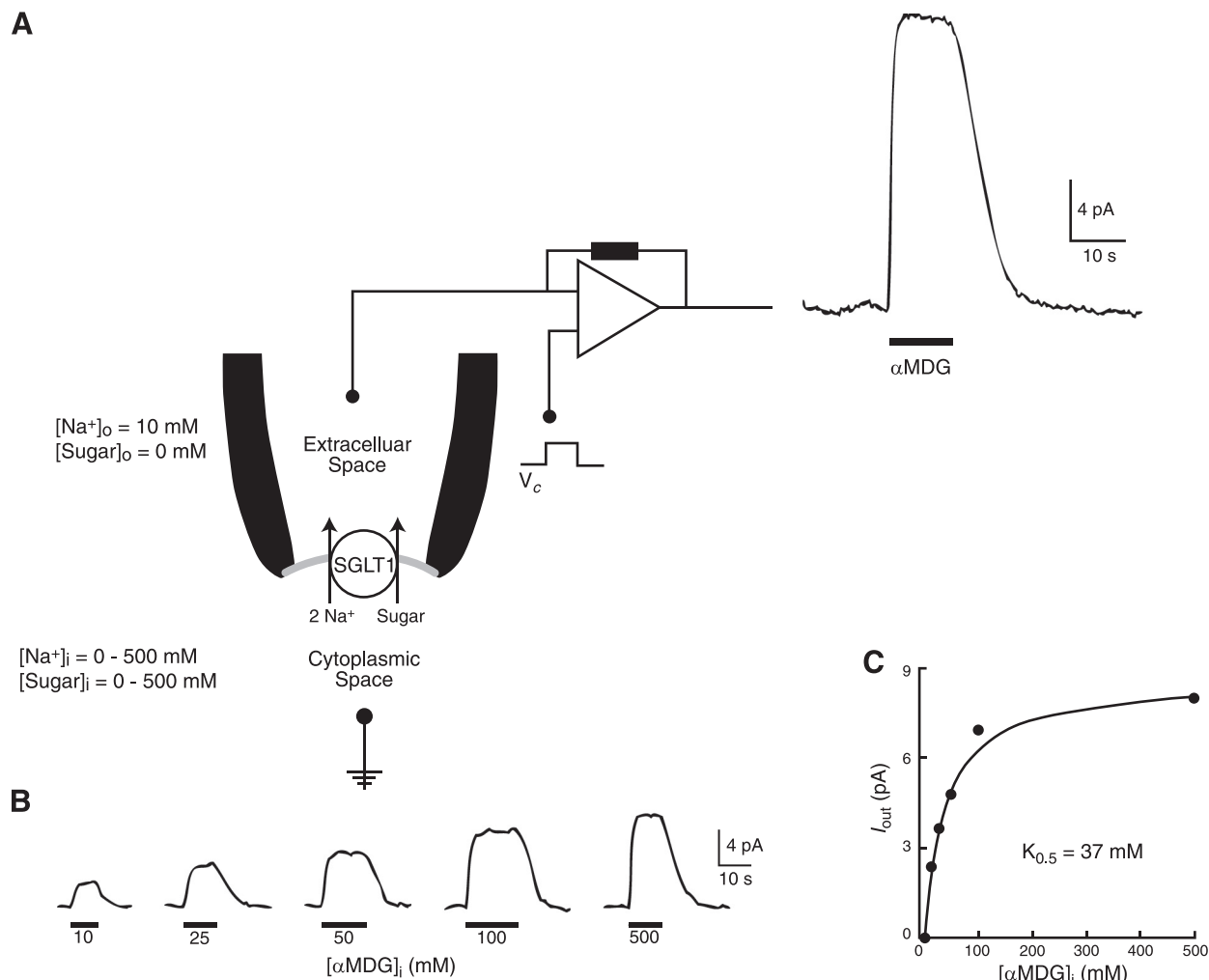


FIG. 6. Outward Na^+ /sugar cotransport by rabbit SGLT1 in an excised inside-out patch of oocyte membrane (47). *A*: membrane potential was clamped at 0 mV, at the time shown by the bar, and 100 mM α MDG was added to the external superfusing solution (internal surface of SGLT1). Sugar induced an upward deflection of the current trace, signifying an outward current (20 nA). Pipette (or external) solution contained the following (in mM): 10 NaCl, 90 choline Cl, 2 KCl, 1 $CaCl_2$, 1 $MgCl_2$, and 10 HEPES, pH 7.5. Bath (or internal) solution contained the following (in mM): 500 NaCl, 2 KCl, 1 $CaCl_2$, 1 $MgCl_2$, and 10 HEPES, pH 7.2. *B*: dependence of the outward current on internal $[\alpha\text{MDG}]_i$ (47). Current records in the same patch (expressing rabbit SGLT1) as various concentrations of α MDG were added to the bath solution. Pipette and bath solutions contained 10 and 500 mM Na^+ at 0 mV (V_m). *C*: relationship between the α MDG-induced outward current and $[\alpha\text{MDG}]_i$ from the experiment of Fig. 6*B*. The data followed a hyperbolic relation with a $K_{0.5}$ for α MDG of 37 ± 5 (SE) mM. Population average was 32 ± 8 mM ($n = 5$).

intracellular NaCl concentration of 500 mM at a holding potential of 0 mV. The addition of 100 mM α MDG to the intracellular solution produced an outward current (intracellular to extracellular current) of 20 pA that reversed on washing out the sugar. Figure 6*B* shows the outward currents produced by 10–500 mM α MDG, and Figure 6*C* is the plot of the sugar-induced current against the internal sugar concentration which yields a $K_{0.5}$ of 37 mM. As judged by the currents produced by different sugars at 100 mM, the relative sugar affinities for reverse transport is α MDG > D-galactose > 3-O-methyl-D-glucoside > D-glucose. This is quite different from the sugar selectivity for inward transport, α MDG ~ D-galactose ~ D-glucose >> 3-O-methyl-D-glucoside. Phlorizin is also a poor inhibitor from the cytosolic side of the membrane with a K_i esti-

mated to be >1 mM compared with <1 μ M at the extracellular surface.

The kinetics of forward and reverse sugar transport by human SGLT1 was also studied by monitoring radioactive α MDG uptake into right-side-out and inside-out membrane vesicles from bacteria expressing hSGLT1 (176). In both cases, incubation buffer contained 100 mM NaCl and the intravesicular buffer contained 100 mM K-phosphate. The α MDG $K_{0.5}$ for transport in the forward direction (extracellular to intracellular) was 0.15 mM (identical to that for SGLT expressed in oocytes, COS7, and Sf9 cells), while that for α MDG transport in the reverse direction (intracellular to extracellular) was 56 mM. α MDG transport in the forward direction was Na^+ dependent, phlorizin sensitive (K_i 2 μ M), and inhibited by

10 mM D-glucose, α MDG, and D-galactose, but not 2-deoxy-D-glucose, i.e., has the same sugar and phlorizin selectivity as uptakes into eukaryotes expressing hSGLT1. On the other hand, transport in the reverse direction was reduced by 100 mM sugar in the order α MDG > D-galactose, 3-O-methyl-D-glucoside > D-glucose, and there was a poor affinity for phlorizin, i.e., similar to that observed with reverse transport in the patch-clamp experiments (see above). These patch-clamp and vesicle studies show that transport through SGLT1 is indeed reversible, but the kinetics and sugar selectivity are asymmetrical. The implication is that there are slight differences in the substrate binding site depending on the direction of transport.

In summary, this preliminary characterization of the hSGLT1 clones, and those from rabbit (228), rat (164), mouse (33), and sheep SGLT1 (M. Bing, D. D. F. Loo, B. A. Hirayama, S. P. Shirazi-Beechey, and E. M. Wright, unpublished data), is quite consistent with all that was known about intestinal brush-border Na^+ /glucose transporter prior to cloning in 1987.

IV. GENES

A. Chromosomal Location

The chromosomal location of hSGLT1 was first assigned to the q11.2 qter region of chromosome 22 using Southern blots of genomic DNA from a panel of hamster-human somatic cell hybrids (60). This was further refined to the proximal half of band q13.1 by fluorescence in situ hybridization (FISH) with metaphase chromosomes from normal subjects and patients with translocations of chromosome 22, e.g., chronic myelogenous leukemia (CML) (219). hSGLT2 was assigned to chromosome 16 close to the centromere (240). The human genome project ultimately led to the gene mapping of all six SGLTs (Fig. 7) beginning with SGLT1 on chromosome 22 (39): SGLT2 16p12-p11; SGLT3 21q22.12; SGLT4 1p32; SGLT5 17p11.2, and SGLT6 16p12.1 (251).

B. Gene Mapping

The entire SGLT1 gene was initially mapped by cloning the gene from cosmid and λ phage clones, restriction mapping, and sequencing the exon/intron boundaries (220). This single-copy gene is large with 15 exons spanning 72 kb (Fig. 7). Transcription is under the control of a TATA box 27 bp upstream of the start codon, and the minimal promoter, as judged by luciferase reporter assays in Caco-2 cells (143), is encoded in nucleotides -235/+22. This minimal promoter contains three *cis*-elements, a HNF-1, and two GC boxes, which are critical for basal

expression and a novel 16-bp element that bind members of the Sp1 family of proteins that enhance basal expression. At least in sheep, HNF-1 (the HNF-1 α isoform) appears to be involved in the increase of intestinal SGLT1 gene expression in response to dietary glucose (229). Interestingly HNF-1 α -/- mice do not show any defect in intestinal glucose absorption, but instead show a renal defect in glucose reabsorption caused by a reduction in SGLT2 expression (172).

The organization of all 6 SGLT genes is quite similar, in having 15 exons, although they span from 8 to 72 kb (Fig. 7), but in other members of the SLC5 gene family the coding sequences are found in 14 (NIS), 8 (CHT), or only 1 exon(s) (SMIT1) (251). In SGLT 4–6 there are some indications of alternative splicing, and this may account for the difficulty in expressing these clones in heterologous expression systems.

C. Human Gene Family (SLC5)

The SGLT family grew larger with the identification of the renal Na^+ /glucose (SGLT2) (240), the renal Na^+ /myo-inositol (SMIT1) (104), the thyroid Na^+ /iodide (NIS) (29), and Na^+ /multivitamin (SMVT) (174). In humans, this is the SLC5 family (Fig. 8) (253).

All members of the SLC5 family code for 60- to 80-kDa proteins containing 580–718 amino acids. It is noteworthy that human SGLT3 is not a transporter but a glucosensor (35), and this underscores the importance of functional studies.

When human SGLT1 was first cloned, we found that it was homologous to the *E. coli* Na^+ /proline transporter PutP with a 28% amino acid identity (64). This family of genes, now known as the sodium solute symporter family (SSS or SSF), contains hundreds of proteins of pro- and eukaryotic origins with a common architecture. The SSF human genes belong to one of 14 members of the Pfam family clan APC (Cl0062) ([PF00474](http://pfam.sanger.ac.uk) <http://pfam.sanger.ac.uk>). The SSF structural domain proteins share the consensus sequence [GS]-2(2)-[LIY]-x(3)-[LIVMFYWSTAG](7)-x(3)-[LIY]-[STAV]-x(2)-G-G-[LMF]-x-[SAP]. There is also a common motif for the six SGLTs and SMIT1s [RxTxxxx-FLAGxxxxWWxxGAS] located on the intracellular loop between transmembrane helices (TM) 1 and 2 (Fig. 1 in Ref. 249). Other families in the APC clan include amino acid and bicarbonate cotransporters and exchangers. Readers should be aware that there is another classification system for membrane transporters where the SGLTs are included in the electrochemical potential-driven transporters as subclass 2.A.21 (<http://www.tcdb.org/tcdb>). These two websites, along with those at the United States National Library of Medicine (<http://www.ncbi.nlm.nih.gov>) and GeneCards (<http://www.genecards.org>), provide a rich source of information about the SGLTs.

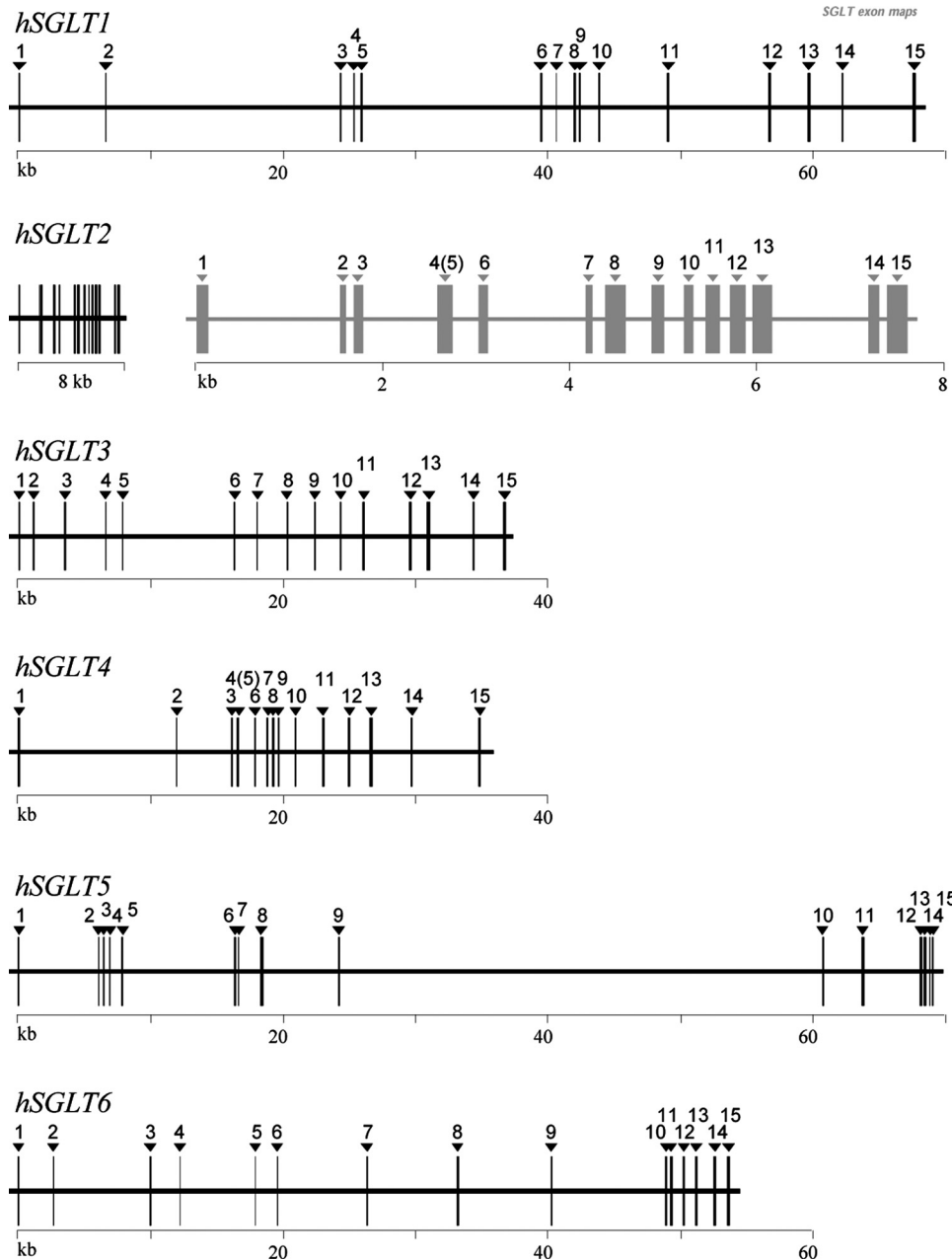


FIG. 7. The organization of human SGLT1–6 genes. All SGLT coding sequences are found in 15 exons. (From E. Turk and E. M. Wright, unpublished data.)

While we are fairly confident that all members of the human SGLT (SLC5) gene family have been identified, we recognize that other Na^+ -dependent sugar transporters may still be hiding in the human genome. One such novel transporter, NaGLT1, has been cloned from a rat kidney cDNA library (78). A human homolog has been identified, KIAA1919, and located on chromosome 6, 6q22. NaGLT1 is a 484-residue protein with <22% amino acid identity with SGLT and GLUT transporters. The gene is mainly expressed in the proximal tubule at a higher level than SGLT1 and SGLT2. When expressed in *Xenopus laevis* oocytes, the protein increased Na^+ -dependent α MDG uptake fourfold, and

this was blocked by phlorizin. Neither D-galactose nor D-mannose was transported by this low-affinity transporter. In HEK293 cells, NaGLT1 also behaved as a Na^+ -dependent, phlorizin-sensitive, D-fructose transporter (77).

D. Functional Characterization

Table 1 summarizes the functional properties and tissue distribution of the six human SGLTs. As discussed above, SGLT1 transports the natural sugars glucose and galactose with similar kinetics ($K_{0.5}$ and V_{\max}), and this

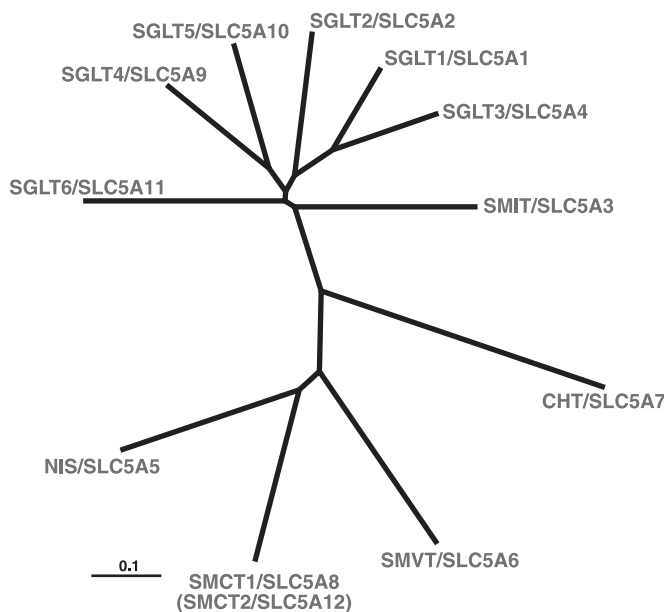


FIG. 8. An unrooted phylogenetic tree of the 12 human members of the SLC5 gene family. SGLT6 is also known as SMIT2 (Na^+ /inositol cotransporter 2). SMIT, sodium myo-inositol; CHT, choline; SMVT, sodium multivitamin; SMCT, sodium monocarboxylic acid; NIS, sodium iodide cotransporters. [Revised from Wright and Turk (253).]

protein is found abundantly in the brush-border membrane of the small intestine. Relatively little is known about the functional properties of the kidney SGLT2 as it is very poorly expressed in heterologous expression systems, but it is a glucose transporter that has poor affinity for galactose (81, 86, 214). SGLT2 has become a major drug target for regulating blood glucose levels in diabetes (see sect. XIVJ). SGLT3 is not a transporter in some species, e.g., in humans SGLT3 is a glucosensor expressed in the enteric nervous system and muscle (35). The sensor does not recognize galactose, but it has a very high affinity for imino sugars (235). There is one report on SGLT4 (214) showing that it is a low-affinity glucose transporter

with unusual sugar selectivity, i.e., it transports D-mannose but not galactose or 3-O-methyl-D-glucoside. The function of SGLT5 has only been reported in abstract form (113). When expressed in HEK293 cells it exhibits Na^+ -dependent, phlorizin-sensitive transport of α MDG and galactose. This gene is exclusively expressed in the renal cortex. SGLT6 (SMIT2) has the lowest amino acid identity with SGLT1 (50%), and its preferred substrate is not glucose but D-chiro-inositol (118). D-Glucose inhibits with a K_i of 6 mM. Rabbit SGLT6 transports glucose with a $K_{0.5}$ of 35 mM (21).

V. EXPRESSION

A. mRNA

Analysis of gene expression in human tissues has been carried out using Northern blots, real-time PCR, and RNAase protection assays on commercial mRNA samples, from a very limited pool of Caucasian individuals with unknown medical histories. A comprehensive study of SLC gene expression, including SGLT1, -2, -3, -5, and -6, using these samples has been published (151). Others have determined expression as the genes were cloned, e.g., SGLT4 with reference to SGLT1 and -2 (214). In the PCR experiments, SGLT1 was most abundant in the small intestine, and significant levels were also found in trachea, kidney, heart, and colon; SGLT2 was exclusively in kidney; SGLT3 in small intestine; SGLT4 in small intestine and kidney; SGLT5 in kidney; and SGLT6 in spinal cord, kidney, and brain. We found similar results in our RNase protection assays. (Figure 9 shows the profile of SGLT2 mRNA expression.) However, we find SGLT2 mRNA in cerebellum and low levels in tissues such as heart, salivary gland, liver, and thyroid; SGLT1 mRNA in testis; SGLT3 in testis, spleen, uterus, brain, kidney, and lung; SGLT4 in liver, brain, and lung; SGLT5 exclusively in

TABLE 1. SGLT substrates and expression in the human body

Gene	Substrate	$K_{0.5}$, mM	Distribution
SGLT1 (SLC5A1) Cotransporter	Glucose, galactose	0.5 0.5	Intestine, trachea, kidney, heart, brain, testis, prostate
SGLT2 (SLC5A2) Cotransporter	Glucose	6 NI	Kidney, brain, liver, thyroid, muscle, heart
SGLT3 (SLC5A4) Glucosensor	Glucose	20 NI	Intestine, testis, uterus, lung, brain, thyroid
SGLT4 (SLC5A9) Cotransporter	Glucose, mannose	2 0.15	Intestine, kidney, liver, brain, lung, trachea, uterus, pancreas
SGLT5 (SLC5A10) Cotransporter	Glucose Galactose	ND ND	Kidney cortex

Substrate specificity, affinity ($K_{0.5}$ for α MDG), and RNA expression of human SGLT (SLC5) genes are shown. Substrate specificity and α MDG transport were measured using heterologous expression systems (34, 81, 116, 211). RNA distribution is based on mRNA protection assays (M. Bing, M. G. Martin, and E. M. Wright, unpublished data) and Northern blots (SMIT2). ND, not determined; NI, noninteracting. [Revised from Wright et al. (246).]

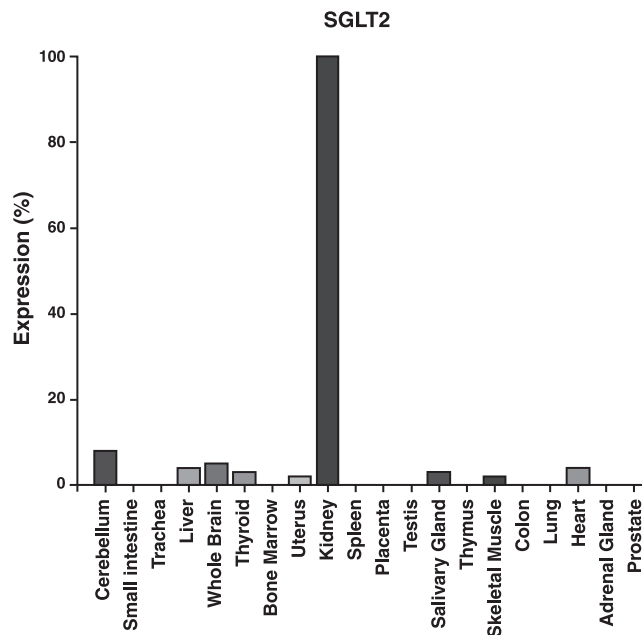


FIG. 9. Expression of SGLT2 mRNA in human tissue samples. These studies were carried out by RNase protection assays on commercial samples of human mRNA. The autoradiograms were digitized, and the protected fragments of SGLT2 mRNA were digitized, counted, and expressed as a percentage of that in the tissue expressing the highest abundance. mRNA extracted from the duodenum and renal cortex was included as controls. (From M. Bing, E. Turk, M. G. Martin, and E. M. Wright, unpublished data.)

kidney cortex; and SGLT6 in brain, kidney, and small intestine.

What remains to be determined is the cellular distribution of SGLT mRNAs in the organs and tissues of the human body, e.g., by *in situ* hybridization methods. This has been carried out for kidney, brain, and spinal cord in animal models (86, 173, 257; Allen Institute Brain Atlas <http://www.brain-map.org/>; Ref. 28). Significant levels of SGLT1 and SGLT2 mRNA are detected in specific regions of the pig, rabbit, rat, and mouse brain, e.g., pyramidal cells of the hippocampus, and in rat kidney SGLT2 mRNA is present in S1 segment tubules in the cortex while SGLT1 mRNA is in the outer stripe of the outer medulla.

Another source of information about SGLT gene expression in normal human tissues is the EST (expressed sequence tag) data bases, e.g., www.ncbi.nlm.nih.gov/unigene. For example, SGLT2 expression is similar to that for mRNA (Fig. 9), but positives are also reported for testis, placenta, larynx, pancreas, placenta, and stomach.

B. Proteins

Antibodies have been used to map SGLT expression in human cells and tissues, but so far there are no comprehensive studies, due to the lack of specific an-

tibodies and the availability of tissue. Soon after cloning of rabbit SGLT1, a series of polyclonal antibodies were raised to different SGLT1 peptide sequences and screened for their specificity on brush-border membranes using Western blots (70, 209). Our criteria for acceptable antibodies were that 1) antibodies made against two different peptides are able to recognize the same single band, and 2) the antigenic peptide had to block antibody binding. Two antibodies 8792 and 8821 met these criteria in blots of rabbit brush-border membranes. Figure 10 shows a Western blot of mouse intestinal brush-border membranes with a single, broad band of 75 kDa. No other immunoreactive bands were observed in these blots. We later demonstrated that the broad band was in part due to *N*-linked glycosylation of the brush-border SGLT1 (71). The same antibodies recognized cloned rabbit SGLT1 expressed in *Xenopus laevis* oocytes, but two bands are observed representing the core and unglycosylated protein (70).

It is important to recognize that membrane proteins run faster than expected from their molecular weight on SDS-PAGE gels with broad bands, presumably due to incomplete denaturing of membrane proteins by SDS. It appears that the apparent molecular weight of SGLTs can vary with the degree of glycosylation in that SGLT1s from different species range in size from 69 to 79 kDa (70). Finally, under different experimental conditions, multimeric SGLT1 bands may

Western Blot of Mouse Intestinal Brush Border Membranes

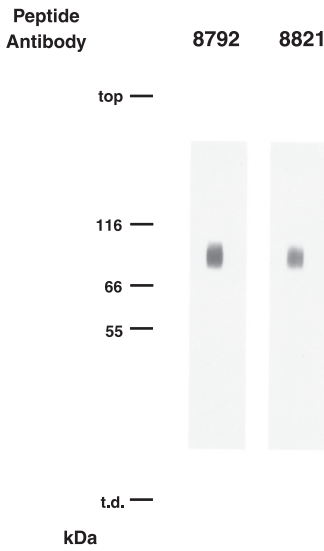


FIG. 10. Western blot of mouse intestinal brush-border membranes for SGLT1 using two antipeptide antibodies (no. 8792, residues 402–419; no. 8821, residues 604–615; Ref. 70). Both antibodies recognize the same 75-kDa protein, and the immunoreactivity was blocked with the peptides used to raise each antibody. Similar Western blots were obtained against hSGLT1 expressed in *Xenopus laevis* oocytes (140). [From Wright et al. (247).]

appear on the Western blots when frozen samples are used.

We have validated the use of our SGLT1 antibodies for immunolocalization studies, first in *Xenopus laevis* oocytes expressing wild-type rabbit SGLT1 and a mutant R427A rabbit SGLT1 that is not inserted into the plasma membrane (137). Confocal fluorescence microscopy showed 1) no SGLT immunoreactivity in control oocytes, 2) immunoreactivity was restricted to the plasma membrane in oocytes expressing wild-type SGLT1 (within the resolution of light microscopy), and 3) immunoreactivity only appeared just below the plasma membrane in oocytes expressing the R427 mutant. Freeze-fracture electron microscopy confirmed that SGLT1 was not in the plasma membrane of control or oocytes expressing the mutant in contrast to the 5,000 copies/ μm^2 in wild-type expressing oocytes. Similar results were observed with hSGLT1 (140). Second, we have demonstrated that the intensity of the 78-kDa immunoreactive band in Western blots of sheep brush-border membranes is proportional to the transport activity over two orders of magnitude (201).

Such antibodies have been used to immunolocalize SGLT1 protein in the rat intestine and kidney (209), rat and pig brain (173), and rat heart and skeletal muscle (45). The studies from the Koepsell group can be used to illustrate the problems that arise when the peptide antibody recognizes additional bands on Western blots. Their antibody to residues 582–600 of rat SGLT1 also recognized a 40-kDa protein (probably a viral receptor protein) that led to erroneous conclusions, e.g., that SGLT1 was expressed in endothelial cells in brain (4). Commercial antibodies are available for SGLT1 and other SGLTs, but these have not been carefully evaluated, so published results with these have to be reevaluated. One report has appeared using a SGLT2 antibody to localize SGLT2 in wild-type and *SGLT2*^{-/-} mice (227). This study clearly identifies SGLT2 in the brush-border membrane of early proximal tubules.

As yet, the potential to map the distribution of SGLTs throughout the human body by immunolocalization has not been realized.

C. PET Imaging

Positron emission tomography (PET) has revolutionized studies of glucose uptake and metabolism in organs and tissues in the human body in health and disease using 2-[¹⁸F]-2-deoxy-D-glucose (2FDG) as a tracer (see Ref. 170). 2FDG PET is a safe, noninvasive, imaging method to monitor glucose uptake and trapping in cells and tissues with high spatial and temporal resolution (2 mm, s). Fluorine-18 is the preferred positron emitter as it decays with a conveniently short

half-life (109.8 min). 2FDG is transported into cells via GLUTs, where it is trapped after conversion to the phosphorylated sugar 2-FDG-6-phosphate. Accumulation of 2-FDG-6-phosphate in tissues is followed as a function of time, and a compartmental analysis is used to extract rate constants for transport and glucose phosphorylation (80). 2FDG is a poor substrate for SGLTs (Table 2), so PET studies with this tracer do not report cellular glucose uptake via SGLTs.

We and others (12, 30) have developed SGLT specific PET probes to study the distribution of functional SGLTs in the human body. Our first generation tracer is α -methyl-4-deoxy-4-[¹⁸F]fluoro-D-glucopyranoside (Me4FDG). This was designed based on functional studies of sugar selectivity: 1) α MDG is a substrate for SGLTs and not GLUTs (92, 252); 2) α MDG is not phosphorylated by hexokinase (7, 258); 3) 4FDG is a high-affinity substrate for SGLT1 (Table 2) (38); and 4) Me4FDG is a high-affinity substrate for SGLT1 and -2, but not GLUTs (Table 2) (81; B. A. Hirayama and E. M. Wright, unpublished data).

PET scans of one adult male subject with 2FDG and Me4FDG are shown in Figure 11. 2FDG was accumulated in regions of the brain, excreted by the kidneys into the urinary bladder, and accumulated to a lesser degree in heart, liver, kidneys, and muscle. These observations agree with the expression of GLUT1 in the blood-brain barrier, GLUT3 in brain, GLUT2 in liver and kidney, and GLUT4 in muscle. The excretion of 2FDG into the urine is also expected as 2FDG is not a substrate for SGLTs, and hence, it is not salvaged from the glomerular filtrate.

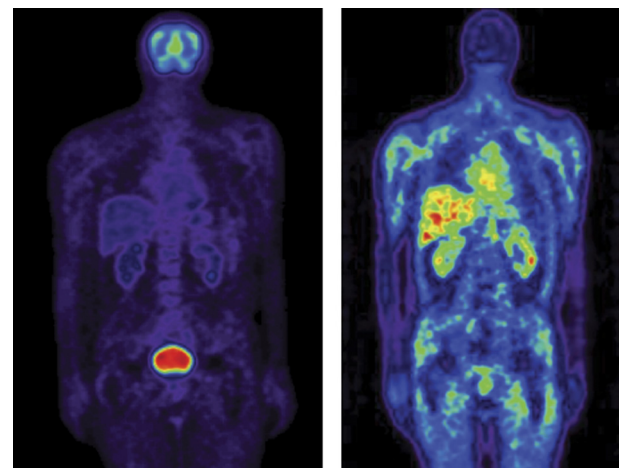


FIG. 11. The biodistributions of FDG (left) and Me-4-[¹⁸F]FDG (right) on a 64-yr-old male subject (EMW). 10 mCi of each tracer were injected intravenously into the subject on separate occasions, and whole body PET scans were collected at 60 min after intravenous injections. (Note that each scan is normalized to the highest point, i.e., the two scan scales are not normalized to each other.) The scans show the lack of brain uptake of Me-4-[¹⁸F]FDG, compared with 2-FDG, and there is no elimination of Me-4-[¹⁸F]FDG into the urinary bladder. (From E. M. Wright, A. Halabi, B. A. Hirayama, V. Kepe, and J. R. Barrio, unpublished data.)

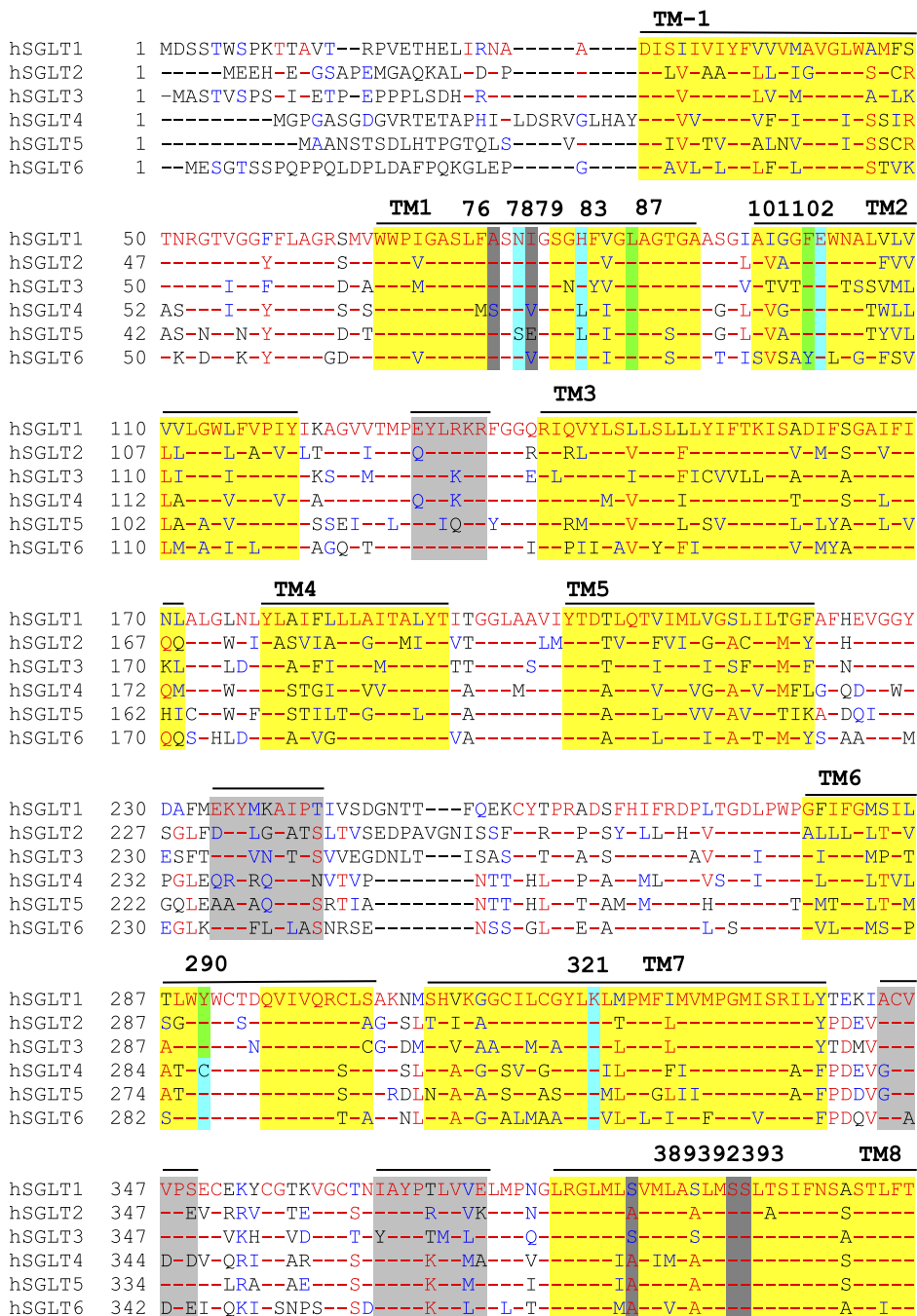


FIG. 12. The amino acids sequences of SGLT1-6 were aligned using Maximum Linkage Clustering. Gaps are indicated by dashed lines, and conserved residues are highlighted in red (single letter code or dashed lines). The location of the 14 putative transmembrane helices (TM-1 to TM13) based on the crystal structure of vSGLT is highlighted in yellow (1, 48). Highlighted boxes identify homologous vSGLT residues forming the sugar (green) and sodium (dark gray) binding sites and the external and internal gates (green). Note the general conservation of the ligand coordinating and gate residues in the six SGLT proteins.

In contrast, Me4FDG did not enter the brain, confirming that it is not a substrate for GLUT1 in the blood-brain barrier, and did not appear in the urinary bladder, indicating that it was indeed salvaged from the glomerular filtrate by SGLTs in the proximal tubule. Me4FDG was accumulated in kidney, skeletal muscle, heart, liver, prostate, uterus, and testes, suggesting that SGLT genes are functional in these tissues (Table 1). Studies are in progress to determine which SGLTs are functional in these organs and tissues, and how expression is regulated. So far, *in vivo* and *in vitro* assays of

SGLT activity in rat show SGLT activity in discrete regions of the brain, e.g., hippocampus and cerebral cortices (258).

VI. PROKARYOTE SGLTS

A few thousand SSF (SSS) genes have been identified in archaea, prokaryote, and eukaryote genomes. The interested reader is referred to the phylogenetic tree of 41 diverse members of the gene family (253).

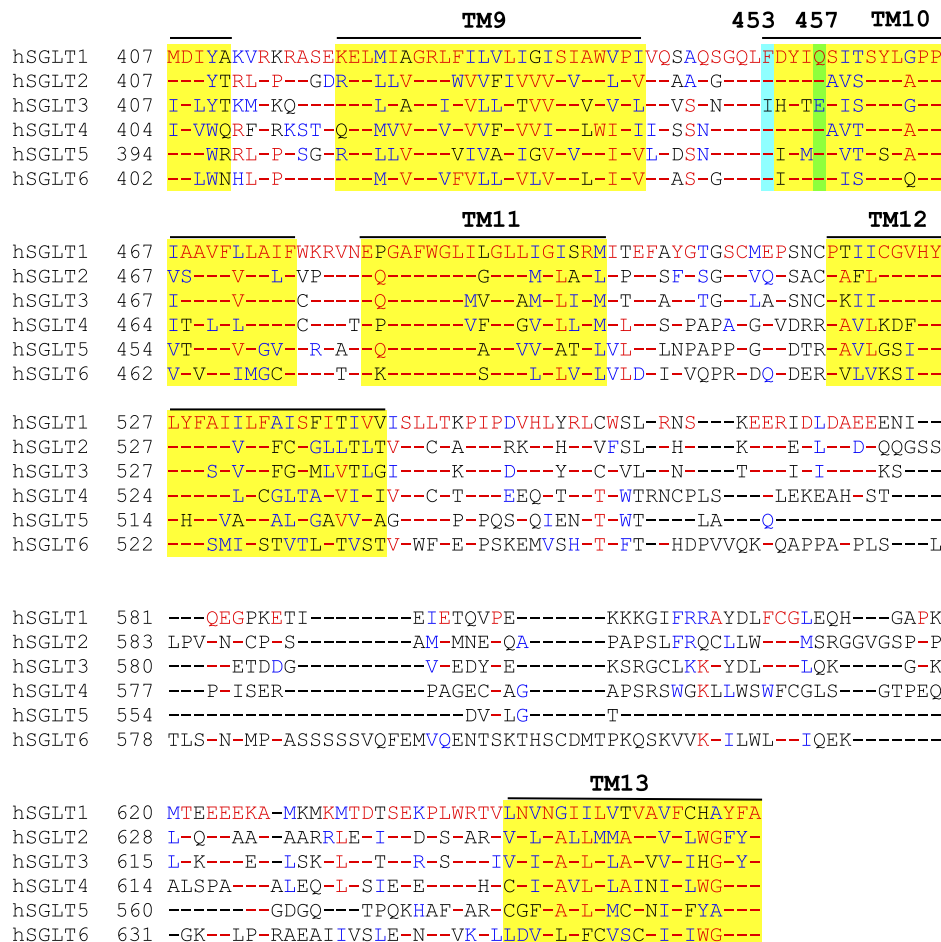


FIG. 12.—Continued

Ever since SGLT1 was cloned, we have made efforts to overexpress and purify SGLT1 protein for biochemical and structural studies with limited success (e.g., Refs. 177, 202). Following the success of others in the overexpression, purification, and reconstitution of bacterial symporters, we focused our attention on the structure and function of the bacterial homolog of SGLT coded by the *Sgls* gene of *Vibrio parahaemolyticus*, vSGLT (218). The protein is smaller than hSGLT1, 543 versus 664 residues, but there is 32% identity and 75% similarity between the amino acid sequences. This protein has only one cysteine residue, and this facilitates cysteine-scanning accessibility measurements. Our strategy was first to express the gene in *E. coli* and to characterize vSGLT transport activity in intact cells, membrane vesicles; purified protein reconstituted into proteoliposomes, and solubilized protein (216, 218, 230, 254).

We found that vSGLT carried out Na⁺-dependent transport of D-galactose, but not αMDG. Phlorizin inhibited transport but with a poor affinity ($K_i > 1$ mM). In proteoliposomes, the $K_{0.5}$ for D-galactose transport was 158 μM, and the Hill coefficient for Na⁺ was 1, suggesting a 1:1 coupling between Na⁺ and galactose transport. The

Na⁺ $K_{0.5}$ depended on galactose concentration; in *Xenopus laevis* oocytes, it was 17 mM at 0.06 mM galactose (116). Kinetic studies with proteoliposomes and purified protein in detergent further revealed that the system was ordered with Na⁺ binding before sugar and that Na⁺ binding results in a conformation change that underlies sugar binding (216, 230).

In summary, the functional properties show that vSGLT has much in common with hSGLT1, but there are differences in sugar selectivity and Na⁺-to-sugar transport stoichiometry (1:1 rather than the 2:1 for SGLT1). This encouraged us to purify this protein for structural studies (see below).

VII. STRUCTURE

A. Amino Acid Sequences

The SGLT genes code for proteins with 596–681 residues. Alternative splicing with SGLT4–6 may result in the predicted amino acid content varying by up to 52 residues (253). Relative to human SGLT1, there is between 50 and 70% identity and 67–84% similarity in the

sequences for SGLT2–6. The greatest divergence in sequence occurs at the extracellular NH₂-terminal domain and the COOH-terminal third of the proteins. This also holds for members of the larger SSS family (253). Figure 12 shows an alignment of the SGLT1–6 amino acid sequences.

B. Secondary Structure

The amino acid sequence of hSGLT1 superimposed on a 14-transmembrane helix model is shown in Figure 13. Note that the 14 helices have been renumbered from TM –1 to 13 based on the crystal structure of LeuT structural family (1). This model was based primarily on *N*-glycosylation scanning mutagenesis analysis and computer algorithms, e.g., the neural network algorithm to predict membrane spans (217, 221). Additional experimental approaches used by us and others included antibody recognition of polypeptide epitopes and labeling of cysteine mutants with “impermeant” alkylating reagents such as rhodamine maleimide and charged methanethiosulfonates (MTSET, MTSES). While our model is now generally accepted, there is disagreement about the location of the 90-residue hydrophilic domain between TMs 12 and 13. A succinct review of experimental evidence for the topol-

ogy of the COOH-terminal domain is contained in a paper by Gagnon et al. (53). In essence, the controversy stems from studies on the accessibility of the large, very hydrophilic loop to hydrophilic reagents and antibodies in the extracellular compartment, raising the possibility of a reentrant loop between TMs 12 and 13. This was apparently supported by a proteomic study of trypsin digests of hSGLT1 in proteoliposomes (102), but we think that the results are ambiguous as hSGLT1 was most likely reconstituted into the liposomes in both orientations.

Results in support of the 14 TM model (Fig. 13) include experiments on vSGLT. The secondary structure model for vSGLT closely resembles that for hSGLT1 but with shorter hydrophilic loops between the transmembrane domains (221). The NH₂-terminal of vSGLT was shown to be extracellular by electrospray ionization mass spectrometry (ESI-MS) of purified vSGLT: the NH₂ terminal retains its formylmethionine that would normally be excised in the cytoplasm (218). The crystal structure of vSGLT (48) showed that the protein has 14 transmembrane helices and that the hydrophilic loop between TM12 and 13 remains in the cytoplasm. TM13 lies outside the core of the structure in both the native protein and that with an additional COOH-terminal TM helix (glycophorin A). In Figure 13, we have superimposed the helices in the

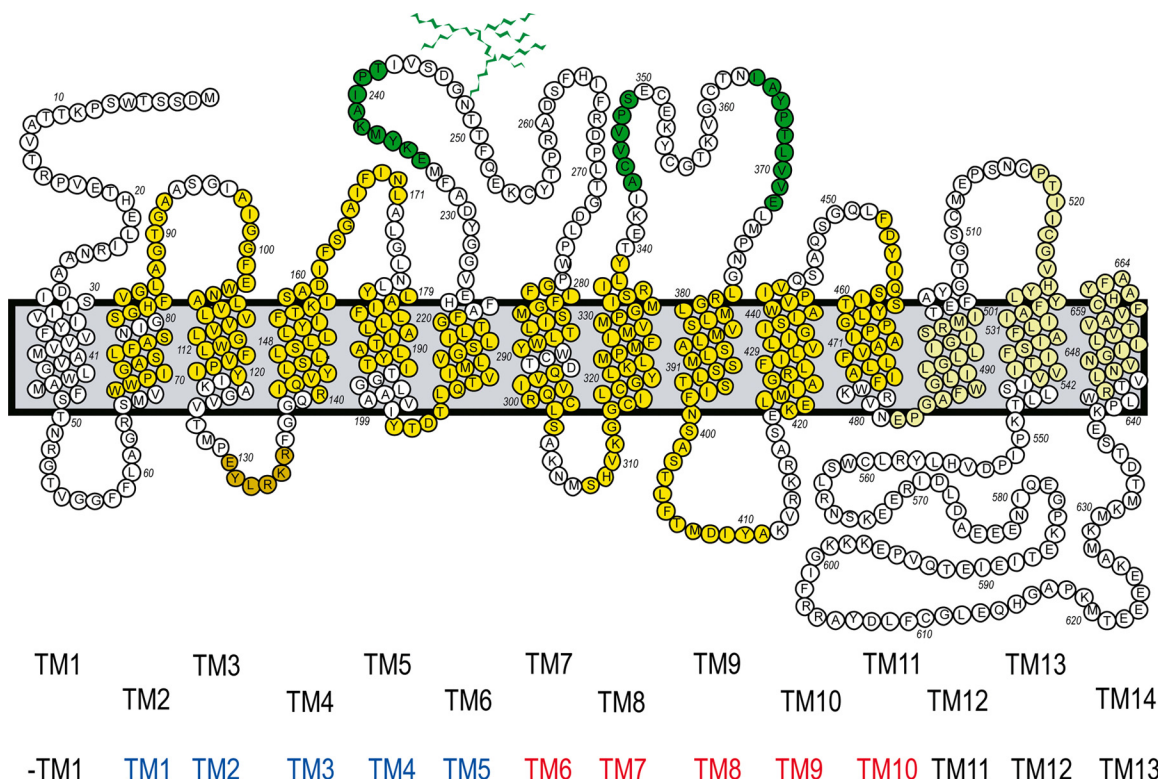


FIG. 13. Secondary structure model of hSGLT1 (217). This model shows the sequence of the 664 residues arranged in 14 transmembrane helices with both the NH₂ and COOH termini facing the extracellular side of the plasma membrane. A single *N*-glycosylation site occurs at Asn (N) 248. Highlighted are the locations of the helical domains based on the vSGLT structure (48). The numbering of the TMs has been revised to conform with the LeuT structural fold to allow easy comparisons between structural family members, i.e., TM1 through TM13 (1).

vSGLT crystal structure on the hSGLT1 secondary structure model to highlight the agreement between the model and the crystal structure. Differences between the predicted secondary structure and the crystal structure arise mainly due to assumptions in modeling of the length and angle of helical segments crossing the membrane. For example, the results of cysteine scanning studies on rabbit SGLT1 suggesting a helical loop in the extracellular loop between TM3 and TM4 have been reinterpreted as part of TM3 in light of the vSGLT crystal structure (122). It remains to be determined why the hSGLT loop between TM12 and 13 is accessible to extracellular hydrophilic reagents.

Apart from *N*-linked glycosylation at N248, there is little direct evidence for other secondary modifications of SGLT1. *N*-linked glycosylation is not required for functional expression (63, 71). There is no evidence for *O*-linked glycosylation (71). Analysis of potential secondary modification of the SGLTs using PROSITE at PredictProtein (www.predictprotein.org) predicts motifs for cAMP, PKC, CK2, and Tyr phosphorylation and myristoylation sites. The importance of these has yet to be tested by direct experiment (the regulation of SGLT1 expression by kinases will be discussed below).

C. Monomer

Freeze-fracture studies of hSGLT1 expressed in oocyte plasma membranes and purified vSGLT reconstituted in proteoliposomes clearly demonstrated that both are fully functional as monomeric proteins (46, 218). This conclusion was based on the cross-sectional area of the proteins within the plasma membrane relative to those of membrane proteins of known structure that were also analyzed by freeze-fracture electron microscopy in oocyte membranes. The dimensions of the vSGLT electron microscopic images, corrected for the thickness of carbon/platinum coating, also agreed with the dimensions of the vSGLT crystal structure. One unresolved question is the discrepancy between these electron microscopic images of hSGLT1 and the radiation inactivation analysis of transport in rabbit brush-border membranes, suggesting that SGLT1 is a homotetramer (205).

Hermann Koepsell and colleagues (106) cloned a 67-kDa protein RS1 that was initially claimed to be a regulatory subunit, but subsequent studies demonstrated that RS1 was not in the plasma membrane but instead participated in the transcription and posttranslational trafficking of SGLT1 and other transporters (101, 182, 232, 233).

D. Protein

The major advantages of using vSGLT for structure/function studies are as follows: 1) vSGLT only contains

one cysteine residue, and this is not required for full functional activity (254). Thus cysteine scanning accessibility measurements can be made on a cysteine-less background (230). 2) vSGLT mutants expressed in bacteria do not suffer from trafficking defects observed in eukaryotes, and 3) it is straightforward to isolate vSGLT mutants from bacterial expression systems for biochemical studies. In 1999, Eric Turk took on the challenge to produce vSGLT protein for structural studies.

Our strategy to produce and purify the transporter (vSGLT) was to construct an expression plasmid (VNH6A) by inserting the full *Sgls* coding region into the pBAD18 vector and appending a COOH-terminal HIS tag for metal-chelate chromatography (218). To facilitate optimization of vSGLT protein expression and purification, we also constructed a vSGLT-green fluorescence protein (GFP) fusion plasmid where a 15th TM (glycophorin) was used to locate GFP in the cytoplasm (VNGFPH6). Both constructs were expressed in XL1Blue cells after induction with L-arabinose. Membrane vesicles were prepared by standard methods, and the protein solubilization and purification was followed by monitoring GFP fluorescence. Both the vSGLT and vSGLT-GFP proteins were almost exclusively expressed in the bacterial plasma membrane, and each was fully active in cell and membrane vesicle transport assays (218, 254). The proteins were purified to homogeneity by metal-chelate and size exclusion chromatography as judged by SDS-PAGE and mass spectrometry. ESI-MS confirmed the correct mass of the proteins to within 0.01% (218). Currently, we obtain >5 mg of vSGLT protein from 10 liters of cultured cells. Biochemical, transport, and fluorescence assays show that purified vSGLT protein is fully active when incorporated into liposomes (48, 216, 218, 230, 231). Using similar strategies, we and others have had success in purifying hSGLT1 from *E. coli* and *Pichia pastoris* (177, 225).

E. Circular Dichroism

Given that vSGLT was fully functional when solubilized in detergent, we examined the secondary structure of the protein using ultraviolet (UV) circular dichroism (CD) (216). The fusion protein vSGLT-GFP was included as a control as the crystal structure of GFP is known (50% β -strand and <2% α -helix). A large crystallographic reference set of proteins was available, and three algorithms (CONTINLL, CDSSTR, and SELCON3) were used to predict the helical content of membrane proteins. For example, CD measurements accurately predicted the helical content of lactose permease (85%, compared with 86% in the crystal). Our CD spectra predicted 82–89% α -helical content in vSGLT and 60% in the vSGLT-GFP fusion protein. This decrease with vSGLT-GFP was anticipated given the low helical content of GFP. We further estimate

that 27–33% of the total helical content in vSGLT occurs outside the plasma membrane domain (216). Again, the CD predicted secondary structure is quite consistent with the subsequent vSGLT crystal structure.

D-Galactose changed the near UV CD, 250–300 nm, of vSGLT in the presence of Na^+ , but not in K^+ (216). This, and the galactose-induced change in tryptophan fluorescence (231), probably reflects conformational changes at a tryptophan residue at or near the galactose binding site. A tryptophan was found flanking the Y263 involved in stacking with galactose in the sugar binding site (48).

Attenuated total reflection Fourier transform infrared (ATR-FTIR) spectroscopy was also used to examine the structure of vSGLT (112), but the results suggested that only 35% α -helical content in the absence of ligands. This secondary structure profile was unexpected, but it is now known that FTIR methods have a tendency to predict β -sheet content in α -helical membrane proteins where none exists, e.g., aquaporin 1 and lactose permease. The FTIR studies do show that there is limited extent of hydrogen-deuterium (H/D) exchange in vSGLT, 40–50% in 2 h compared with 80% for lactose permease and GLUT1. These results are interpreted as showing that there is limited water access to vSGLT compared with that found

for the $\text{H}^+/\text{lactose}$ symporter. Na^+ and D-galactose each reduced H/D exchange in vSGLT, and this suggested that the ligands caused a compaction of the overall protein structure.

F. Crystal Structure

The first structure of vSGLT was solved in collaboration with Jeff Abramson and his team (48). The structural model was refined to 2.7 Å, and all residues, apart from those in TM–1 and 36 disordered residues in two cytoplasmic loop regions, were assigned. Figure 14A contains a topology model of the crystal structure, and Figure 14B shows a side view of the model in the membrane plane.

As predicted, the structure contains 14 TMs with the NH_2 and COOH termini on the same side of the membrane. A single galactose molecule was found in the center of the protein, where it was occluded from both the extra- and intracellular compartments. Notable features not anticipated from the amino acid sequence and the analyses of secondary structure were as follows: 1) the inverted topology repeat (TM1-TM5 and TM6–10) that forms the core of the structure (there is

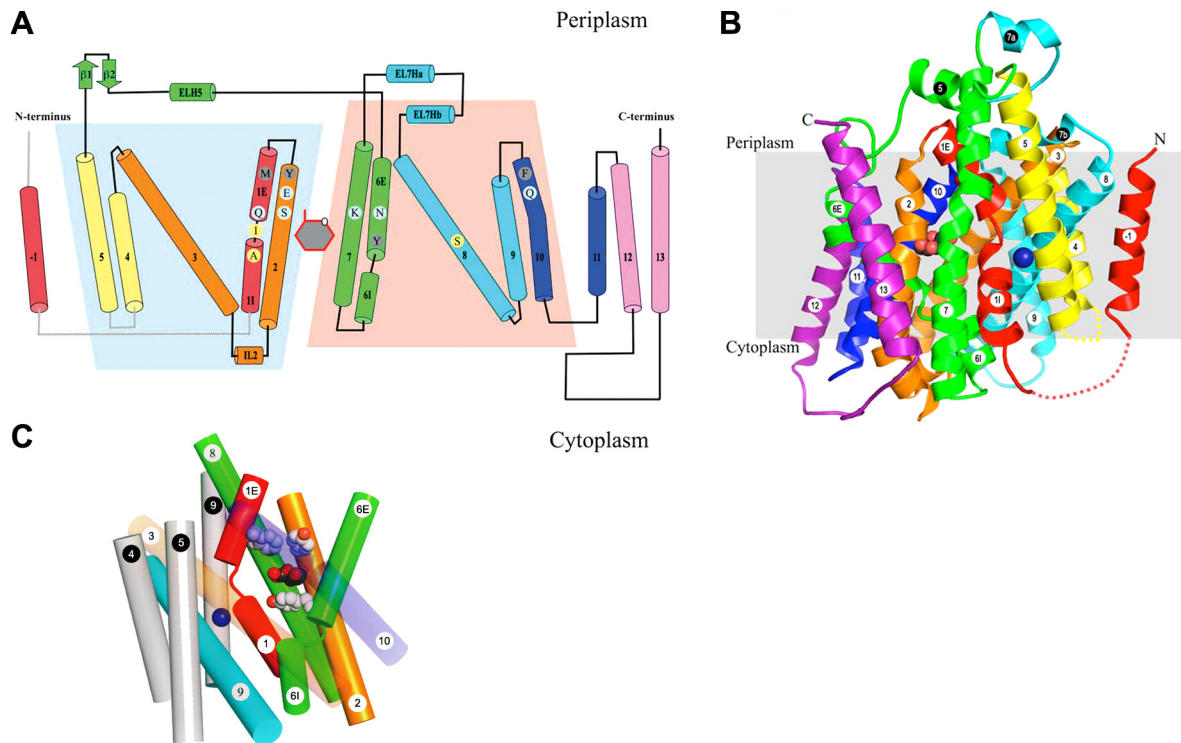


FIG. 14. The structure of vSGLT. **A:** topology model showing the 14 TM from the NH_2 terminal (TM-1) to the COOH terminal (TM13). The blue and red trapezoids represent the inverted topology of TM1-TM5 and TM6-TM10. **B:** a side view of the 3-dimensional structure viewed from the membrane plane. The location of the bound sugar is shown as black and red spheres. Residues involved in sugar binding and gating and Na^+ binding are shown on TM as circles. The two discontinuities represent the disordered regions of the protein. [**A** and **B** redrawn from Faham et al. (48).] **C:** ligand binding sites in vSGLT. An overview of the galactose and Na^+ binding sites. The sugar is occluded from the exterior by external and internal hydrophobic gates.

no amino acid sequence homology between the repeats, but the structures can be superimposed with a RMSD of 3.9 Å; 2) the two discontinuous membrane helices, TM1 and TM6, which lie at the interface between the two inverted repeats (these two discontinuous helices are at the core of the sugar binding site); 3) the large tilts in TM3 and TM8; 4) the variation in the length of the TM helices; and 5) the presence of helical structures in the extra- and intracellular loops. The total helical content of the transmembrane domains and the extracellular loops (72%) was anticipated by the CD analysis (216). The structure contains a central group of seven helices (TM1, TM2, TM3, TM6, TM7, TM8, and TM10) that are supported by a ring of other helices. Finally, the cytoplasmic halves of TM1, TM2, TM5, TM7, and TM9 form a large hydrophilic cavity that extends from the inner gate of the sugar binding site (Y263) to the cytoplasm.

An overview of the location of the galactose and Na^+ binding sites and the intra- and extracellular gates is provided in Figure 14C. A close-up view of the galactose binding site from the extracellular surface in Figure 15A shows the position of the gates, M73, Y87, F424, and Y263 that block sugar entry and exit. The outer gate residues are removed from the external view in Figure 15B to highlight the residues coordinating with galactose. Hydrogen bonds from the residues coordinating with D-galactose include Q428, Q69, E88, K294, S91, and N260, and the pyranose ring is stacked against the inner gate residue Y263. The putative Na^+ binding site, ~10 Å away from the sugar binding site, has coordinating residues S354, S355 (TM8), and the carbonyl oxygens of A62, I65 (TM1), and A361 (TM8) (see Fig. 16B below). The functional importance of the sugar and sodium coordinating residues has been confirmed by transport assays on the mutated proteins, Q69A, E88A, K294A, Q428A, and S365A, reconstituted into proteoliposomes (48).

Both the bound galactose and Na^+ binding sites face the cytoplasmic aqueous vestibule. Galactose is prevented from entering the vestibule by the inner gate tyrosine (Y263), and Na^+ is held in place by the coordinating residues on TM1 and TM8 (see below).

There are additional helical structures in the hydrophilic loops connecting the transmembrane helices. On the intracellular surface, a short helix (IL2) between TM2 and TM3 lies on the outer edge of the hydrophilic cavity leading to the sugar binding site, and on the extracellular surface one of two helices (EL7b) forms extensive contacts with TM1 and TM3. An additional extracellular helix (EL5) between TM5 and TM6 connects the two inverted repeats, and in hSGLT1, this loop contains the *N*-linked glycosylation site (see Fig. 13). The hydrophilic helices are predicted to play roles in the conformational changes that underlie coupling of Na^+ and sugar transport.

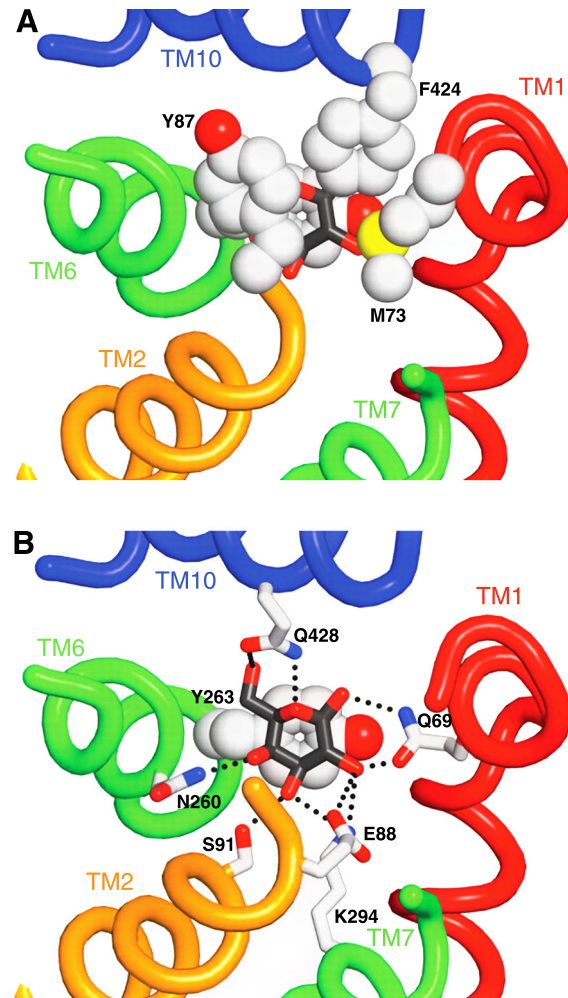


FIG. 15. A: view of the galactose binding site from the external surface showing the external gates. B: the galactose binding site. The external gates were removed for clarity. The tyrosine residue below the sugar, Y263, is shown in gray spheres. The coordinating residues and bonds to glucose are indicated by dotted lines. [Redrawn from Faham et al. (48).]

vSGLT is constructed of two precisely assembled halves, so it is amazing that these assemble properly to form a fully functional transporter when they are expressed in the same cell under two different promoters, the NH₂-terminal half (residues 1–279) and the COOH-terminal half (residues 280–543) (254).

G. LeuT Superfamily

The core structure of vSGLT (TM1-TM5 and TM6-TM10) is virtually identical to the core structure of LeuT, an unrelated transporter in the neurotransmitter sodium cotransporter gene family (NSS) (48, 256). This was soon followed by reports that two other unrelated sodium cotransporters, Mhp1 and BetP, share the same core structure (183, 241). The core structure of all four pro-

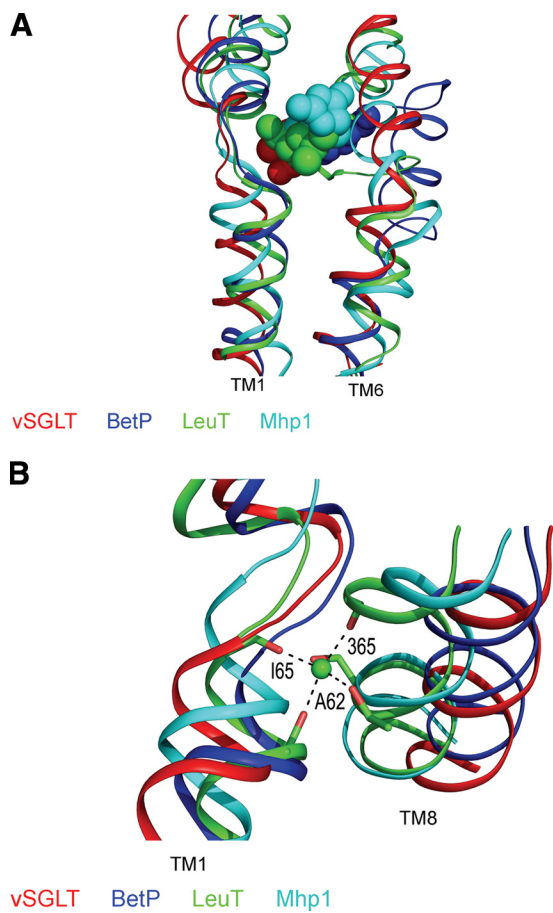


FIG. 16. The LeuT structural family. *A*: a structural alignment of TM1 and TM6 and the substrate binding sites for vSGLT (red, galactose), BetP (glycine betaine, blue), LeuT (leucine, green), and Mhp1 (benzylhydantoin, cyan). *B*: alignment of the Na² sites on TM1 and TM8. [Redrawn from Abramson and Wright (1).]

teins can be superimposed (RMSDs 3.8–4.5 Å), and as with vSGLT, the inverted repeats in each protein can be superimposed even though there is no amino acid sequence similarity. Figure 16*A* shows that the substrate binding sites have a common location approximately halfway across the membrane. While the substrate binding sites in the four proteins share a common location, the substrate specificities are determined by different coordinating residues.

The four proteins were found to be in slightly different conformations: LeuT and Mhp1 in an outward occluded conformation with aqueous vestibule extending from the substrate binding site to the extracellular surface; vSGLT in an inward occluded conformation with a hydrophilic vestibule leading from the sugar binding site to the cytoplasm; and BetP in an intermediate conformation with no aqueous vestibules leading to or from the betaine binding site (see sect. XII for further discussion). In each structure, additional TM helices may be present at the NH₂ or COOH termini, and these may or may not be important for function.

Two putative Na⁺ binding sites have been identified in LeuT, Na1, and Na2 (256). By homology, these two sites were also found in BetP, and one, Na2, was identified in vSGLT and Mhp1. Na1 overlaps with the substrate binding sites in LeuT and BetP, where the cation is coordinated with the carboxyl group of the substrate. In contrast, Na2 is formed by two conserved serine residues and backbone carbonyl oxygens (Fig. 16*B*). The presence of one or two sodium binding sites is correlated with the stoichiometry of transport.

The vSGLT2 Na² site appeared more open than that in LeuT (Fig. 16*B*), suggesting a different functional state. This was supported by molecular dynamic simulations: Na⁺ was stably bound to the Na² site in LeuT, whereas in vSGLT Na⁺ rapidly escaped down the aqueous vestibule into the cytoplasm (117, 238). More recently it was reported that the LeuT structural motif extends to a cation-independent arginine/agmatine antiporter (AdiC) in the APC gene family (50, 54). Na1 and Na2 sites were not found in this structure, and this validates the functional significance of the Na1 and Na2 sites in the sodium cotransporters. As yet, there is no information about the location of the second Na⁺-binding site in mammalian hSGLT1.

Although it is impossible to deduce transport mechanism from a single structure, it is feasible to gain insight into the structural rearrangements by examining the structures of the other transporters (see sect. XII).

VIII. SUGAR SELECTIVITY

Since 1987 the kinetics and specificity of SGLT isoforms have been studied using electrophysiological techniques on cloned rabbit, rat, mouse, or human SGLT1, SGLT2, and SGLT3 (33, 34, 37, 38, 67, 81, 86, 125, 235). Electrophysiological methods offer unique advantages: 1) they enable accurate determination of apparent affinities ($K_{0.5}$) from submicromolar to >100 mM; 2) measurement of $K_{0.5}$ and maximum rates of transport (I_{max}) for many different substrates on the same cell (see Fig. 4); 3) allow discrimination between substrates and competitive inhibitors (Fig. 4); and 4) determine inhibitor kinetics in the absence of substrates from leak currents (Fig. 4) and pre-steady-state charge movements (Fig. 20) (66).

A. Monosaccharides

Table 2 summarizes estimates of apparent sugar affinities ($K_{0.5}$) for the cloned Na⁺/sugar cotransporters hSGLTs 1–4, pig SGLT3, and SMIT1–2 from dog and rat. All transport or bind D-glucose and αMDG and are inhibited by phlorizin, but the affinity of the Na⁺/myo-inositol (SMIT) cotransporters for glucose are 1–2 orders of magnitude lower than hSGLT1. The most essential requirement for substrate interaction and transport by SGLTs is

TABLE 2. Sugar selectivities of SGLT 1–6

Sugar	Apparent Affinity, mM						
	hSGLT1	hSGLT2	hSGLT3	pSGLT3	hSGLT4	cSMIT 1	rtSMIT 2
αMDG	0.5 ^{4,5} (4** ¹⁸)	4.8 ^{11,18} (6** ¹⁸)	21 ^{7,15}	4 ^{5,13}	2.6 ¹	50 ³	>>50 ²⁰
D-Glucose	0.5 ^{¶1,4,5} (2** ¹⁸)	5 ^{**18}	19 ^{4,7}	8 ^{5,13}	7.7 ^{¶1}	>50 ³	36 ²
D-Galactose	1 ^{¶1,4,5} (6** ¹⁸)	>100 ¹⁸	NI ^{4,7,5}	>200 ⁵	>100 ^{¶1}	>>50 ³	>>50 ²⁰
1DOG	10 ⁵		43 ⁷	26 ⁵	>30 ^{*1}		
2DOG	>100 ⁵		NI ^{7,13}	NI ^{5,13}	>30 ^{*1}	>>50 ³	
2F2DOG	>>100 ¹⁹						NI ²⁰
Glucosamine	>>100 ¹⁹						
3DOG	>100 ⁷		NI ⁷	NI ¹⁵			
3F3DOG	9 ⁵						
4DOG	0.4 ⁷		>50 ⁷				
4F4DOG	0.07 ⁵		17 ⁷				
4F4DOGAl	1.3 ⁷		NI ⁷				
5ThioGlc	4 ⁵			17 ^{*5}			
6DOG	3 ⁵		>50 ⁷	4 ⁵			
6F6DOG	~5 ¹⁹						
3-OMG	3.3-6 ^{4,5}		NI ¹³	NI ^{4,5,13}	NI ^{*1}	>>50 ³	NI ²⁰
3-O-benzyl-glc	30 ¹⁷						
D-Mannose	NI ¹	>100 ^{¶1}	NI ¹³	NI ¹³	0.15 ¹		
D-Fructose	NI ¹	>100 ^{¶1}	NI ¹⁵		~100 ¹		
Myo-inositol	~500 ³					0.050 ³	0.27 ²
D-Chiro-inositol							0.31 ²
L-Fucose	>>100 ³					~50 ³	NI ^{2,20}
L-Glucose	>>100 ³		NI ¹³	NI ¹³		>50 ³	>>50 ²⁰
L-Xylose	~50 ³					~50 ³	>>50 ²⁰
D-Xylose	~50 ³		NI ¹³	NI ¹³		>>50 ³	~50 ²⁰
D-Allose	>>100 ¹⁸		NI ¹³				
D-Fucose	~50 ³					>>50 ³	NI ²⁰
βMDG	0.5 ⁵			7 ⁵			
1-Deoxyojirimycin	NI ⁷		0.004 ⁷				
1-Deoxygalactonojirimycin	NI ⁷		11 ⁷				
N-ethyl-1-deoxyojirimycin	NI ⁷		0.003 ⁷				
Miglyitol	NI ⁷		0.003 ⁷				
Miglustat	NI ⁷		0.0005 ⁷				
1-Deoxyojirimycin-1-sulfonic acid	NI ⁷		0.009 ⁷				

* K_p , or estimate of inhibition. **Measured at 37°C. ¶Value estimated from graph in paper. NI, no interaction. §EC₅₀. ‡ K_d . #rbSGLT1. References are as follows: hSGLT4: ¹Ref. 214; hSGLT1: ⁴Ref. 37, ⁵Ref. 38, ⁶Ref. 66, ¹⁷Ref. 67, ¹⁸Ref. 81, ¹⁹Hirayama and Wright, unpublished data; rat SMIT2: ²Ref. 3, ¹⁵Ref. 21; dog SMIT1: ³Ref. 58; hSGLT3: ⁷Ref. 235, ¹⁵Ref. 35, ¹³Ref. 138; hSGLT2: ⁸Ref. 147, ⁹Ref. 156, ¹⁰Ref. 255, ¹¹Ref. 159, ¹²Ref. 86; rbSGLT1: ¹⁴Ref. 136; pSGLT3: ¹⁶Ref. 234.

that the sugar must be a pyranose and cyclic polyhydroxy alcohols are noninteracting. Removal of the one, two, three, or six equatorial hydroxyls reduces the apparent affinity for hSGLT1 by a factor of 5 to >200 (1-deoxy-, 2-deoxy-, 3-deoxy-, and 6-deoxyglucose). The O1 in hSGLT3 is of minor importance as removal reduces the apparent affinity by only a factor of 2. The 4 hydroxyl is not essential for hSGLT1, but replacement with fluorine (4F4DOG) increases apparent affinity by a factor of 10. Adding F to 2-deoxyglucose (2F2DOG) does not restore the apparent affinity, whereas in the case of 3-deoxyglucose the affinity is partially restored ($K_{0.5}$ decreases from >100 to 9 mM). The SGLT isoforms 2 and 3 are more selective at the 4 position in that they have poor affinities for D-galactose relative to D-glucose. Oxygen 5, in the ring, is essential for recognition by hSGLT1, as replacement by sulfur is detrimental, and substitution by nitrogen abolishes binding completely. In contrast, imino sugars, e.g., 1-deoxyojirimycin, are the preferred ligand for SGLT3 with micromo-

lar affinities. At positions 2 and 3, the hydroxyl must be in the equatorial position as D-mannose and D-fucose do not interact with SGLT1, -2, or -3, but mannose is accepted by SGLT4.

Despite these differences in sugar affinity and selectivity, the sugar coordinating residues are generally conserved in the SGLT family (Table in Fig. 12). One significant exception is in SGLT3, where glutamic acid replaces glutamine at residue 457. Mutation of this residue, E457Q-SGLT3, resulted in a SGLT1-like phenotype (9), apart from a low galactose affinity ($K_{0.5} > 100$ mM). In contrast, mutation of 457 in SGLT1, Q457E, partially produced the SGLT3 phenotype; glucose was still transported, but the coupling between sugar and Na⁺ transport was not tight (38).

From studies of hSGLT1 using “mutated sugars”(38, 67, 235), we dissected the essential interactions of sugar recognition (Table 3). All of the D-glucose equatorial OH groups and pyranose oxygen are predicted to be involved

TABLE 3. Predicted interactions between glucose and SGLT1

Sugar	Interaction
O1	H-bond donor from protein
O2	H-bond acceptor and donor, with highly constrained side chain
O3	H-bond donor
O4	Fluorine substitution increased affinity 10-fold, H-bond not required
O5	Accepts H from protein only; nitrogen substitution absolutely unacceptable
O6	H-bond acceptor, but not essential; C5 methylene required
Plane	Stacking with an aromatic side chain

The $K_{0.5}$ values of a series of sugars in which the hydroxyls and pyranose oxygen were removed or substituted for other elements were determined. Comparison to the $K_{0.5}$ for glucose was then used to propose the pattern and importance of hydrogen bonding involved in recognition. Glucose has hydrophobic surfaces due to the axial orientation of its hydrogens in the plane of the ring.

in hydrogen bonding to the protein. Based on similarities to sugar binding proteins, such as the lectins, we also expected to see a hydrophobic stacking interaction with an aromatic residue (178, 211). We hypothesized that Q457 of hSGLT1 interacts with O1, O5, and O6; T460 interacts with O4; H-bonds to and from an unspecified residue with O2 and a hydrophobic stacking interaction with an aromatic side chain(38).

How do these predictions compare with those found in the vSGLT crystal structure (48)? The occluded sugar binding site in the crystal is dehydrated, and the sugar is coordinated by H-bonds with polar side chains and stacking of the hydrophobic face of the sugar with tyrosine 263 (Table 4 and Fig. 15B). The coordinating residues are constrained by adjacent side chains to provide a precise spatial arrangement for sugar identification.

hSGLT1 has 32% amino acid identity (60% similarity) with vSGLT, enabling us to model hSGLT1 based on the vSGLT crystal coordinates. How do the sugar interactions in the threaded hSGLT1 model compare with the predic-

tions based on experiment? Figure 17 shows the model of glucose binding to hSGLT1. In general, the interactions between glucose and the protein are accounted for, apart from a missing O1 interaction. Note that mutation of Q457C results in a 12-fold reduction in sugar affinity and that alkylation of this cysteine blocks sugar transport (38, 129). Experiments in progress have confirmed the importance of all the putative sugar coordinating residues (M. Sala-Rabanal, D. D. F. Loo, B. A. Hirayama, and E. M. Wright, unpublished data).

B. Glucosides

It has long been known that a variety of glucosides are transported by SGLTs. Studies from this and many other groups (e.g., Refs. 2, 37, 107, 136, 149) clearly show that SGLT1s accept β -aromatic and hydrophobic glucopyranosides, with affinity and transportability (V_{max}) determined by the groups decorating the aglycone. For example, phenyl- β -D-glucoside is transported by rabbit SGLT1, but phenyl- α -D-glucoside is noninteracting, i.e., neither a substrate nor an inhibitor (136). Adding a para-hydroxyl or amino group to phenyl- β -D-glucoside improves affinity, whereas a NO₂ creates an inhibitor. So the sugar binding site and translocation pathway is able to accept a large substituent to the pyranose ring, if it has the right characteristics. In addition to glucopyranosides, glucosides such as 3-O-methyl- and 3-O-benzyl glucoside are transported by hSGLT1 albeit with a lower affinity than glucose (Table 5). Large glucosides (up to 20 \times 12 \times 5 Å) are therefore transported through SGLT1, and this obviously requires large conformational changes in the protein.

These studies also suggest that there is a series of “selectivity filters” along the sugar translocation pathway through the protein and that the characteristics of these filters can be different from those in the binding site, and also vary among members of the SGLT family. For example, in rabbit SGLT1, adding a para-hydroxyl to phenyl- β -D-glucoside increased both affinity (3 times) and transport-

TABLE 4. Protein-sugar interactions in vSGLT

Sugar	Interaction
O1	Q69 supplies the essential H-bond
O2	Q69, E88, and K294 donate and accept; E88 and K294 interact with each other to stabilize their location
O3	E88, K294, and S91 donate and accept; position of S91 is constrained by interactions with multiple residues: W264, N260, and the backbone carbonyl from Y87; E88 and K294 stabilize each other
O4	S91 and N260 donate and accept; position of residues constrained by side-chain interactions
O5	Q428 donates the H-bond
O6	Q428 can donate and accept; the requirement for the 6C may be for distance to the residue from O6 or hydrophobic interaction with Y263
Plane	Stacking with Y263

The crystal structure of vSGLT contains a bound galactose and reveals the amino acids involved in sugar recognition. These sugar-protein bonds and interactions between side chains are summarized. We note that the crystal structure is an occluded state and may not represent the initial sugar binding site.

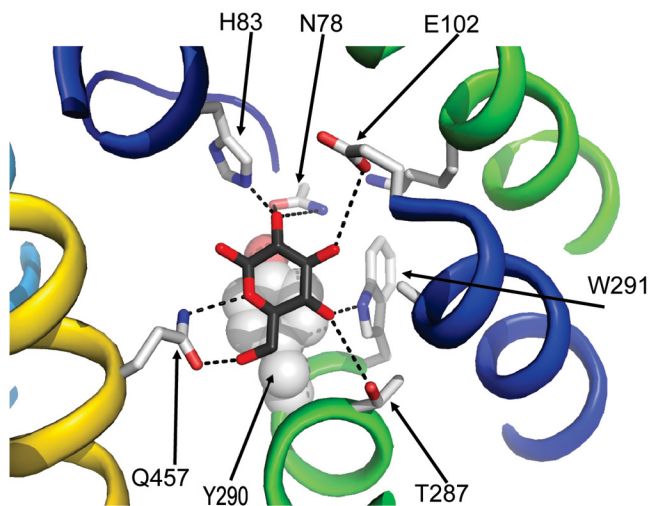


FIG. 17. Glucose binding to hSGLT (homology model). The primary sequence of hSGLT1 was aligned on that of vSGLT, and this was then superimposed on the vSGLT crystal structure to create a “threaded” model structure of hSGLT1 with glucose replacing galactose in the binding site: O1, no interaction observed; O2 N78, H83 can donate and accept; O3, E102 can donate and accept; O4, T287, W291 can donate and accept; O5, Q457 can donate; O6, Q457 donate and accept, possible hydrophobic with T290; and hydrophobic stacking with Y290. (From V. Chaptal, B. A. Hirayama, J. Abramson, and E. M. Wright, unpublished data.)

ability (1.5 times) (136), but in hSGLT1 there was no change in affinity but transportability increased threefold. Indican (3-indolyl- β -D-glucopyranoside) is a high-affinity ($60 \mu\text{M}$) transported substrate, but it is only transported at 14% of the maximal rate for α MDG ($I_{\max}^{\alpha\text{MDG}}$) in hSGLT1. It is also a substrate ($0.9 \mu\text{M}$) in pig SGLT3, but here it is transported at 80% of $I_{\max}^{\alpha\text{MDG}}$ (37). A simple modification can change transported indolyl glucosides from substrates into an inhibitor. When bromine is added at the 5-position of the substrate 3-indolyl- β -D-galactopyranoside, 5Br-3-indolyl- β -D-galactopyranoside becomes an inhibitor (66). Likewise, engineering these transporters may convert substrates into inhibitors, and vice versa, e.g., a pig SGLT1/SGLT3 chimera transports phlorizin with a $K_{0.5}$ of $4.5 \mu\text{M}$ and a maximum transport rate comparable to that for glucose (161).

C. Inhibitors

The classic competitive inhibitor of SGLTs is phlorizin {Fig. 18A, natural dihydrochalcone glucoside (1-[2- β -D-glucopyranosyloxy)-4,6-dihydroxyphenyl]-3-(4-hydroxyphenyl)-1-propanone} (see an excellent review by Ehrenkranz et al., Ref. 44). Phlorizin is a β -glucoside comprised of two aromatic rings (A and B) joined by an alkyl spacer of three carbons. As with the aglycone phloretin, it undergoes a *keto-enol* tautomerization (52, 242), with the *keto*-form being the higher affinity configuration (32, 66).

The phlorizin K_i for hSGLT1 is 200–300 nM, but the K_i varies among different isoforms, e.g., rat SGLT1 K_i =

12 nM and rabbit SGLT1 K_i = 760 nM (66, 69, 159, 164). hSGLT2 has an order of magnitude higher affinity for phlorizin (K_i = 10–39 nM, Refs. 81, 88, 159), despite its 10-fold lower apparent affinity for glucose (6 vs. 0.5 mM).

The flexible structure of phlorizin makes predictions about its three-dimensional structure in the binding site uncertain (Fig. 18A). First we assume that since phlorizin is a competitive inhibitor, the glucose is bound at the same site as the free glucose: this is reasonable given that the hSGLT1 K_i for phlorizin, 200 nM, is 250 times lower than that for the aglycone phloretin, 50 μM (66). We propose that the B-ring is canted 30° to the plane of the sugar as for phenyl- β -D-glucopyranose. Possible configurations of the A-ring range from that for the X-ray crystal structure, an extended conformation with the aglycone in roughly the same plane as the pyranose ring (Cambridge Structural Database code CEWWAC), to that from solution NMR studies and computer conformational searches, which predict that that A-ring folds back over the B-ring (161, 242). The energetic differences between the different conformations are small, so it is not clear how realistically computational methods can be employed to predict the bound conformation.

Nevertheless, analysis of the physical characteristics of the aglycones combined with their kinetics (Table 5) allowed us to create a pharmacophore model of the inhibitor binding site, and predict interactions of the aglycone with SGLT1 that determined binding (Fig. 18B) (66). We predicted that there is a flat hydrophobic surface of at least $7 \times 12 \text{ \AA}$ extending from the sugar binding site with an orientation similar to the plane of the pyranose. Many of these inhibitors are relatively flexible, and conformational analyses predict folded solution structures. A study focused on phlorizin (242) predicted the binding structure being a folded conformation occupying a $13 \times 10 \times 17 \text{ \AA}$ volume, an arrangement similar to the structure shown by Panayotova-Heiermann (161) and Figure 19. Independent of the actual conformation, the pharmacophore predicts that there are three locations where H-bonds can be donated and accepted, one point where an H-bond is donated from the protein, and one area in which an H-bond is detrimental (66). Phlorizin can be docked into homology models of SGLT1 and -2 with glucose in the sugar binding site and the aglycone in either the enol or keto conformation (V. Chaptal and B. A. Hirayama, unpublished data).

Given that hSGLT2 is 59% identical to hSGLT1 and is expected to share the same architecture, how, then, does one produce a specific SGLT2 inhibitor?

Over the past decade, several pharmaceutical companies have attacked this problem experimentally by modifying the phlorizin structure to enhance selectivity for SGLT2 over SGLT1. Phlorizin has a greater than four-fold higher affinity for hSGLT2 ($K_i \sim 40 \text{ nM}$) than hSGLT1 ($\sim 200 \text{ nM}$) (81, 88, 159). The first report of an effective

TABLE 5. Glucoside interactions with SGLT2

Substrate/Inhibitor	hSGLT1	hSGLT2	pSGLT3
<i>Transported glucosides ($K_{0.5}$, mM)</i>			
2-Naphthyl- β -D-glucose	0.5 ⁴		0.2 ⁴
Indican	0.05 ⁴	0.1 ¹⁸	0.9 ⁴
Phenyl- β -D-glucose	1.6 ⁴	0.3 ¹⁸	7.9 ⁴
Arbutin	1.4 ^{4,14}		1.2 ⁴
Helicin	14 ¹⁴		
Glufosfamide	Poor ¹⁶		1 ¹⁶
<i>Glucoside inhibitors (K_i, K_d, or EC_{50}, mM)</i>			
Phlorizin	0.0002 ^{6,8,9,11,18}	0.00007 ^{1,8,9,11,18}	0.009 ¹³
Phloretin	0.05–0.14 ^{6,11}	0.025 ¹¹	
4-Methylumbelliferyl- β -D-glucopyranoside	8 ^{4,6}		3.3 ⁴
8-Hydroxyquinoline- β -D-glucopyranoside	6 ^{4,6}		~40 ⁴
Esculin	15 ^{4,6}		NI ⁴
1-Naphthyl- β -D-galactopyranoside	0.9 ^{4,6}		NI ⁴
2-naphthyl- β -D-galactopyranoside	7 ^{4,6}		NI ⁴
Deoxyrhapontin	0.025 ⁶		
Rhapontin	0.2 ⁶		
5Br-6Cl-3-indolyl- β -D-galactose	0.14 ⁶		
5Br-3-indolyl- β -D-galactose	0.18 ⁶		
T-1095 ^a	0.0002 ^{8,9}	0.00003 ^{8,9}	
Sergiflozin	0.0021 ¹¹	0.00001 ^{8,11}	
Compound 5	>0.008 ⁸	0.0013 ⁸	
Dapagliflozin	0.0014 ⁸	0.000001 ⁸	
6'-O-Spiroglucoside	0.01–0.1 ¹⁰	0.000071 ¹⁰	
6'-O-Spiroglucoside-Cl	0.00062 ¹⁰	0.000007 ¹⁰	
2'-O-Spiroglucoside	>.0001 ¹⁰	>>0.00001 ¹⁰	
Salicin			NI ¹³
Helicin			NI ¹³
2-Nitrophenyl- β -D-glucopyranose			NI ¹³
4-Nitrophenyl- β -D-glucopyranose			transported 33% α MDG ¹³

Glycosides can be transported or be inhibitors. The apparent affinities of these compounds for hSGLT1, hSGLT2, and pSGLT3 are compared as $K_{0.5}$ for transported substrates, or K_i or EC_{50} for inhibitors. * K_b , or estimate of inhibition. ¶Value estimated from graph in paper. NI, no interaction. § EC_{50} . ‡ K_d . #rbSGLT1. References are as follows: hSGLT4: ¹Ref. 214; hSGLT1: ⁴Ref. 37, ⁵Ref. 38, ⁶Ref. 66, ¹⁷Ref. 67, ¹⁸Ref. 81, ¹⁹Hirayama and Wright, unpublished data; rat SMIT2: ²Ref. 3, ¹⁵Ref. 21; canine SMIT1: ³Ref. 58; hSGLT3: ⁷Ref. 235, ¹⁵Ref. 35, ¹³Ref. 138; hSGLT2: ⁸Ref. 81, ⁹Ref. 156, ¹⁰Ref. 255, ¹¹Ref. 159, ¹²Ref. 86; rbSGLT1: ¹⁴Ref. 136; pSGLT3: ¹⁶Ref. 234.

SGLT2 inhibitor was T-1095A, a phlorizin derivative created by research groups at Tanabe Seiyaku (156), that could be delivered orally in a pro-drug strategy. Selectivity for SGLT2 was accomplished by substituting a methyl group for the *meta* hydroxyl of the B-ring, and creating an aromatic five-membered ring of the *para*-OH of the A-ring (Fig. 18A). The pro-drug was absorbed without interacting with the intestinal SGLT1, and the active drug had a fourfold increase in SGLT2/SGLT1 selectivity.

We will present a brief synopsis of the continuing evolution of specific hSGLT2 inhibitors. A more detailed discussion of intermediate structures is available in pharmaceutical reviews (e.g., Refs. 83, 147, 237). Since the description of T-1095A, several groups have addressed the SGLT1/SGLT2 specificity problem. Approaches of note are Sergiflozin-A, Dapagliflozin, and 6'-O-spiro-C-aryl glucosides (Fig. 19), as each represents advances in the phlorizin modification strategy. In the initial investigation of glucoside transport and binding to SGLT1, the importance of the glycosidic oxygen was noted, as was the observation that a β -linked hydrophobic/aromatic structure could be accommodated in the binding site. This

model is followed in phlorizin, T-1095A, and Sergiflozin-A. Sergiflozin-A is a β -glucopyranoside in which the A-ring is joined to the B-ring by only one carbon rather than the three carbons of phlorizin and T-1095A (88). Both hydroxyls of the B-ring and the carbonyl oxygen in the linker are absent. The *para* hydroxyl of the A-ring of phlorizin is replaced by a methoxy group. These changes resulted in an increase in SGLT2/SGLT1 selectivity (to 210:1) and an increase in SGLT2 affinity (K_i 2–10 nM) (88, 159).

Dapagliflozin is a further departure from the phlorizin plan (147) as it is a C-aryl glucopyranoside, i.e., the B-ring is directly linked to the pyranose ring in an equatorial configuration, eliminating oxygen 1. The A- and B-rings are still linked by a single carbon, but the B-ring has a chloro group *para* to the sugar, and the A-ring is attached in the *meta* position. The A-ring has a *para* ethoxy group. These modifications improved SGLT2: SGLT1 selectivity (1,200:1) and affinity for SGLT2 (EC_{50} = 1.1 nM). Given the specificity profile of hSGLT1 (Table 5), this increase in affinity in the absence of the glycosidic oxygen was initially surprising, but we note that this requirement may not hold for all SGLT isoforms (Table 2):

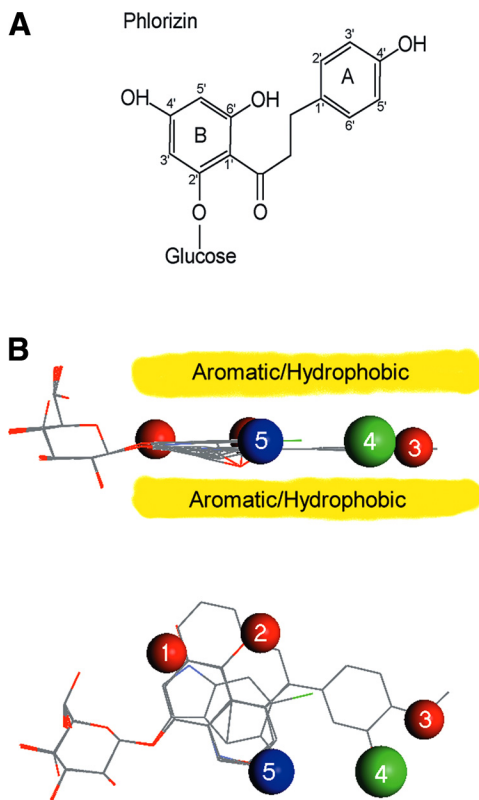


FIG. 18. Phlorizin and a 3-dimensional pharmacophore for hSGLT1. *A*: chemical structure of phlorizin showing the A and B rings. *B*: an inhibition pharmacophore for hSGLT1 was constructed by comparing strength of inhibition of hSGLT1 function by aromatic glucosides with potentially interacting groups placed at different positions on the rings. Red spheres indicate a region where hydrogen bond donation and acceptance are favorable; the blue sphere is the location where only hydrogen bond donation is allowed, and the green sphere designates the area where hydrogen bonding is detrimental. The yellow region shows the extent of the planar surface for aromatic/hydrophobic interactions. The space was generated by overlaying seven structures that represent the diverse regions and types of interactions tested: salicin, arbutin, two conformations of 2-naphthyl galactopyranoside, 1-naphthyl galactopyranoside, rhamnose, and 5-Br-6Cl-3-indolyl-galactopyranoside. [From Hirayama et al. (66).]

in hSGLT3, the $K_{0.5}$ for 1-deoxyglucose is only reduced by a factor of 2 compared with the 20-fold decrease for SGLT1.

The third example is an *O*-spiro modification of dapagliflozin where the orientation of the B-ring is locked in position by creating a five-membered ring of the α -oxygen and the B-ring of the aglycone (Fig. 19) (255). This compound showed that the presence of the substituent at the *para* position of the A-ring was important for SGLT2 binding, and the 6'-*O*-spiro compound was preferred over the 2'-*O*-spiro construct, helping to more clearly define the orientation of the B-ring. However, no gain in selectivity over that of dapagliflozin was reported.

The development of selective SGLT2 inhibitors was mostly accomplished with an increase in affinity for hSGLT2 and a reduction in affinity for SGLT1: the hSGLT1

K_i (or rather EC_{50}) values for these inhibitors increased by roughly an order magnitude (Fig. 18). The pharmaceutical implications of the SGLT2 inhibitors are addressed in section **XIVH**.

IX. ION SELECTIVITY

SGLTs are exquisitely selective for Na^+ as the energizing cation. Apart from H^+ and Li^+ , no other monovalent cation can replace Na^+ to drive glucose transport (82, 166). The cation $K_{0.5}$ values were 4 mM for Na^+ , 12 mM for Li^+ , and 7 μM for H^+ at -150 mV (68, 175). The maximum velocities were similar, and Hill coefficients were greater than 1. There was a kinetic penalty for substituting Na^+ with Li^+ or H^+ in that the apparent affinity for sugar decreased by 1–2 orders of magnitude: $K_{0.5}^{MDG}$ increased from 0.15 to 4 and 20 mM. One interpretation of the cation selectivity data is that cation binding initiates a change of the conformation of the sugar binding site: the conformations induced by Li^+ and H^+ binding are perturbed relative to the Na^+ -bound transporter. The agreement between the Na^+ to glucose transport stoichiometry (2:1) and the Na^+ Hill coefficient in SGLT1 and pig SGLT3 has led to the conclusion that these proteins have two strongly interacting Na^+ binding sites (34, 139). On the other hand, hSGLT2 only has one Na^+ binding site (81). One study examined the

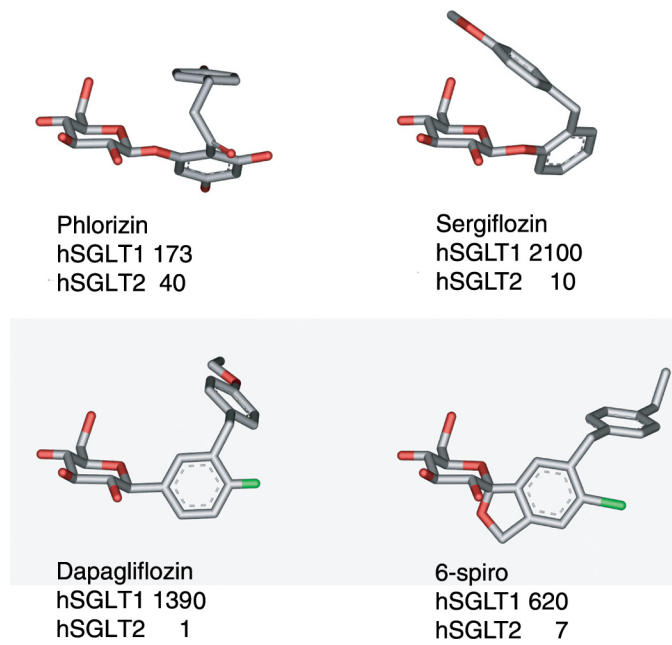


FIG. 19. SGLT2 inhibitors. Representative conformations of the hSGLT2-selective inhibitors sergiflozin, dapagliflozin, and the 6-spiro modification of dapagliflozin are compared with phlorizin. The structures are aligned on the glucopyranose. EC_{50} values (nM) for each compound are listed for hSGLT1 and hSGLT2 for comparison. These structures represent favorable (low energy) configurations resulting from conformational searches (*in vacuo*) of the rotatable bonds.

effect of anions on SGLT1 activity (126) and showed that replacing Cl⁻ with gluconate or MES [2-(N-morphino)ethanesulfonic acid] decreased the apparent affinity of SGLT1 for Na⁺ ($K_{0.5}^{\text{Na}}$ increased from 41 to 62 mM at -50 mV), whereas the effect on apparent affinity for αMDG was small (<10%). Cl⁻ had no effect on maximal transport rate.

What does the crystal structure of vSGLT tell us about the Na⁺ binding sites? First, it should be made clear that crystallographic assignment of Na⁺ binding sites is nontrivial, even for proteins with much higher resolution structures than are currently available for membrane transport proteins (157, 158). The problem is that Na⁺ has a small ionic radius of 0.97 Å and the same number of electrons as water, and there are no electron-dense cations that can substitute for Na⁺.

Even in the case of the highest resolution structure of a cotransporter to date (LeuT 1.65 Å, Ref. 256), the two Na⁺ binding sites (Na1 and Na2) were assigned based on modeling density peaks as water or Na⁺, valence calculations, and consideration of coordination distances. [Significantly, neither Na1 nor Na2 sites have been identified in Na⁺-independent transporters in the LeuT structural family (50, 54).] Both LeuT Na1 and Na2 sites are near the unwound sections of TM helices and involve five or six coordinating atoms, mostly backbone carbonyls. The major difference between the two sites is that the negatively charged group of the substrate (carboxyl group of leucine) contributes to the coordination of Na1, while Na2 is constructed from polar/neutral groups (carboxyl oxygens from Gly-20, Val-23, and Ala-351 and hydroxyl oxygens from Thr-354 and Ser-355; see Fig. 16B). Molecular dynamic simulations of ion selectivity of the LeuT Na1 and Na2 sites suggest, as predicted, the Na1 site is more selective for Na⁺/K⁺ than Na2 (5,000 vs. 400) (152).

One sodium site corresponding to Na2 of LeuT has been assigned to vSGLT (Fig. 16B) (1, 48). This is ~10 Å away from the sugar binding site with the coordinating residues from TM1 (A62, I65) and TM8 (A361, S364, S365). An equivalent site is found in the Mhp1 and BetP transporters, but the Na1 site is only found in LeuT and BetP. The presence of one or two sites is consistent with the 1:1 and 2:1 Na⁺/substrate coupling ratio reported for these transporters. Experimental evidence for the importance of the Na2 site S365A in vSGLT was the abolition of transport by S365A (48), and in the homologous Na2 site in hSGLT1 the mutation S392A reduces both Na⁺ and sugar affinities (Loo, Hirayama, Sala-Rabanal, and Wright, unpublished data). Molecular dynamic simulations of mutations at the LeuT Na2 site predict that the mutations S355A and T354A increase the Na⁺/K⁺ selectivity and T354A increase the Li⁺/Na⁺ selectivity (Sergei Noskov, personal communication).

Close inspection of the superimposed Na2 sites in core vSGLT, LeuT, and Mhp1 structures shows that TM1

and TM8 are shifted away from each other in vSGLT (1). The Na⁺ coordinating distances are larger (3.1–3.8 Å) in vSGLT than in LeuT (2.2–2.5 Å), suggesting that in vSGLT the cation has access to the cytoplasmic aqueous vestibule. This is supported by molecular dynamic simulations indicating that Na⁺ is bound tightly to the Na2 site in LeuT, but in vSGLT Na⁺ can escape into the cytoplasmic aqueous vestibule and, after a transient interaction with D186, into the cytoplasm (117, 238).

X. KINETICS

The high level of expression of SGLT1 in heterologous systems has led us to revisit the questions of SGLT1 kinetics using voltage-clamp methods. One significant advance has been the ability to record the kinetics as a function of membrane potential and external sugar, sodium, and phlorizin concentrations in a single cell. In addition, it is now possible to control the composition of the intracellular compartment using either the cut-open oocyte or patch-clamp preparations (17, 47, 81, 191). Another major advance was our introduction of fast perturbation techniques developed for enzymology to the field of cotransporters. We used rapid jumps in membrane potential to record the transient capacitive SGLT currents as a function of external Na⁺, sugar, and phlorizin (pre-steady-state kinetics)(127). The significance is that for the first time one can study partial reactions in the overall transport cycle.

Relatively little is known about the transport kinetics of other human SGLTs: SGLT2 is expressed poorly in heterologous expression systems, where the rate of transport is generally orders of magnitude less than that for SGLT1 (81, 86). Human SGLT3 is not a transporter but instead a glucose sensor (35). Pig SGLT3 (originally designated pig SGLT2) is a transporter with a common transport mechanism to hSGLT1 (34, 138). Only limited information is available for SGLT4, -5, and -6 (SMIT2) (21, 113, 118, 214).

A. Steady-State Kinetics

1. Inward transport

As discussed above (Figs. 3 and 4), the activity of hSGLT1 can be monitored as an inward sodium current generated by glucose, and the kinetics can be determined by recording the currents as a function of voltage and the external sugar, cations, and inhibitor concentrations (see Fig. 4B for αMDG and 3FDG in a single oocyte). The protocol that is commonly employed in oocytes expressing hSGLT1 is illustrated in Figure 20. The cell membrane potential is voltage clamped at -50 mV and then rapidly stepped to voltages ranging from +50 to -150 mV for 100

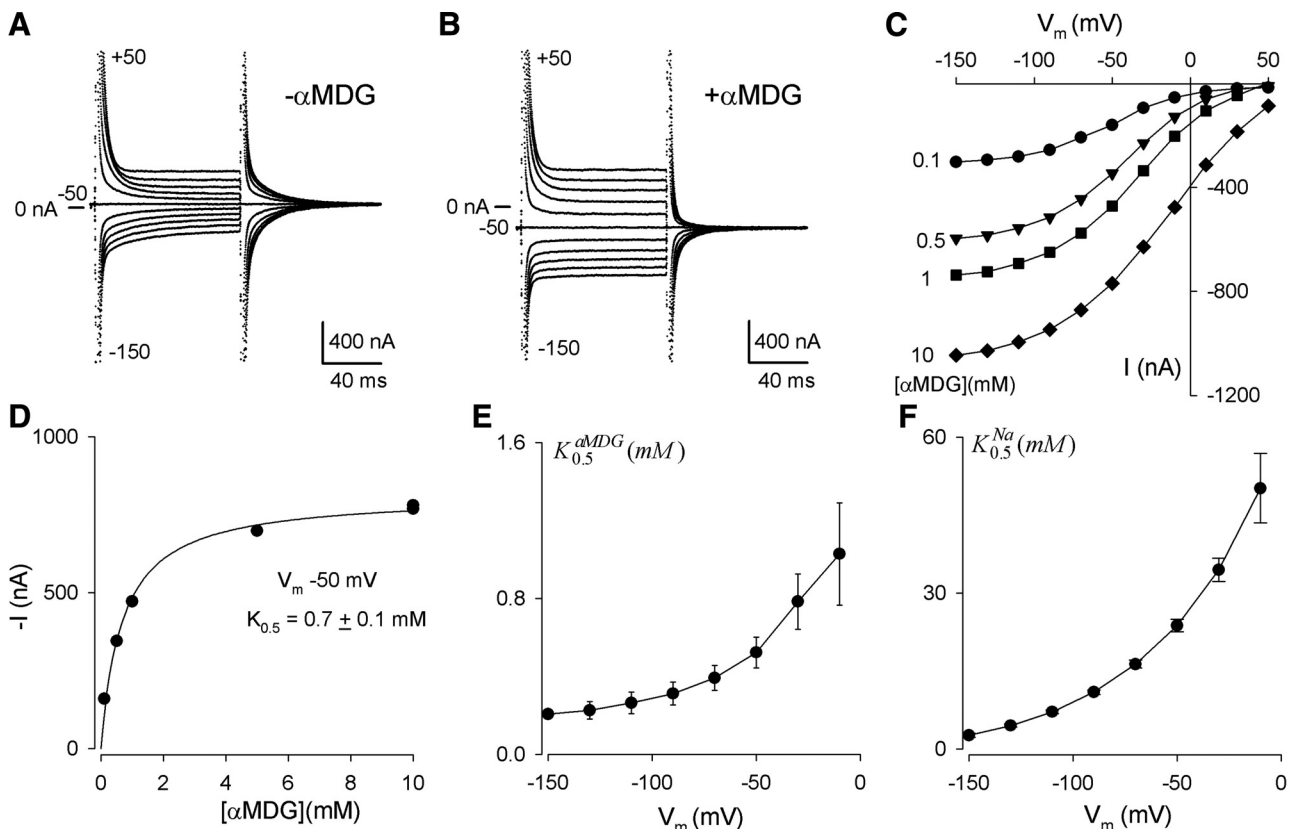


FIG. 20. Kinetics of Na^+ /sugar transport by hSGLT1. Total current records from an oocyte expressing hSGLT1 bathed in NaCl buffer are shown. *A*: in the absence of sugar. *B*: with 0.3 mM α MDG added to the external solution. Membrane potential was clamped at $-50 and stepped to a series of test voltages for 100 ms (+50 to $-150). *C*: current-voltage relations of the sugar-induced current, obtained by subtracting the baseline current in the absence of sugar from the current in the presence of sugar. *D*: dependence of the sugar-induced current on sugar concentration. The curve was drawn according to the equation: $I = I_{\max} [\alpha\text{MDG}] / ([\alpha\text{MDG}] + K_{0.5}^{\alpha\text{MDG}})$. *E*: dependence of $K_{0.5}^{\alpha\text{MDG}}$ on voltage. *F*: dependence of $K_{0.5}^{\text{Na}^+}$ on voltage. (From B. Moy, C. Lu, D. D. F. Loo, and E. M. Wright, unpublished data.)$$

ms, first in the absence of substrate (Fig. 20A) and then in the presence of different external cation and sugar concentrations (Fig. 20B). Note that the practical range of test potentials, +50 to -150 mV, is limited by the stability of the cell membrane, i.e., without artifacts from voltage-activated endogenous channels or dielectric breakdown.

In the experiment illustrated in Figure 20, the external Na^+ concentration ($[\text{Na}^+]_o$) was 100 mM, and the α MDG concentration ($[\alpha\text{MDG}]_o$) was varied between 0 and 10 mM. In both the presence and absence of sugar, the currents approached a steady-state value 95–100 ms after stepping the membrane potential (V_m) to each test value, and returned to the original holding potential with a similar time course. The difference between the steady-state currents obtained in the presence and absence of sugar at each voltage step gives the current-voltage (I - V) curve at each sugar concentration (Fig. 20C). Note that the I - V curves approach zero current at positive V_m values and saturate at hyperpolarizing voltages, i.e., transport has voltage-sensitive (between +50 and -100 mV) and voltage-insensitive (-100 to -150 mV) kinetics.

The substrate-coupled current (I) was empirically described by the relationship:

$$I = I_{\max}^S [S]^n / \{ (K_{0.5}^S)^n + [S]^n \} \quad (1)$$

where $[S]$ is the external substrate concentration (cation or sugar substrate), I_{\max}^S is the maximal substrate-induced current, $K_{0.5}^S$ is the half-maximal substrate concentration, and n is the so-called Hill coefficient.

In the experiment illustrated, the $K_{0.5}$ for α MDG was 0.7 mM at -50 mV (Hill coefficient set to 1) (Fig. 20D), and the $K_{0.5}$ decreased towards a minimum value of 0.2 mM at -150 mV (Fig. 20E). In the same oocyte, the currents induced by α MDG were also recorded as the Na^+ concentration was varied between 0 and 100 mM and fit to Equation 1 (not shown), and the apparent $K_{0.5}$ for Na^+ was plotted against voltage in Figure 20F. The Na^+ $K_{0.5}$ was voltage dependent ranging from 60 mM at 0 mV to a minimum value of 0.8 mM at -150 mV. The Hill coefficient for Na^+ was 1.5 and independent of voltage.

Steady-state kinetics provides insights into the order of substrate binding, as well as whether the substrates are transported sequentially or simultaneously. For example, in a strictly ordered system, if glucose is the last molecule to bind, then the maximal transport rate for sugar (I_{\max}^S , determined by maintaining $[\text{Na}^+]$

constant while varying sugar concentration) is independent of Na^+ concentration; conversely, if Na^+ binds last, I_{\max} for Na^+ (I_{\max}^{Na} , determined by maintaining [glucose] constant while varying $[\text{Na}^+]$) is independent of glucose concentration.

We found that the I_{\max} for sugar (αMDG) at saturating voltages (-150 mV) was independent of the Na^+ concentration (Fig. 21C), whereas I_{\max} for Na^+ depends on the glucose concentration (Fig. 21D). These observations indicate that external Na^+ bind to the transporter before the external sugar (167). At saturating voltages, -150 mV, the $K_{0.5}$ for Na^+ depends on the αMDG concentration (Fig. 21B), and conversely, the $K_{0.5}$ for αMDG depends on the Na^+ concentration (Fig. 21A). This mutual dependence of the $K_{0.5}$ values for Na^+ and glucose indicates that two substrates are transported simultaneously. The Hill coefficients for αMDG and Na^+ are 1 and >1.5 , respectively, consistent with measurements of sugar and Na^+ stoichiometry. The binding of the two Na^+ to the transporter before glucose is also supported by fluorescence experiments (see Fig. 25B).

$\text{Na}^+/\text{glucose}$ cotransport has large temperature dependence, temperature coefficient $Q_{10} > 3$, or activation energy $E_a > 20$ kcal/mol, i.e., much greater than for chan-

nels (145, 168). There was no temperature effect on the apparent affinities of rabbit SGLT1 for either Na^+ or glucose, but the maximum rate of transport increased with a Q_{10} of ~ 3 (168).

2. Outward transport

Outward Na^+/sugar currents were also measured as a function of voltage and internal Na^+ (0 – 500 mM) and sugar (0 – 500 mM) concentrations when the external solution contained 10 mM Na^+ and no sugar, i.e., the reverse of inward current measurements (see Fig. 6; Refs. 47, 191). In contrast to the inward Na^+/sugar currents, which saturated with large hyperpolarizing voltages and approach zero at large depolarizing voltages (Fig. 20C), the outward Na^+/sugar currents saturated at 0 mV and approached zero at -150 mV. The internal $K_{0.5}$ for sugar was ~ 40 mM at 0 mV (with internal Na^+ concentration of 500 mM). The outward current decreased as the internal Na^+ was lowered from 500 to 0 mM with a sodium $K_{0.5}$ of 45 – 50 mM when the data were fit with a Hill coefficient of 2. Model simulations indicate that if sugar is dissociated before Na^+ , there would be sugar *trans*-inhibition, i.e., inhibi-

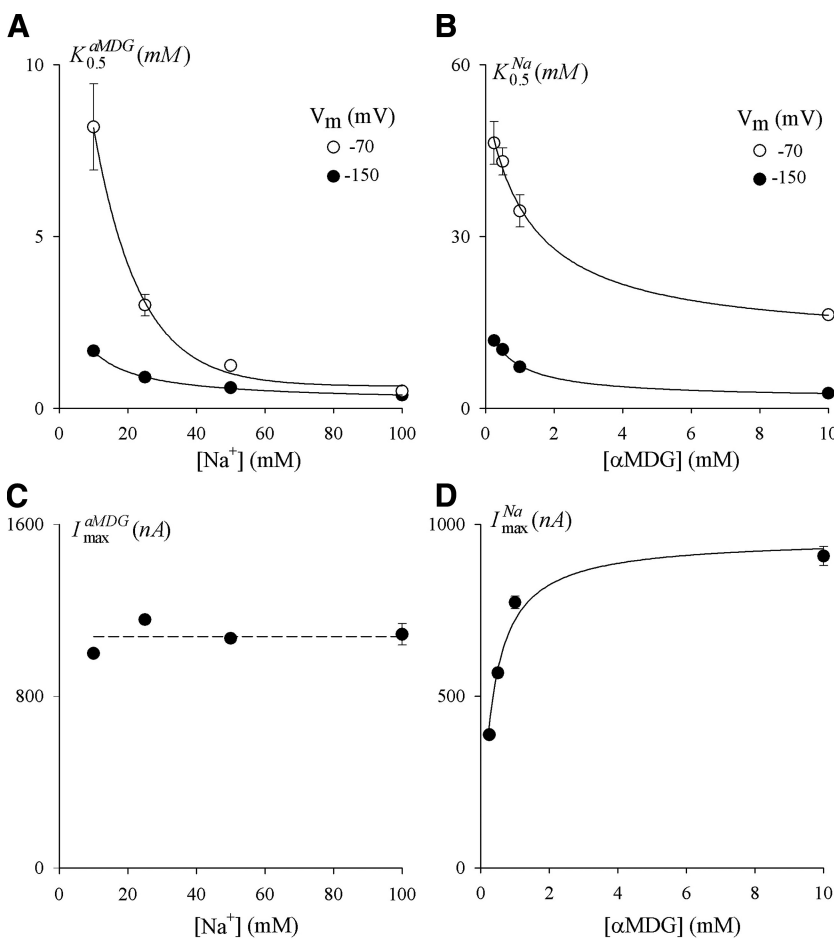


FIG. 21. Dependence of the steady-state kinetic parameters $K_{0.5}$ and I_{\max} on $[\text{Na}^+]$ and $[\alpha\text{MDG}]$. The experiment was performed on an oocyte expressing the hSGLT1. A and C show the dependence of $K_{0.5}$ and I_{\max} for αMDG on $[\text{Na}^+]$. The $K_{0.5}$ values are shown for V_m at -70 and -150 mV. The maximal transport rate (I_{\max}) was determined at -150 mV. B and D show the dependence of the $K_{0.5}$ and I_{\max} for Na^+ on $[\alpha\text{MDG}]$. Error bars represent the SE of the estimates. The curves in A, B, and D were drawn by eye, and the dashed line in C is the mean of the data values. Same cell as in Figure 20.

tion of inward Na^+ /glucose cotransport at hyperpolarizing membrane potentials by internal sugar but not Na^+ (167). Sugar *trans*-inhibition has also been demonstrated in brush-border membrane vesicles (91).

B. Pre-Steady-State Kinetics

Understanding the mechanism of SGLT1 has been revolutionized by our discovery of SGLT capacitive currents, or charge movements. These are the carrier counterparts of the gating currents of voltage-gated ion channels and are thought to arise from movement of charged and/or polar residues in response to changes in the membrane electric field (11, 127–129, 166; see also Refs. 18, 59, 99, 123). The carrier-mediated capacitive transients are elicited by step jumps in membrane voltage in the absence of glucose (Fig. 20A). These transients, or pre-steady-state currents, are blocked by saturating concentrations of glucose and phlorizin (Figs. 20B and 22, B and C). Pre-steady-state currents are a general property of cotransporters (see Ref. 59). So far, we have been unable to detect any hSGLT2 pre-steady-state currents (81).

The pre-steady-state current of hSGLT1 is illustrated in Figure 20A. In the absence of external sugar, the membrane potential was held at -50 mV (V_h) and then stepped to a

series of test values (from $+50$ to -150 mV in 20-mV decrements) for 100 ms (ON) before returning to V_h (OFF). In response to the voltage jump, the total current consisted of 1) an initial membrane bilayer capacitance transient which decays to steady state with a time constant τ of 1 ms, which is insensitive to Na^+ and sugar concentrations. This component was also observed in noninjected control oocytes. Integration of this transient in control oocytes gave a capacitance of 275–340 nF, and, with the assumption of a specific membrane capacitance of $1 \mu\text{F}/\text{cm}^2$, the area of the oocyte cell membrane area was $30 \times 10^6 \mu\text{m}^2$ (262). 2) SGLT1 pre-steady-state currents with time constants greater than for the membrane capacitance τ vary between 3–20 ms, and 3) SGLT1 steady-state currents consist of the background (endogenous) currents of the cell and the Na^+ currents mediated by SGLT1 (leak or uniporter currents) (166, 131). During the ON and OFF pulses, the SGLT1 pre-steady-state currents were in the opposite direction, but the total charge moved (Q_{\max}) for ON and OFF voltage jumps were identical. The SGLT1 current transients were inhibited by glucose (Fig. 20B) and phlorizin (Fig. 22, B and C) and were not observed in control cells. Increasing external α MDG concentrations reduced the charge movements (Q_{\max}) with an apparent $K_{0.5}$ of 1.1 mM, and phlorizin inhibited

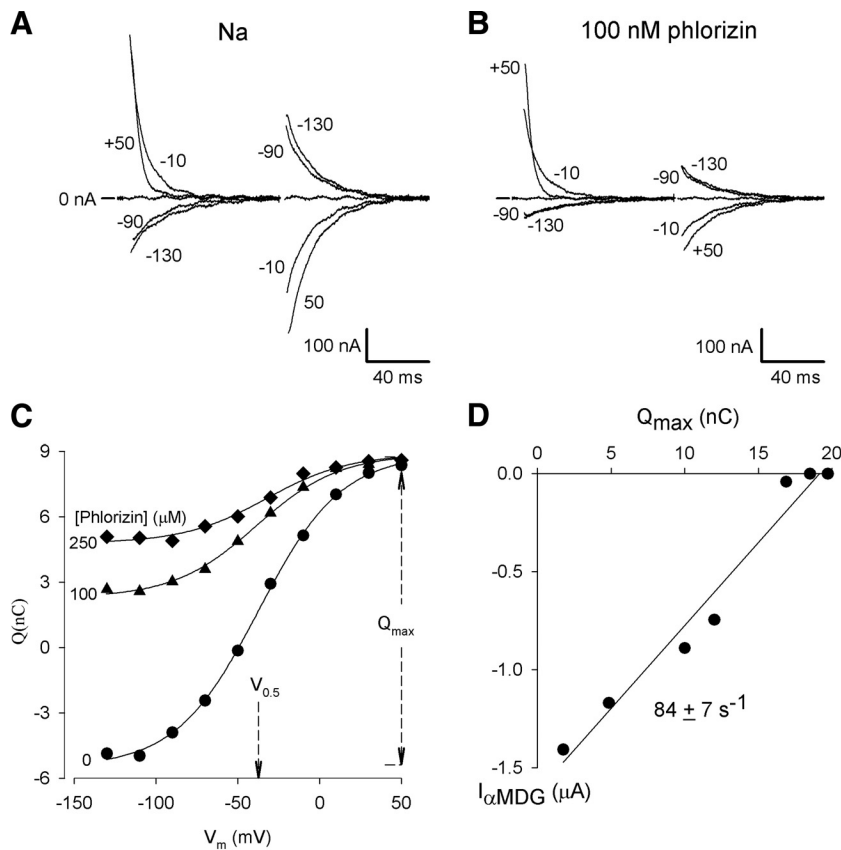


FIG. 22. Dependence of hSGLT1 presteady currents on phlorizin and glucose. A: compensated current records (at $V_m = +50, -10, -90$, and -130 mV) in 100 mM NaCl buffer. $V_h = -50$ mV. B: current records with 100 nM phlorizin added to the external solution. C: dependence of charge movements (Q) on phlorizin. The curves were obtained from the Boltzmann relation and have been shifted to align at the depolarizing limit (in the absence of phlorizin). Maximal charge Q_{\max} is the difference in Q between the depolarizing and hyperpolarizing limits. Q_{\max} is decreased with increasing [phlorizin]. $V_{0.5}$ is the midpoint of the Q - V curve and is unaffected by [phlorizin]. For this oocyte, $V_{0.5}$ is -37 mV. D: relation between Q_{\max} and maximal sugar transport rates I_{\max} . Slope of the regression line is $84 \pm 7 \text{ s}^{-1}$.

with a K_i of 100 nM (Fig. 22C). The reduction in charge by sugar was directly proportional to the increase in sugar current with a slope of 84 s^{-1} (see Fig. 22D).

The pre-steady-state current of SGLT1 can be isolated from the total current (I_{tot}) by two equivalent methods (18, 59, 123, 127): 1) point to point subtraction of the total currents in the presence and absence of saturating phlorizin and 2) fitting the total current by the equation

$$I_{\text{tot}}(t) = I_{\text{cm}} \exp(-t/\tau_{\text{cm}}) + I_{\text{pss}} \exp(-t/\tau_{\text{pss}}) + I_{\text{ss}} \quad (2)$$

where I_{ss} is the steady-state current, $I_{\text{cm}} \exp(-t/\tau_{\text{cm}})$ is the bilayer capacitance current with initial value I_{cm} and time constant τ_{cm} , and $I_{\text{pss}} \exp(-t/\tau_{\text{pss}})$ is the SGLT1 pre-steady-state current with initial value I_{pss} and time constant τ_{pss} .

SGLT1 pre-steady-state currents were obtained from $I_{\text{tot}}(t)$ by subtraction of the capacitive and steady-state components [$I_{\text{pss}}(t) = I_{\text{tot}}(t) - I_{\text{cm}} \exp(-t/\tau_{\text{cm}}) - I_{\text{ss}}$]. The “compensated current” records, i.e., the currents corrected for the bilayer membrane capacitive component and the steady-state current, are shown in Figure 22, A and B. For jumps to large depolarizing voltages, e.g., +50 mV, the current rose to a peak (at 1.5 ms from the onset of the voltage pulse) before decaying to the steady state (128). The implications of the rising phase of charge movement are discussed below (Fig. 25). The total charge transfer Q at each test voltage (V_m) was obtained by taking the integral of the current transients, and this was equal for the ON and OFF responses. Q shows a sigmoidal dependence on V_m (Figs. 21C and 22D), and the charge versus voltage (Q - V) curve is empirically fitted by the Boltzmann relation

$$\{(Q_{\text{dep}} - Q_{\text{hyp}})/Q_{\text{max}} = 1/[1 + \exp(z\delta(V_m - V_{0.5})F/RT)]\} \quad (3)$$

where Q_{max} is the maximal charge transfer; $Q_{\text{max}} = Q_{\text{dep}} - Q_{\text{hyp}}$, with Q_{dep} and Q_{hyp} representing the charge measured at large depolarizing and hyperpolarizing limits, respectively; and $z\delta$ is maximum steepness factor for the dependence of Q on voltage, and is the product of the apparent valence of the movable charge (z) and the fractional distance (δ) within the membrane electric field in which the charge moves. $V_{0.5}$ is the midpoint voltage or voltage at 50% Q_{max} (Fig. 22C). F is Faraday's constant, R is the gas constant, and T is absolute temperature. For Q_{hyp} to be the hyperpolarizing limit, we assume $z < 0$. In this simple treatment the Boltzmann relation is interpreted as a distribution of a movable charge between two states according to membrane voltage.

Pre-steady-state currents depend on external $[\text{Na}^+]$, suggesting that Na^+ can bind to the transporter in the

absence of the substrate. This is illustrated in Figure 23, A–C, where $[\text{Na}^+]_o$ was decreased from 100 to 25 mM. Lowering the external $[\text{Na}^+]$ causes a decrease of the transient currents in the depolarizing direction and an increase in the hyperpolarizing direction. Compared with 100 mM Na^+ , the midpoint of the distribution, $V_{0.5}$, shifts to more negative values. The Q - V curves at 100, 50, and 25 mM Na^+ were shifted to align at the depolarizing limit (Fig. 23D), and the plots show that reducing external $[\text{Na}^+]$ reduces the maximal charge (the difference between the hyperpolarizing and depolarizing limits) as well as shifted the midpoint voltage $V_{0.5}$. For the wild-type hSGLT, it is not possible to obtain the Q_{max} at 0 mM Na^+ as the Q - V curve moves out of the working range of the test voltages. However, with several hSGLT1 mutants, e.g., Y290C, substantial charge movements were observed in Na^+ -free solutions, and the complete Q - V curve fell within the –150 to +50 mV range. This demonstrated that orientation of the Na^+ -free protein contributed to the SGLT1 capacitive charge.

Attempts to identify the origin of SGLT1 charge movement by mutation of charged residues in the membrane domain have not yet been successful, but this should be revisited in light of the crystal structure. Given that the Na2 binding site in vSGLT is a neutral site (see above), we have to entertain the possibility that protein dipoles contribute to the charge movements.

The dependence of the $V_{0.5}$ on $[\text{Na}^+]$ is shown in Figure 23E. The line was obtained by linear regression with slope 93 mV/10-fold change in $[\text{Na}]_o$. The shift in $V_{0.5}$ with $[\text{Na}^+]_o$ suggests that the distribution of conformations of hSGLT1 in the membrane is dependent on $[\text{Na}^+]_o$. The occupancy of SGLT1 proteins in the charge-generating conformations is increased with increasing $[\text{Na}^+]_o$ (see below).

Figure 23F shows the dependence of the relaxation time constant (τ) of the pre-steady-state currents on membrane voltage. For the ON pulse (filled symbols), in the hyperpolarizing direction, τ (~20 ms) was relatively independent of voltage, whereas τ decreased at more positive test voltage to 3 ms (at +50 mV). The time constant for the OFF transients (open symbols), when the membrane was stepped from the test voltage (V_m) back to V_h , was independent of the test voltage (15 ms). The time constants decreased as Na^+ concentration was reduced from 100 to 25 mM $[\text{Na}]_o$ (at 0 Na^+ the time constants are below the resolution of the 2-electrode voltage clamp). Using the cut-open oocyte preparation (see Fig. 26), pre-steady current in the absence of Na^+ decayed to steady state with a voltage-independent time constant of 0.24 ms for ON and 0.17 ms for OFF voltage pulses.

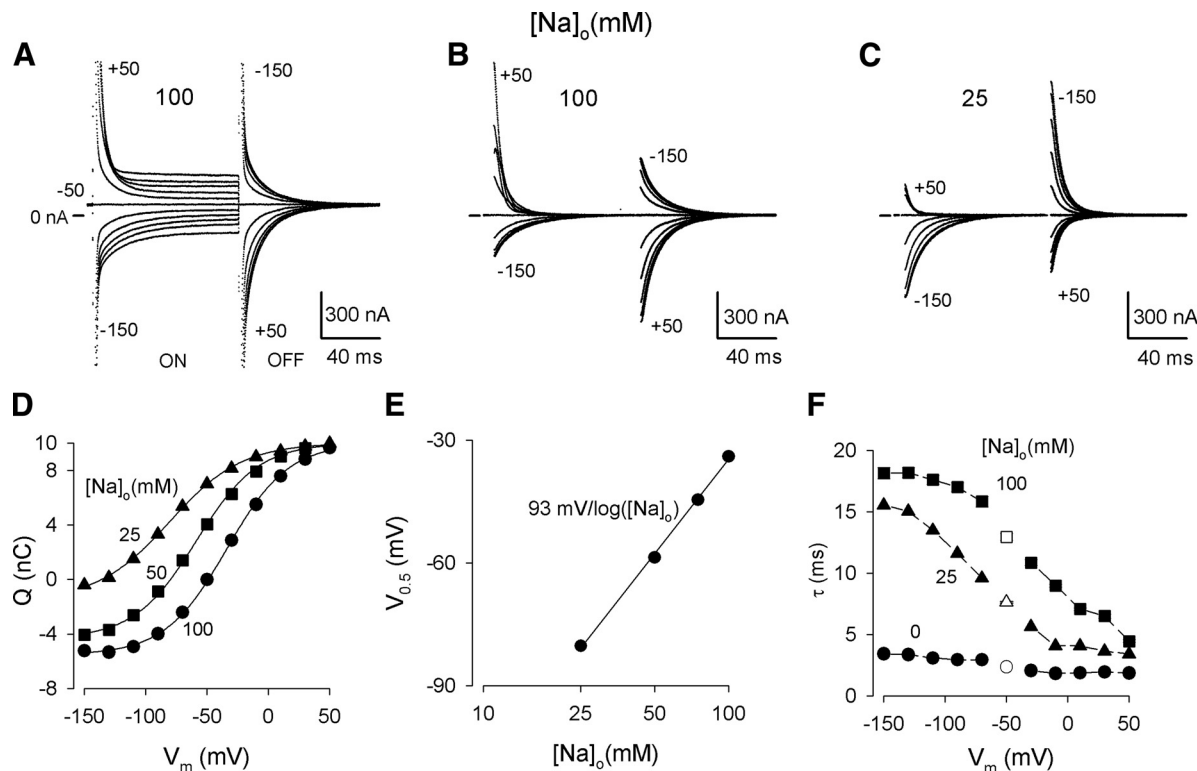


FIG. 23. Dependence of hSGLT1 pre-steady-state currents on Na^+ . *A*: total current records from an oocyte injected with cRNA coding for hSGLT1. External medium was NaCl buffer. Membrane potential was held at $V_h = -50$ mV and stepped (ON) to various test voltages (V_m) between $+50$ and -150 mV in 20-mV decrements for 100 ms before returning to V_h (OFF). The currents were obtained from the total currents by subtraction of the membrane capacitive transient and steady-state current. *C*: current records at 25 mM $[\text{Na}]_o$. *D*: charge transfer. Q was obtained from integration of the pre-steady-state currents. Q was the same for ON and OFF responses, and shown are the Q_{OFF} . At each voltage, the Q - V data were fitted (smooth curves) to the Boltzmann relation (Eq. 3). The Q - V curves at 100, 50, and 25 mM Na^+ were shifted to align at the depolarizing limit. *E*: dependence of $V_{0.5}$ on Na^+ . The slope of the regression line is $93 \text{ mV}/\log([\text{Na}])$. *F*: dependence of relaxation time constant (τ) on test voltage V_m . Shown are the τ obtained at 100, 25, and 0 mM $[\text{Na}]_o$. Na^+ free was obtained with choline replacement. Solid symbols correspond to ON pulses, and open symbols are the OFF. The time constants for OFF pulses (from V_m back to $V_h = -50$ mV) were independent of V_m .

1. Effect of sugar

The effect of sugar on pre-steady-state current is illustrated in Figure 20*B* for an oocyte in 0 and 0.25 mM α MDG. The most pronounced effect of sugar was the reduction in pre-steady-state current with hyperpolarizing voltages. With increasing $[\alpha\text{MDG}]$ (from 0 to 100 mM), there was a reduction and eventual elimination of the maximal charge Q_{max} . The reduction in Q_{max} was hyperbolic with a $\alpha\text{MDG } K_{0.5}$ of 1.1 mM. The midpoint voltage ($V_{0.5}$) shifted to more positive values with $K_{0.5}$ values similar to the $K_{0.5}$ for reduction of Q_{max} with $[\alpha\text{MDG}]$, but $z\delta$ was unaffected (127, 130). The reduction of Q_{max} and shift of $V_{0.5}$ with increasing sugar concentrations demonstrated that under sugar transporting conditions, there is a partition of SGLT1 into non-voltage-dependent states.

Since Q_{max} provides an index of the number of transporters in the oocyte plasma membrane, the turnover rate of SGLT1 can be estimated from the ratio ($I_{\text{max}}/Q_{\text{max}}$) of the maximal rate of transport (I_{max}) and maximal charge (Q_{max}), assuming $z = 1$. The turnover rate for α MDG transport by hSGLT1 at 20°C was initially estimated to be

57 s⁻¹ (127). It was revised to 28 s⁻¹ when longer duration voltage pulses (500 ms) revealed a slow component of charge movement (time constant $\tau \sim 100$ ms) contributing a maximal charge similar to that of the 20–30 ms (medium) component (128).

2. Phlorizin

Phlorizin also blocks the pre-steady-state currents. This is illustrated in Figure 22, which shows the pre-steady-state currents in absence of phlorizin (*A*) and with 100 μM phlorizin (*B*) in the bath solution. Analysis of the Q - V relations as external [phlorizin] varied from 0 to 250 μM indicates that the Q_{max} was reduced with a phlorizin K_i of 100 nM (Fig. 22*C*), but $z\delta$ and $V_{0.5}$ were unaffected (59, 66, 130). The high affinity of SGLT1 for phlorizin (K_i 200 nM) means that during the 100-ms pulse, the inhibitor has locked the transporter in a phlorizin-bound state. Increasing the duration of a depolarizing pulse up to 2 s shows partial recovery of charge and so demonstrates the slow inhibitor off rate (130, see also 81).

3. Correlation between charge and expression

Q_{\max} values at saturating Na^+ can be used to estimate the number of SGLT1 proteins (N) in the plasma membrane, $N = Q_{\max}/ze$, where z is the apparent valence of the moveable charge (the limiting slope of the Q - V curve) and e is the elementary charge (127). In an oocyte with a Q_{\max} of 25 nC, this corresponds to $\sim 10^{11}$ SGLT1 molecules/cell or $10^4 \mu\text{m}^{-2}$.

Independent confirmation that the maximal charge provides an index of the number of cotransporters in the oocyte plasma membrane was obtained from freeze-fracture electron microscopy (262). Replicas of the P or cytoplasmic face of the plasma membrane of SGLT1-cRNA-injected oocytes showed an increase in the density of intramembrane particles (IMPs) with diameter 7–8 nm compared with control oocytes (262). There was a direct correlation between particle density and charge density, and the slope gives an estimate of ~ 3.5 charges per SGLT1 molecule. The apparent discrepancy between the apparent valency ($z\delta = 1$) and this estimate of charge may in part be due to our simplifying assumption that the SGLT1 charge movements occur in a single step by fitting the Q - V curves to the Boltzmann relation (262).

Subsequently, we were able to demonstrate that these IMPs in SGLT1 expressing oocytes were indeed SGLT1 monomers (46). We concluded that Q_{\max} is a valid measure of the number of cotransporters expressed in the oocyte membrane.

4. Conformational changes

The demonstration that the charge movements are directly associated with protein conformation changes came from biochemical experiments where we measured the accessibility of covalent probes to a cysteine residue (Q457C) in the sugar binding site (38, 129). The hSGLT1 mutant Q457C has a similar apparent affinity ($K_{0.5}$) for Na^+ as wild-type hSGLT1 and is able to transport sugar. Sugar transport, but not the SGLT1 capacitive transients, were abolished after alkylation of the mutant by methanethiosulfonate reagents (38, 129, 146). However, inhibition of Cys-457 SGLT1 was dependent on the conformation of the transporter, as determined by the rate of inhibition of the sugar-induced current after exposure to MTSEA (2-aminoethyl methanethiosulfonate hydrobromide). Figure 24A shows an example. Initially, α MDG generated a current of 180 nA. After exposure to MTSEA in Na^+ buffer (for 80 s), the sugar-induced current was reduced to 40 nA. MTSEA inactivation was reversed by washing the oocyte in DTT (dithiothreitol, 10 mM). In the second part of the experiment, the inhibition of transport by MTSEA was blocked by the presence of sugar (Fig. 24B). It was further demonstrated that the accessibility to Cys-457 to MTSEA was dependent on the presence of external Na^+ and was blocked by phlorizin: there was no reduction in α MDG-

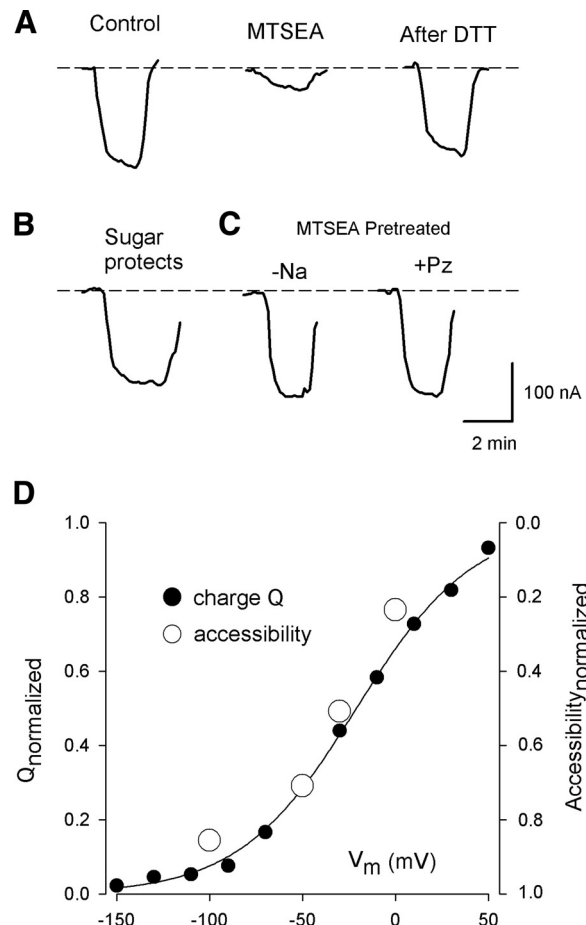


FIG. 24. Dependence of effect of MTSEA on protein conformation in hSGLT1 mutant Q457C. The ability of $1 \mu\text{M}$ MTSEA to label the cysteine at residue 457 was influenced by substrate binding and membrane voltage. The oocyte was voltage-clamped at -50 mV in Na^+ buffer, and bath composition was varied. Effects of MTSEA were measured as the current generated by 200 mM α MDG. Between all of the experiments, the oocyte was washed in 10 mM DTT for 15 min before equilibration in Na buffer. Dashed line indicates baseline holding current. A: control experiment demonstrating MTSEA inactivation of sugar transport was reversible. B: sugar protected against MTSEA inactivation. C: dependence of MTSEA inactivation on Na^+ and phlorizin. D: correlation of the voltage dependence of Q457C accessibility and the pre-steady-state charge movement. Accessibility was measured as the extent of inhibition of the sugar-induced current (unity is 100%) after 1-min exposure to $10 \mu\text{M}$ MTSEA. The relative voltage sensitivity was obtained by normalizing the accessibility at the holding potential (-50 mV) to the charge. At each test voltage, the charge Q was obtained by integration of the pre-steady-state currents. The curve was the fit of the Q - V data to the Boltzmann relation (Eq. 3). $Q_{\max} = 13 \text{ nC}$, $z = 0.8$, and $V_{0.5} = -21 \text{ mV}$. The data have been normalized between 0 and 1 (129).

induced current if the oocyte was pretreated with MTSEA in the absence of Na^+ (choline replacement) or in the presence of Na^+ and $100 \mu\text{M}$ phlorizin before testing for α MDG transport (Fig. 24B).

In addition to ligands, accessibility of Cys-457 hSGLT1 to MTSEA was dependent on membrane voltage. The accessibility of MTSEA to Cys-457 was determined when the membrane potential held at different values between -90 and $+30 \text{ mV}$, and is compared with

the Q - V relation of the pre-steady-state current in the same oocyte (Fig. 24D). The close correlation between charge movement and changes in MTSEA accessibility demonstrated that the Q - V relations represent the distribution of SGLT1 proteins between the outward-facing Na^+ -bound conformation and the inward-facing empty carrier.

5. Voltage-clamp fluorometry

The correlation between charge movement and protein conformational changes is further supported by voltage-clamp fluorometry (Fig. 25) measurements (129, 146). Fluorophores such as tetramethyl-rhodamine are sensitive to their local environment. A change in fluorescence therefore indicates that the protein conformation has changed, for example, moving tetramethyl-rhodamine

from a hydrophobic to a polar environment (such as aqueous external solution) would decrease its fluorescence intensity. The charge and fluorescence measurements are complementary. SGLT1 capacitive charges are associated with global conformational changes of the transporter [the apparent valence of the movable charge, $z = z_1\delta_1 + z_2\delta_2 + \dots + z_n\delta_n$, is the sum of the product of all movable charges (z_i) and the displacement of each charge (δ_i) in the membrane electric field], while changes of fluorescence reflect changes in the local environment of the fluorophore.

In the absence of sugar, Na^+ can interact with SGLT1. This is illustrated in Figure 25A, which shows the time course of rhodamine fluorescence on an oocyte expressing Q457C labeled with TMR6M (tetramethyl-rhodamine-6-maleimide) as the cation in the external solution is

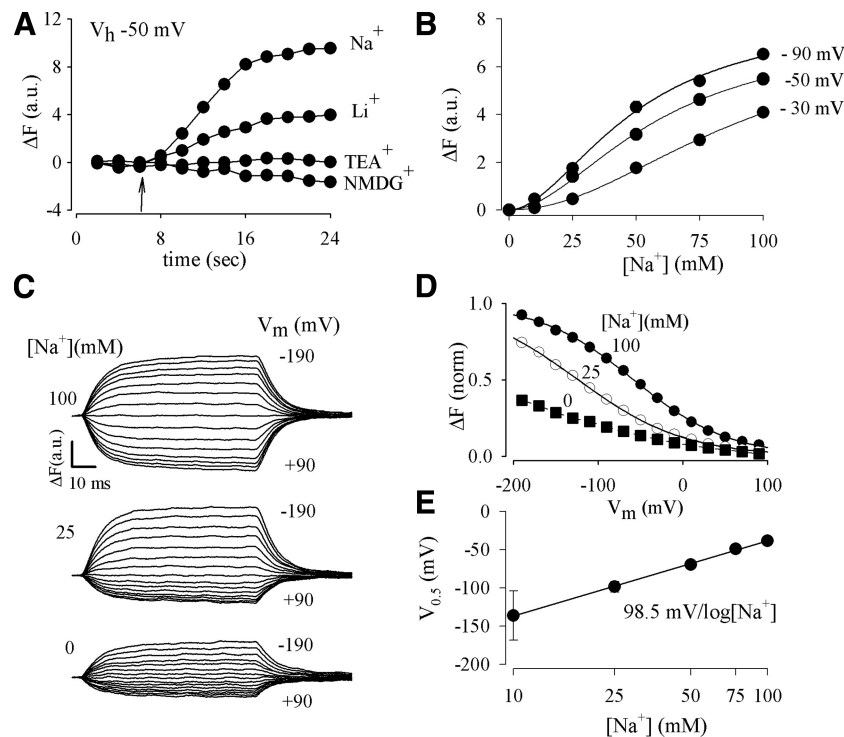


FIG. 25. Dependence of fluorescence on Na^+ . Oocytes expressing Q457C were labeled with TMR6M. The experiments were performed using a two-electrode voltage clamp on the stage of an inverted epifluorescence microscope. Fluorescence intensity changes (ΔF) are quantified as percent change from baseline ($\Delta F/F$). ΔF is expressed in arbitrary units (a.u.). 1 a.u. represents a $\Delta F/F_{\text{total}}$ of $\sim 1\%$. A: cation dependence of fluorescence. V_m was -50 mV, and the time course of ΔF was monitored. External perfusing solution initially contained $0 \text{ mM } \text{Na}^+$ ($100 \text{ mM choline Cl}$). At the arrow, the solution was changed to either $100 \text{ mM } \text{Na}^+$, Li^+ , TEA^+ , or NMDG^+ . An upwards deflection of the traces indicates an increase in fluorescence intensity. B: kinetics of Na^+ activation. ΔF was measured as a function of $[\text{Na}^+]$. The ΔF vs. $[\text{Na}^+]$ curves are sigmoid and fitted to Eq. 1: $\Delta F = (\Delta F_{\text{max}} [\text{Na}^+]^n)/([\text{Na}^+]^n + (K_{0.5})^n)$, where ΔF_{max} is the maximal fluorescence for saturating $[\text{Na}^+]$, $K_{0.5}$ is the half-maximal concentration, and n is the Hill coefficient. At -30 mV, $\Delta F_{\text{max}} = 7.4$ a.u., $K_{0.5} = 91 \text{ mM}$, and $n = 2.0$. At -50 mV, $\Delta F_{\text{max}} = 7.5$ a.u., $K_{0.5} = 58 \text{ mM}$, and $n = 1.9$. At -90 mV, $\Delta F_{\text{max}} = 8.2$ a.u., $K_{0.5} = 49 \text{ mM}$, and $n = 1.8$. C: time course of ΔF with step jumps in voltage. V_m was initially at -50 mV and then stepped to between $+90$ and -190 mV (with 20 -mV increments). External solution contained 100 mM (top panel), 25 mM (middle panel), and $0 \text{ mM } [\text{Na}^+]_o$ (bottom panel). D: relationship between ΔF and voltage. ΔF is the difference in steady-state fluorescence between the test and holding voltages. The ΔF vs. V_m relations for 100 and $25 \text{ mM } [\text{Na}^+]$ were fitted to a Boltzmann relation (Eq. 3): $(\Delta F - \Delta F_{\text{hyp}})/\Delta F_{\text{max}} = 1/[1 + \exp(z(V - V_{0.5})F/RT)]$, where $\Delta F_{\text{max}} = \Delta F_{\text{dep}} - \Delta F_{\text{hyp}}$; ΔF_{dep} and ΔF_{hyp} are the ΔF at depolarizing and hyperpolarizing limits; F , R , and T have their usual meanings; $V_{0.5}$ is membrane potential at $50\% \Delta F_{\text{max}}$; and z is apparent valence of the charge sensor of the fluorophore. At $100 \text{ mM } [\text{Na}^+]$, $z = 0.4$, and $V_{0.5} = -50$ mV. At $25 \text{ mM } [\text{Na}^+]$, $z = 0.4$, and $V_{0.5} = -125$ mV. For comparison, the curves have been normalized to ΔF_{max} observed in $100 \text{ mM } \text{Na}^+$ and shifted to align at the extrapolated depolarizing limit. E: dependence of $V_{0.5}$ for fluorescence (ΔF) on Na^+ . The slope of the regression line is $98.5 \text{ mV}/\log[\text{Na}^+]$. [From Meinild et al. (146).]

changed. External perfusing solution initially contained 0 Na^+ (100 mM choline Cl), and membrane potential was held at -50 mV. At the arrow, the perfusing solution was changed from choline buffer to either 100 mM NaCl, LiCl, TEACl, or NMDGCl. On exposure to Na^+ , the rhodamine fluorescence intensity increased to a new steady-state value and returned to baseline (in choline) when Na^+ was removed from the perfusing solution (not shown). This increase in fluorescence intensity was specific for Na^+ and Li^+ , which can substitute weakly for Na^+ in driving sugar transport, whereas TEA $^+$ and NMDG had no effect.

The kinetics of Na^+ activation of hSGLT1 were determined by measuring the fluorescence increase (ΔF) as external Na^+ concentration varied from 0 to 100 mM with the membrane potential held constant at -30 , -50 , and -90 mV (Fig. 25B). At each holding potential, increasing Na^+ concentration increased fluorescence. Likewise, at constant $[\text{Na}^+]$, hyperpolarizing membrane potentials increased fluorescence. The ΔF versus $[\text{Na}^+]$ relationship was sigmoidal, with a Hill coefficient of 2 at all membrane potentials. We conclude in the absence of glucose, 2 Na^+ bind to SGLT1 and that there is high cooperativity between Na^+ binding to the two sites.

The time course of the fluorescence intensity changes with step jumps of the membrane voltage is shown in Figure 24C. The experiments were performed with external solution containing 100 mM (*top panel*), 25 mM (*middle panel*), and 0 mM Na^+ (choline replacement, *bottom panel*). For both hyperpolarizing and depolarizing voltage pulses, the fluorescence signal reached a steady state and was maintained until the membrane potential was returned to the holding value. From the holding potential, -50 mV, depolarizing voltages decreased the fluorescence, whereas hyperpolarizing voltages increased fluorescence.

The relation between the change in fluorescence intensity (ΔF) and the test voltage (V_m) was sigmoidal, and these were fitted to the Boltzmann equation (Fig. 24D) with parameters ΔF_{\max} (maximal fluorescence intensity change), $z\delta$ (apparent valence of the voltage sensor for fluorescence), and $V_{0.5}$ (voltage at 50% ΔF_{\max}). There was a reduction in ΔF_{\max} with decreasing Na^+ concentration. $V_{0.5}$ shifted to more negative values with decreasing $[\text{Na}^+]_o$, and the shift was 98 mV/10-fold reduction in $[\text{Na}^+]_o$ (Fig. 25E). The direction and amplitude of the shift of the $V_{0.5}$ for fluorescence, towards more negative values with a sensitivity ~ 100 mV/10-fold decrease in $[\text{Na}^+]_o$, is similar to that for charge movement (Fig. 23E). The apparent valence of the voltage sensor for fluorescence ($z\delta$) was 0.4 and was independent of Na^+ concentration. In Na^+ -free solutions, there was also a change in fluorescence with voltage jumps. This confirms that the empty transporter undergoes voltage-dependent conformational changes between the external and internal membrane surfaces. The lower apparent valence observed for the fluorescence, 0.4, than for

charge, 1.0, indicates that the fluorophore reports on local conformational changes.

6. Experimental limitations

The two-electrode voltage clamp, cut-open oocyte voltage clamp, and patch-clamp techniques have been used to study SGLT1 and other electrogenic cotransporters. Each has strengths and weaknesses. The advantage of the two-electrode voltage clamp is that the oocyte is stable for many hours, and the clamp settling time of 0.6–1.0 ms (127) can be used to record electrical and optical transients in the millisecond to second range. The relatively slow clamp speed is due to the microelectrode resistance (~ 0.5 M Ω) and the high membrane capacitance of the oocytes, ~ 300 nF. To measure kinetic events in the microsecond range, the cut-open oocyte voltage clamp with a settling time of 80 μ s may be used (204, 208). However, this system tends to be less stable than the two-electrode voltage clamp. Patch-clamp techniques, such as the excised giant patch, have also been employed to study SGLT1, but here the disadvantage is membrane instability and the difficulty of obtaining high electrical resistance contacts ($>10^9$ Ω) between the patch pipette and the oocyte plasma membrane (47).

The concurrent employment of an independent optical method to monitor voltage-induced conformational changes in SGLT1 overcomes some of the inherent limitations of charge measurements alone, since they are subjected to different constraints than charge measurements. Charge is extracted from SGLT1 pre-steady-state currents within a background of plasma membrane capacitive currents, SGLT1 ionic currents (uniporter currents), and membrane leakage currents, whereas SGLT1 optical records are measured against a stable background fluorescence.

The human isoform was used to study SGLT1 charge movement because the midpoint voltage of the distribution of the protein between the outside-facing and inside-facing conformations ($V_{0.5}$) was close to the normal holding potential, -50 mV. This means that over the practical range of voltages that can be used with oocytes, -150 to $+50$ mV, the full charge movement can be recorded, but this is not the case with other SGLTs with $V_{0.5}$ values of 0 to -10 mV, e.g., rabbit SGLT1 (59). This also is a problem at low Na^+ concentrations where $V_{0.5}$ moves towards more negative voltages (Fig. 23) and it becomes difficult to estimate values of Q_{\max} . Such limitations resulted in early confusion about the origin of charge movements where some concluded that they were wholly ion-well effects.

7. Submillisecond charge movements

In two-electrode voltage-clamp experiments, we observed a fast (submillisecond) rising phase of charge

movement when membrane potential was stepped from the holding to a large positive test voltage (e.g., from -50 to $+50$ mV), and simulations predicted a fast rising phase of charge movement with depolarizing voltage pulses (59, 167). To study this fast charge, the cut-open oocyte voltage-clamp technique (with a settling time of $80\ \mu s$) was combined with fluorescence measurements on the hSGLT1 mutant Q457C labeled by TMR6M (128). In 100 mM external Na^+ (Fig. 26A), depolarizing voltage steps evoked a charge movement that rose initially to a peak (with time constant 0.17 ms) before decaying to steady state (with time constants, $2\text{--}30\text{ ms}$ and $25\text{--}100\text{ ms}$) in the presence of Na^+ but not its absence. The time to peak (0.9 ms) decreased with $[\text{Na}^+]$ (Fig. 26B). In absence of Na^+ , charge movements decayed to steady state with three time constants (0.2 , 2 , and 150 ms). Charge movement was accompanied by fluorescence signals with similar time courses (Fig. 26, C and D), indicating that the conformational changes monitored by charge movement are reflected by local environment changes at or near Q457C.

In external Na^+ , a depolarizing voltage pulse is thought to result in Na^+ release from the Na^+ -bound transporter and a subsequent reorientation of the empty transporter from the outward-facing to the inward-facing

conformation. The development of the rising phase of charge movement in SGLT1 (and Shaker K^+ channels; Ref. 8) is due to a decrease in time constant with depolarization of the membrane and the contribution of charge from secondary steps. (Fig. 23F), i.e., the major voltage-dependent step of the $\text{Na}^+/\text{glucose}$ transport cycle is the return of the empty carrier from inward to outward facing conformations (128).

C. Conformational Dynamics

Simultaneous charge and fluorescence measurements can also be used to study the distribution of conformations of SGLT1 under sugar transporting conditions. In these experiments, we took advantage of the hSGLT1 mutant G507C. The TMR6M-labeled mutant transporter exhibited kinetics similar to that of wild-type hSGLT1, before and after labeling of Cys507 by TMR6M (130). Figure 27A shows a comparison of charge and fluorescence (ΔF) records in the absence and presence of saturating α MDG (100 mM). Addition of saturating sugar (100 mM α MDG) nearly eliminated the pre-steady-state current, but not the fluorescence signal (Fig. 27B). This indi-

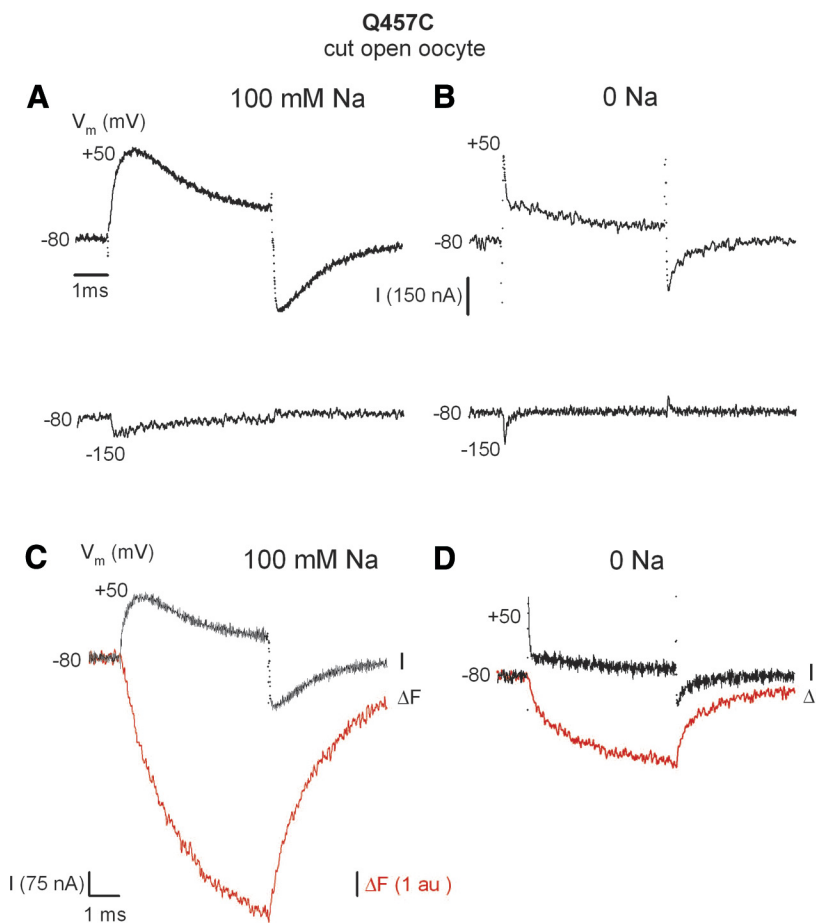


FIG. 26. Correlation between fast charge and fluorescence. The experiment was performed using the cut-open oocyte voltage clamp on TMR6M-labeled Q457C. The currents have been compensated for membrane capacitance and background current using the P/4 protocol with a subtracting holding potential of -150 mV (128). External and guard solution contained 100 mM Na-methanesulfonate and internal solution contained 100 mM K-methanesulfonate. V_h was -80 mV , and test voltages were $+50$ and -150 mV . A: pre-steady-state currents at 100 mM Na^+ . B: pre-steady-state currents at 0 Na^+ . C and D: comparison of the rising phase of the pre-steady-state current (I) and fluorescence (ΔF) in 100 mM $[\text{Na}^+]_o$ (C) and in absence of Na^+ (D).

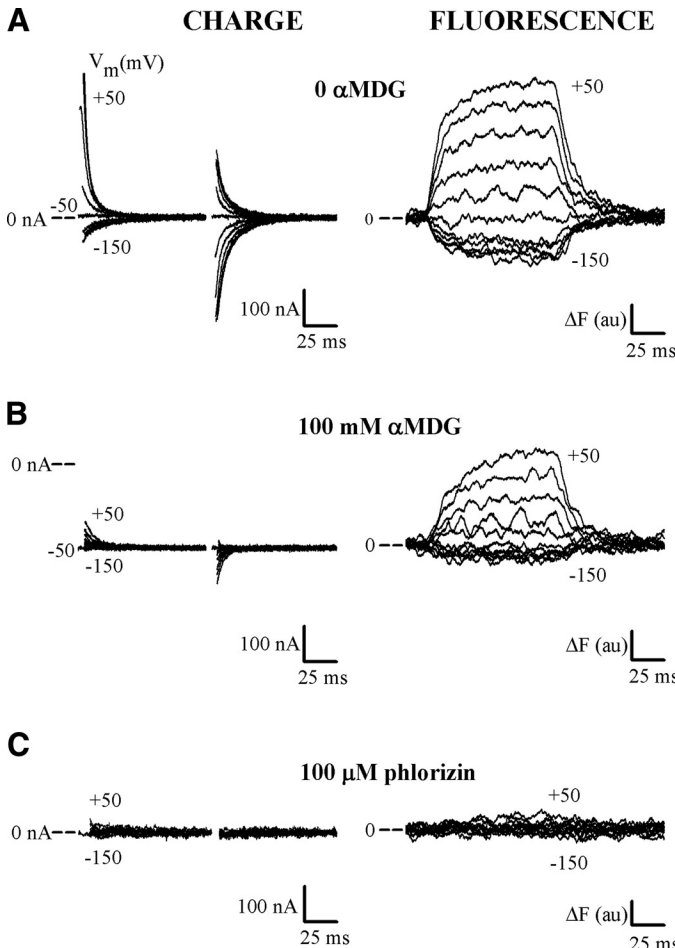


FIG. 27. Effect of sugar on charge and fluorescence. Comparison of charge and fluorescence (ΔF) records in the absence and presence of saturating α MDG (100 mM). V_h was -50 mV, and test voltage varied from $+50$ to -150 mV (20-mV decrements). Dashed lines are the zero current or zero ΔF levels. *A*: in NaCl buffer. *B*: in NaCl buffer with 100 mM α MDG. *C*: in the presence of saturating phlorizin.

cated the presence of an electroneutral conformational step. In contrast, phlorizin blocked the pre-steady-state current and the conformational changes (Fig. 27C).

D. Substrate and Drug Interactions

SGLT1, like many other cotransporters, has been found to transport a wide variety of substrate analogs at widely different turnover rates. In the glucose, nucleoside, and dipeptide cotransporters, drugs were transported at maximum rates ranging from 10 to 150% of that for the natural substrate (37, 136, 188).

For example, indican (indoxyl- β -D-glucopyranoside) was transported by hSGLT1 at 10% of the maximal rate of glucose but with a fourfold greater apparent affinity; $K_{0.5}$ for indican is 80 μ M versus 300 μ M for glucose (37, 125). The I - V curves for the indican and α MDG currents at saturating concentrations of the sugars are shown in Figure 28C. Sat-

urating indican only reduced the hSGLT pre-steady-state currents by 10% (Fig. 28, *A* and *B*), whereas α MDG eliminated them. This contrast in behavior of indican and α MDG indicated a difference in the rate-limiting step between the two substrates.

Computer modeling (see below) indicated that the rate-limiting step for indican transport is sugar translocation, whereas for α MDG, it is dissociation of Na^+ from the internal binding sites. Because of the differences in turnover rates and the rate-limiting step between indican and α MDG, indican behaved as a competitive inhibitor of α MDG transport (Fig. 28*D*). In this

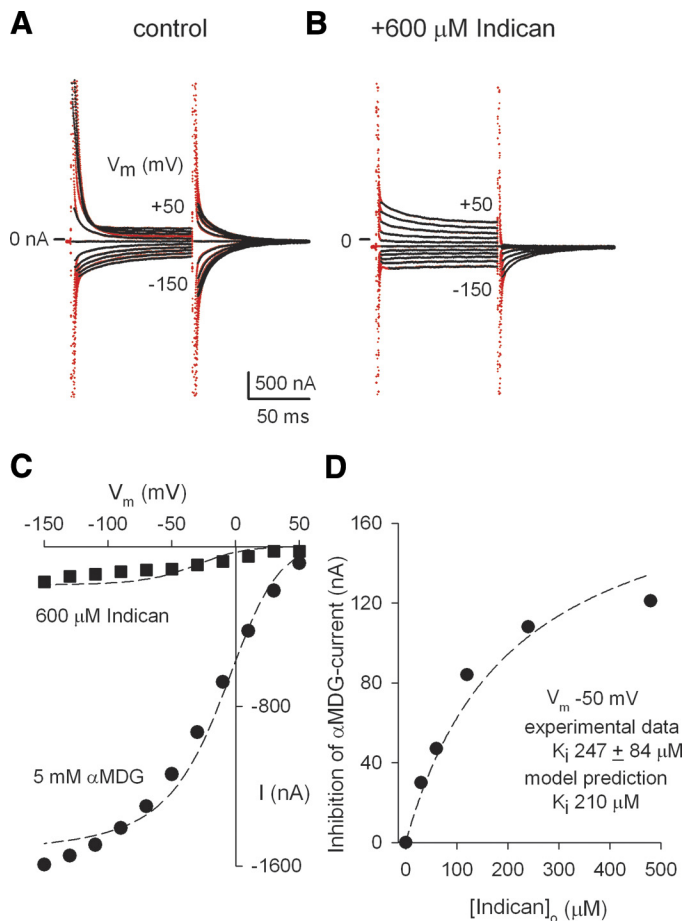


FIG. 28. Characteristics of indican currents from an oocyte expressing hSGLT1. Membrane potential was held at -50 mV (V_h), and test voltage pulses were applied (from $+50$ mV to -150 mV in 20-mV decrements). Red traces represent total current, and black traces are the records with the oocyte membrane capacitance subtracted. *A*: current records in NaCl buffer alone. *B*: in presence of 600 μ M indican. *C*: I - V curves of the indican- and α MDG-induced steady-state currents. *D*: inhibition of α MDG (0.25 mM) current by indican. Membrane potential was -50 mV. The dashed line was drawn with a K_i of 210 μ M, obtained by simulation of the 8-state kinetic model (see text). Kinetic parameters used were: $k_{12} = 45,000 \text{ M}^{-2}\text{s}^{-1}$, $k_{21} = 300 \text{ s}^{-1}$, $k_{1a} = 600 \text{ s}^{-1}$, $k_{a1} = 50 \text{ s}^{-1}$, $k_{ab} = 5 \text{ s}^{-1}$, $k_{ba} = 40 \text{ s}^{-1}$, $k_{b6} = 100 \text{ s}^{-1}$, $k_{6b} = 100 \text{ s}^{-1}$, $k_{25} = 0.01 \text{ s}^{-1}$, $k_{52} = 3.5 \times 10^{-4} \text{ s}^{-1}$, $k_{56} = 5 \text{ s}^{-1}$, $k_{65} = 2,250 \text{ M}^{-2}\text{s}^{-1}$, $k_{23} = 45,000 \text{ M}^{-1}\text{s}^{-1}$, $k_{32} = 20 \text{ s}^{-1}$, $k_{45} = 800 \text{ s}^{-1}$, $k_{54} = 81,667 \text{ M}^{-1}\text{s}^{-1}$, $k_{34} = 50 \text{ s}^{-1}$, $k_{42} = 50 \text{ s}^{-1}$, $k_{27} = 250,000 \text{ M}^{-1}\text{s}^{-1}$, $k_{72} = 12 \text{ s}^{-1}$, $k_{85} = 800 \text{ s}^{-1}$, $k_{58} = 756,173 \text{ M}^{-1}\text{s}^{-1}$, $k_{78} = 0.5 \text{ s}^{-1}$, $k_{87} = 0.5 \text{ s}^{-1}$. Total number of transporters $N_t = 1.5 \times 10^{12}$.

experiment, the α MDG current (generated by 0.25 mM α MDG) was inhibited by increasing concentrations of indican, K_i of 247 μM . Simulations indicate that if α MDG is present at the $K_{0.5}$ concentration, then the indican K_i was twice the $K_{0.5}$ for indican transport, i.e., there was classical competitive inhibition between indican and sugar. The competition between α MDG and indican is due to the “trapping” of the transporters in the indican-bound conformation (125).

In recent years, there has been increasing interest in using transporters as vehicles for drug delivery. Our findings using indican and glucose indicate that competition between substrates and drugs should be taken into consideration when targeting transporters as drug delivery systems.

XI. KINETIC MODELING

A. Model

Many of the experimental observations on the kinetics of SGLT1 are accounted for by the six-state ordered nonequilibrium kinetic model for Na^+ -dependent sugar transport originally proposed by Parent et al. (167). The model (Fig. 29) is based on the alternating access mechanism (see also Fig. 2 for an earlier 6-state equilibrium model). In a transport cycle, accessibility to the ligand (Na^+ and glucose) binding sites alternates between external and internal membrane surfaces. The transporter has six kinetic states, consisting of the empty transporter [C] (states 1 and 6), the Na^+ bound [CNa_2] (states 2 and 5), and the Na^+ - and sugar-bound transporter [CNa_2S] (states 3 and 4) at the external and internal membrane surfaces (Fig. 29). On the external membrane surface, two external Na^+ bind to the transporter before glucose, and glucose is released at the internal membrane surface before the Na^+ . The transition ($\text{C}2 \leftrightarrow \text{C}5$) is the Na^+ -uniport mode of the transporter.

The empty transporter is assumed to have a valence of -2 . Membrane voltage is assumed to affect Na^+ binding/dissociation with the transporter ($\text{C}1 \leftrightarrow \text{C}2$) and ($\text{C}5 \leftrightarrow \text{C}6$), and the conformational change of the empty transporter across the membrane ($\text{C}1 \leftrightarrow \text{C}6$). Since the Na^+ bound protein [CNa_2] is electroneutral, the sugar binding (rate constants $k_{23}, k_{32}, k_{45}, k_{54}$) and translocation steps (k_{34}, k_{43}) were assumed to be voltage independent.

B. Experimental Basis

The experimental basis for the kinetic model for Na^+ /glucose cotransport is described above, namely, biochemical evidence for alternating access, indirect and direct measurement of Na^+ :sugar stoichiometry, the ki-

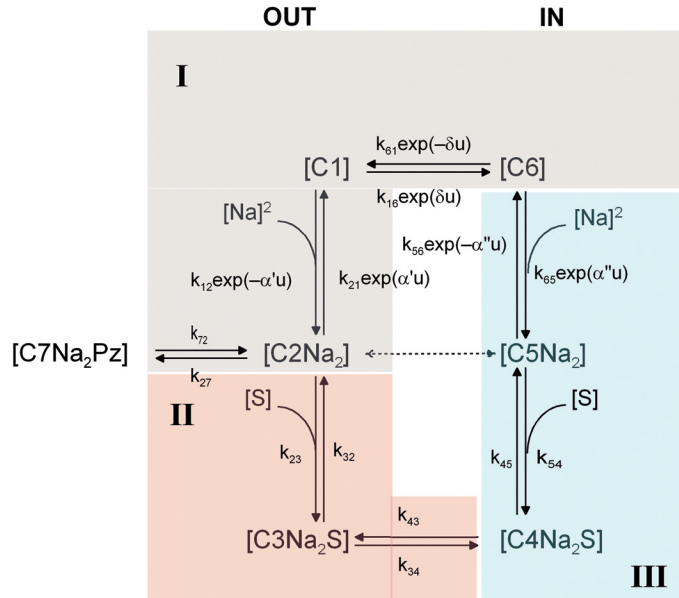


FIG. 29. Six-state ordered kinetic model for Na^+ -glucose cotransporter. Scheme showing the six kinetic states and the rate constants for the transitions between them. In the absence of ligands, the transporter exists in two states ($\text{C}1$ and $\text{C}6$). At the external surface, two Na^+ bind to the transporter to form the complex $\text{C}2\text{Na}_2$. The sugar-loaded transporter ($\text{C}3\text{Na}_2\text{S}$) undergoes a conformational change ($\text{C}3\text{Na}_2\text{S}$ to $\text{C}4\text{Na}_2\text{S}$) resulting in Na^+ -glucose cotransport. The reaction from state $\text{C}2\text{Na}_2$ to $\text{C}5\text{Na}_2$ (dashed line) is the uniport mode of Na^+ transport by SGLT1. Pre-steady-state currents are associated with the partial reactions $\text{C}2\text{Na}_2 \rightarrow \text{C}1 \rightarrow \text{C}6$. Region I (gray) is the pre-steady-state currents. II (red) includes external sugar binding/dissociation ($\text{C}2\text{Na}_2 \rightarrow \text{C}3\text{Na}_2\text{S}$) and sugar translocation across the cell membrane ($\text{C}3\text{Na}_2\text{S} \rightarrow \text{C}4\text{Na}_2\text{S}$); and III (blue) are the internal Na^+ release ($\text{C}5\text{Na}_2 \rightarrow \text{C}_6$) and sugar release ($\text{C}4\text{Na}_2\text{S} \rightarrow \text{C}5\text{Na}_2$) steps. The rate constants (k_{ij} from state i to state j) can be determined by isolating partial reactions in each region. Region I describe the pre-steady-state currents (128). Rate constants in region II can be estimated using indican transport (132). The rate constants for internal reactions (III) can be estimated from the study of reverse Na^+ -glucose cotransport (47). For the 6-state model, the rate constants (estimated using partial reactions I, II, and III described above) are as follows: $k_{12} = 140,000 \text{ M}^{-2}\text{s}^{-1}$, $k_{21} = 300 \text{ s}^{-1}$, $k_{16} = 600 \text{ s}^{-1}$, $k_{61} = 25 \text{ s}^{-1}$, $k_{23} = 45,000 \text{ M}^{-1}\text{s}^{-1}$, $k_{32} = 20 \text{ s}^{-1}$, $k_{34} = 50 \text{ s}^{-1}$, $k_{43} = 50 \text{ s}^{-1}$, $k_{45} = 800 \text{ s}^{-1}$, $k_{54} = 190,000 \text{ M}^{-1}\text{s}^{-1}$, $k_{56} = 5 \text{ s}^{-1}$, $k_{65} = 2,250 \text{ M}^{-2}\text{s}^{-1}$, $k_{25} = 0.01 \text{ s}^{-1}$, $k_{52} = 0.0005 \text{ s}^{-1}$, $k_{27} = 50,000 \text{ M}^{-2}\text{s}^{-1}$, $k_{72} = 0.01 \text{ s}^{-1}$, $\delta = 0.7$, $\alpha' = 0.3$, $\alpha'' = 0$. [Modified from Parent et al. (167).]

netics of forward and reverse Na^+ /glucose transport, substrate binding order, voltage dependence of external Na^+ binding/dissociation and reorientation of the empty transporter, the number of transporters in the plasma membrane, and the cooperativity between the two Na^+ binding sites (47, 67, 68, 127–130, 139, 146, 166, 262). The goal of a kinetic model is to summarize the experimental data in a coherent conceptual framework and to use the model to make predictions for designing experiments to challenge the model.

The binding of two Na^+ to the transporter was modeled to occur in one step (167). This simplification was justified at high Na^+ concentrations due to the strong positive cooperativity between the two Na^+ sites (49). Na^+ binding to SGLT1 exhibits high cooperativity (146). The

one-step approximation is an oversimplification, and it fails to account for the experimental data as external $[Na^+]$ is reduced towards zero (see below). However, key properties of the kinetics of SGLT1 can be easier to see with such a simple model.

C. Voltage Sensitivity

The effect of membrane voltage V_m on the rate constants was assumed to follow Eyring rate theory (with symmetric potential energy profile between the forward and backward reactions, Ref. 167). Dielectric parameters α and δ are used to represent the fraction of the membrane electric field felt by Na^+ binding and the translocation of the empty transporter (110), respectively. The rate constants for a transporter with a valence (z_T) of -2 are $k_{16} = k_{16}^0 \exp(\delta FV_m/RT)$, where F is the Faraday constant, R is gas constant, and T is temperature. For external Na^+ binding, $k_{12} = k_{12}^0 [Na]_o^2 \exp(-\alpha' FV_m/RT)$ and $k_{21} = k_{21}^0 \exp(\alpha' FV_m/RT)$; and internal Na^+ binding: $k_{65} = k_{65}^0 [Na]_i^2 \exp(\alpha' FV_m/RT)$ and $k_{56} = k_{56}^0 \exp(-\alpha'' FV_m/RT)$. The pre-steady-state currents (hSGLT1 capacitive currents) were assumed to be associated with the reorientation of the empty transporter between outward- and inward-facing conformations ($C_1 \leftrightarrow C_6$) and external ($C_2 \leftrightarrow C_1$) and internal Na^+ binding/dissociation ($C_5 \leftrightarrow C_6$).

The changes of fluorescence intensity associated with SGLT1 with step jumps in membrane voltage were assumed to arise from changes in occupancy probabilities: $\Delta F \approx qy_1\Delta C_1 + qy_2\Delta C_2 + qy_3\Delta C_3 + qy_4\Delta C_4 + qy_5\Delta C_5 + qy_6\Delta C_6$, where qy_j is the apparent quantum yield of the fluorophore (TMR6M) when SGLT1 is in conformation C_j (128).

D. Estimating Parameters

The Na^+ /glucose cotransport model involves a closed cycle of six partial reactions, each of the phenomenological kinetic parameters $K_{0.5}^{Na}$, $K_{0.5}^{sug}$, I_{max}^{Na} , and I_{max}^{sug} depend on all the rate constants of the transport cycle (see for example, *Eqs. A37–A43* in Ref. 167). For the six-state model, there are 14 rate constants, and it is a challenge to estimate all the values. For their determination, we note that the partial reactions fall into three groups: 1) voltage-dependent reactions [these are the conformational changes of the empty transporter between external and internal membrane surfaces ($C_1 \leftrightarrow C_6$) and external Na^+ binding/dissociation ($C_1 \leftrightarrow C_2$)]; 2) external sugar binding/dissociation ($C_2 \leftrightarrow C_3$) and sugar translocation ($C_3 \leftrightarrow C_4$); and 3) internal Na^+ release ($C_5 \leftrightarrow C_6$) and sugar release ($C_4 \leftrightarrow C_5$). Moreover, in two-electrode voltage-clamp experiments where the inward transport of Na^+ and glucose are studied, the rate constants for sugar

translocation across the membrane ($C_3 \leftrightarrow C_4$) and the internal ligand binding steps ($C_4 \leftrightarrow C_5$; $C_5 \leftrightarrow C_6$) cannot be uniquely determined.

A set of rate constants for the six-state model for hSGLT1 obtained from experiments where individual partial reactions were isolated is presented in Figure 29: 1) the kinetic parameters for voltage-dependent reactions were obtained from fitting the pre-steady-state currents in the absence of sugar; and 2) kinetic parameters for Na^+ and glucose binding on the internal membrane surface were obtained from studies on reverse sugar transport using the excised giant patch (47). The rate constants for sugar binding and translocation were estimated from forward Na^+ /glucose cotransport (68). These rate constants were obtained from simulation of the global steady-state and pre-steady-state SGLT1 kinetics, and not simply the simulation of a single type of experiment.

There are several notable implications of the model: 1) the voltage-dependent steps are the reorientation of the empty carrier and external Na^+ binding/dissociation. The internal Na^+ binding steps do not depend on voltage. Thus there is an asymmetry in the voltage dependence of Na^+ binding between the outside and inside; 2) the rate-limiting step of Na^+ /glucose transport is the release of Na^+ on the internal membrane surface; 3) under steady-state conditions, the current generated by Na^+ /glucose cotransport arises from the “conformational” current of the empty carrier as it returns from the internal to the external membrane surface ($C_1 \leftrightarrow C_6$) and external Na^+ binding/dissociation ($C_1 \leftrightarrow C_2$); and 4) the model accounts for the outward current, but this requires that the rates of translocation of the empty transporter, k_{16} and k_{61} , are sodium dependent as predicted (49). The asymmetry in the *I*-*V* curves between inward and outward currents are in agreement with our model where the binding of Na^+ at the internal surface is voltage independent. However, this is inconsistent with the location of the Na^+ binding site in the sugar occluded vSGLT crystal structure (48).

E. Testing

Most of the tests of the six-state model have been based on extending the type of experiment and the time scale of the pre-steady-state currents, for example, examining the kinetics of different substrates (glucose and indican) and reverse transport. The time scale of the pre-steady-state kinetics was extended by 1) using a faster voltage clamp, such as the cut-open oocyte voltage-clamp method which has a 10-fold faster settling time (80 μ s compared with 1 ms) compared with the two-electrode voltage clamp (18, 128); and 2) application of test voltage pulses of duration longer than the 100 ms standard pulses

(100, 128). In the simplified three-state model for pre-steady-state currents ($C_2 \leftrightarrow C_1 \leftrightarrow C_6$), the binding of the two external Na^+ is lumped into a single step. This is essentially an equilibrium assumption at high Na^+ concentrations, i.e., at $[\text{Na}^+]_o \gg K_D^{\text{Na}}$ (K_D^{Na} is the intrinsic dissociation constant for Na^+ binding to the protein). One would expect model predictions to deviate from experimental data at low Na^+ concentrations and during relaxations to steady state in response to step perturbations in membrane voltage or ligand concentrations. Simulations of the three-state model (59, 128) predict the following: 1) the pre-steady-state current relaxation contains two time constants, a fast submillisecond component associated with Na^+ binding/dissociation and a medium component 2–30 ms associated with the empty transporter; 2) the dependence of the medium time constant (τ_{ON}) on membrane voltage is Gaussian or bell shaped with a peak at the $V_{0.5}$, and τ_{ON} is decreased with hyperpolarizing and depolarizing voltages away from the $V_{0.5}$; 3) the shift of the $V_{0.5}$ of the charge movement is –60 mV/10-fold decrease in $[\text{Na}^+]_o$; and 4) since the empty transporter has a valence of –2, $z\delta$ (in the Boltzmann relation) should be 2.

While the steady-state kinetics are well described by the six-state model, there are several predictions that have not been met regarding the presteady state currents.

1) Charge and fluorescence measurements have revealed that the pre-steady-state current contains multiple time constants with time scales ranging from 0.1 to 100 ms (128). In 100 mM external $[\text{Na}^+]$, depolarizing voltage pulses evoked a charge movement that rose initially to a peak (with time constant $\tau = 0.17$ ms) before decaying to steady state with two time constants ($\tau = 2$ –30 and 25–150 ms). In the absence of Na^+ , charge movement decayed to steady state with three time constants (0.2, 2, and 150 ms), indicating that reorientation of the empty transporter between the outward (C_1) and inward (C_6) facing conformations involves at least two additional intermediate states ($C_1 \leftrightarrow C_a \leftrightarrow C_b \leftrightarrow C_6$).

2) There is an asymmetry in the voltage dependence of the time constants. The medium (τ_{med} 2–30 ms) time constant was independent of voltage for hyperpolarizing pulses, whereas τ_{med} decreased with depolarizing voltage pulses (18, 128). The asymmetry in voltage sensitivity has also been observed in ion channels and has been attributed to an asymmetry in the potential energy profile (261).

3) The shift of the midpoint voltage ($V_{0.5}$) with decreasing $[\text{Na}^+]_o$ is –100 mV/10-fold decrease in $[\text{Na}^+]_o$ (Fig. 23E). This is also the case for the shift of the $V_{0.5}$ for fluorescence with $[\text{Na}^+]_o$ (Fig. 25E; Ref. 146). The failure of the three-state model to account for the shift of the $V_{0.5}$ with decreasing $[\text{Na}^+]_o$ is not surprising, because lumping the two Na^+ binding steps into one step means that the rate constants k_{16} for empty transporter reorientation

($C_1 \leftrightarrow C_6$) and k_{12} for Na^+ binding ($C_1 \leftrightarrow C_2$) become pseudo rate constants and are dependent on $[\text{Na}^+]_o$ (49). Computer simulations of different models for Na^+ binding to cotransporters showed that two-step sequential models for Na^+ binding are required to account for a shift of 100 mV/10-fold change in $[\text{Na}^+]$ (Dr. Ian Forster, University of Zurich, personal communication).

4) $z\delta$ determined experimentally is 1, whereas simulations predict a $z\delta$ of 2. This discrepancy could, in part, be due to our inability to measure very rapid (submillisecond) components of charge movement.

To account for three relaxation time constants in the absence of Na^+ and the asymmetry in voltage dependence, two additional states C_a and C_b between C_1 and C_6 ($C_1 \leftrightarrow C_a \leftrightarrow C_b \leftrightarrow C_6$) are required (region I of Fig. 29; Ref. 128), together with asymmetry in the voltage dependence of the rate constants. Simulations showed the steady-state kinetics of Na^+ /glucose cotransport was equally accounted for by both the six- and eight-state models. The models qualitatively and quantitatively accounts for I - V relations for forward and reverse transport, as well as the dependence of the kinetic parameters $K_{0.5}^{\text{Na}}$, $K_{0.5}^{\alpha\text{MDG}}$, $I_{\text{max}}^{\text{Na}}$, and $I_{\text{max}}^{\alpha\text{MDG}}$ on membrane voltage and ligand concentrations (130). The models also account for indican transport (a high-affinity, low-turnover substrate) and the competition between αMDG and indican (Fig. 28D).

F. Distribution of Conformations

Insight into the transport kinetics may be obtained by an analysis of the occupancy probability (P_o) of each state in the eight-state model, and how those states are altered by ligands and voltage. In external NaCl buffer (Fig. 30), the transporter is predominantly in $C_2\text{Na}_2$ at negative membrane voltages (98% occupancy in $C_2\text{Na}_2$ at –150 mV), and in C_6 at depolarizing voltages (73% at +50 mV). With step jumps in membrane voltage, the pre-steady-state current is associated with redistribution of the negatively charged transporter between the outward-facing and inward-facing conformations ($C_2\text{Na}_2$ and C_6).

External sugar alters the distribution by reducing the occupancy in $C_2\text{Na}_2$ and increasing C_5 occupancy at large negative membrane voltages. At large positive voltages (e.g., +50 mV), the inward-facing ligand-free conformation C_6 is predominant, regardless of the sugar concentration (Fig. 30, A, B, and D). At saturating external $[\alpha\text{MDG}]$, when membrane voltage is stepped from –50 to +50 mV, the charge movement is too small to be detected because of the low occupancy in states $C_2\text{Na}_2$, C_1 , C_a , C_b , and C_6 (Fig. 30D). However, there is a conformational change from $C_5\text{Na}_2 \leftrightarrow C_6$, and is monitored by the fluorescence changes in the TMR6M labeled G507C (Fig. 27B). The fluorescence change is due to differences in apparent quantum yields of the fluorophore between the

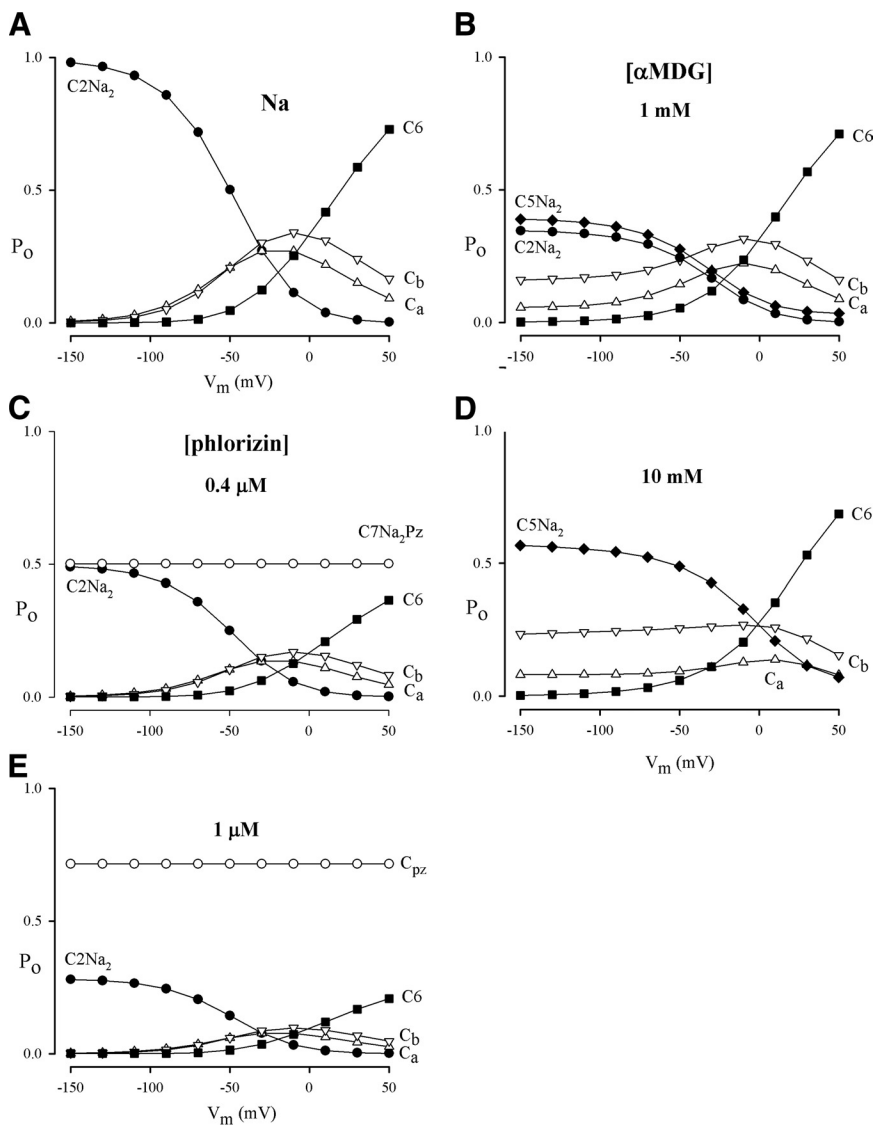


FIG. 30. Simulation of occupancy probabilities (P_o) of the 8-state model. For comparison of charge and fluorescence measurements, the simulations were performed for the TMR6M-labeled hSGLT1 mutant G507C, which exhibited similar steady-state and pre-steady-state kinetics as wild-type hSGLT1. For clarity, states with $P_o < 0.1$ were not plotted. These states were as follows: C_1 in *A*, *C*, and *E*; C_1 , $C_2\text{Na}_2$, $C_3\text{Na}_2\text{S}$, and $C_4\text{Na}_2\text{S}$ in *B* and *D*. *A*: in NaCl buffer in the absence of sugar. *B* and *D*: in 1 mM and saturating (10 mM) αMDG . *C* and *E*: in 0.4 and 1 μM phlorizin. [From Loo et al. (125).]

two states, $C_5\text{Na}_2$ and C_6 . We predict that this conformational change is a rate-limiting step for Na^+ /sugar cotransport.

Phlorizin locked the transporters in a fixed state ($C_7\text{Na}_2\text{Pz}$) and prevented the protein from running through the transport cycle. The increase in the occupancy of the phlorizin-bound state ($C_7\text{Na}_2\text{Pz}$) is balanced by reduction of the occupancy probabilities in all other conformations (Fig. 30, *A*, *C*, and *E*). The profile of the P_o - V_m curves is not affected by phlorizin. At the K_i for phlorizin, 50% of the transporters are in the phlorizin-bound conformation. The effect of phlorizin on the pre-steady-state current is consistent with the model simulations: there is no effect of phlorizin on midpoint voltage ($V_{0.5}$), and maximal charge (Q_{\max}) is reduced 50% at the K_i for phlorizin.

The predicted occupancy in the different conformations with changes in Na^+ and sugar concentrations and

membrane voltage (Fig. 30) was supported by the close agreement between experimental data on fluorescence and the simulations (125, 128, 130, 135).

Simulations using the eight-state model show that, qualitatively and quantitatively, it accounts for the steady-state kinetics of Na^+ /glucose cotransport. However, it fails to fit the pre-steady-state kinetics below 1 ms due to assumptions about the kinetics of sodium binding (125, 135), e.g., 1) the initial rise component of the charge movement with depolarizing voltage pulses (Fig. 26) (128) and 2) magnitude of the shift of $V_{0.5}$ (~ 100 mV/10-fold change in $[\text{Na}]_o$) for charge and fluorescence. These are related: the rising phase is associated with the Na^+ binding steps (128), and a sequential binding model with 2 Na^+ binding sites ($\text{CN}_2 \leftrightarrow \text{CN}_1 \leftrightarrow \text{C}_1$) is required to account for the 100 mV (per 10-fold change in $[\text{Na}]_o$) shift in $V_{0.5}$. At present, very little is known about the kinetics of the

two Na^+ binding steps. A future challenge is to gain insights into the binding of the Na^+ .

XII. STRUCTURE AND FUNCTION

The ultimate goal is to understand, on the atomic level, how an ion-driven cotransporter protein transforms the energy of the electrochemical gradient into work, enabling it to drive the cosubstrate against its concentration gradient. The kinetics studies have identified eight different protein conformations, the rates of transitions between them, and the dynamics of the conformational changes in a Na^+/sugar transport cycle (Fig. 31). With the solution of two conformations of the SGLT1 bacterial homolog vSGLT, providing for the first time a structural model for SGLT1, the task ahead is to merge the kinetics and structure into a dynamic structural translation. Even though we do not yet have the structure of hSGLT1, the ideal situation, there are tools available to begin the process.

At the time of this writing there are four different Na^+ cotransporter crystal structures in different conformations. These cotransporters, LeuT, vSGLT, BetP, and Mhp1, belong to different gene families but share a common core architecture of 10 helices in an inverted repeat configuration. We believe that this shared structural fold implies a common kinetic mechanism; therefore, in the following discussion we will use the LeuT helix numbering system. [For example, vSGLT TM1 is renamed TM-1 because vSGLT TM2 corresponds to TM1 of the core

structure (see Fig. 12), and so on.] The structure of the nucleobase cotransporter Mhp1 has been solved in the outward open (C2), outward occluded (C3), and inward facing (C5) conformations (199). The leucine cotransporter LeuT is an outward occluded (C3) conformation (256), BetP appears to be in an intermediate conformation between C3 and C4 (183), and vSGLT1 is in an inward occluded and inward open conformations (C4, C5) (48, 238). As yet, there are no structures of these proteins in the C1 or C6 conformations.

Our first strategy was to “thread” the vSGLT1 sequence onto the LeuT coordinates to model the outward occluded (C3) conformation (48). Comparison of the vSGLT C4 configuration and the C3 model were then compared to identify how the helices of the core have to move in the C3 to C4 transition (alternating access).

There is an external aqueous pathway where extracellular sugar and Na^+ gain access to the binding sites (bounded by TM1E, TM2, TM6E and TM10), and the aqueous pathway leading from the binding sites to the cytoplasm (bounded by TM1I, TM2, TM3, TM6I, TM8, and TM10). The major arrangements that are predicted to occur during the transition from the outward (C3) to inward (C4) facing conformations involve TM1, TM6, and TM10. The external end of TM10 folds over the sugar binding site and F423 forms part of the external gate along with Y87 (TM2) and M73 (TM1) (see Fig. 14C). The tilting of TM10 is facilitated by P436 and G437 in the middle of the transmembrane domain. Changes in the position of TM2, TM3, TM6I, TM8, and

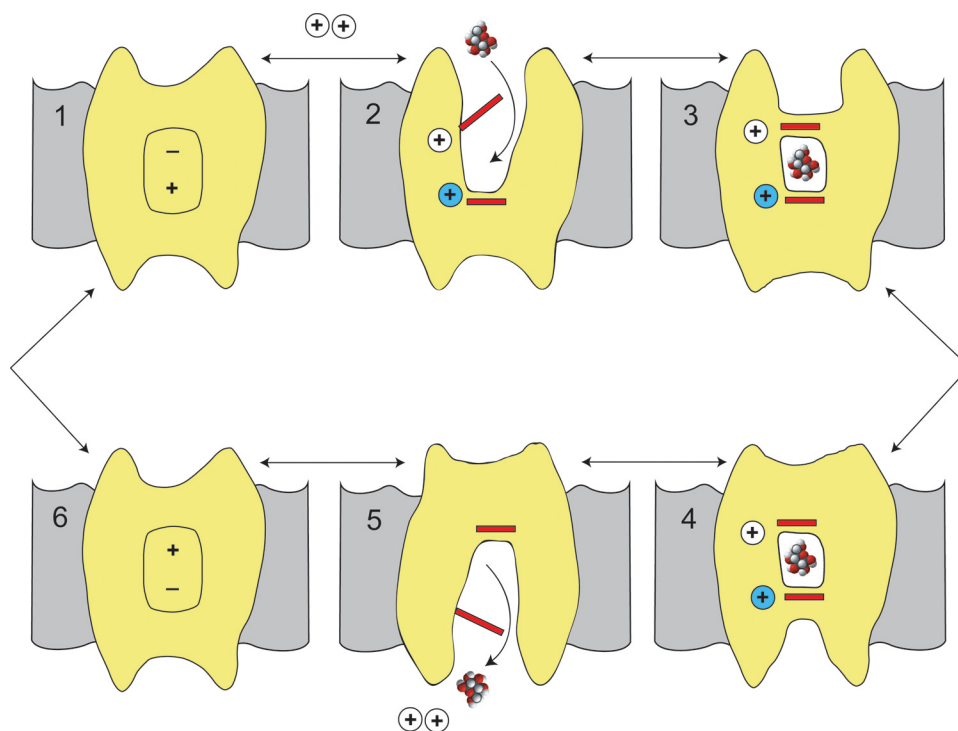


FIG. 31. A 6-state model of SGLTs to integrate the kinetic and structural data. Na^+ binds first to the outside to open the outside gate (C2) permitting outside sugar to bind and be trapped in the binding site (C3). This is followed by a conformational change from an outward occluded (C3) to an inward occluded (C4) state. Upon opening the inward gate (C5), the Na^+ and sugar are released into the cell interior. There is a paucity of experiments addressing the order of the ligand dissociation at the cytosolic surface. The transport cycle is completed by the change in conformation from the inward facing ligand-free (C6) to the outward facing ligand free (C1) states. Structures corresponding to C2 and C3 have been obtained for Mhp1, C3 for LeuT, and C4 for vSGLT.

TM10 also result in the expansion of the intracellular cavity. All that is then required to release sugar into the expanded cavity is the displacement of the inner gate Y263 (238).

Another view of the conformational changes that follow external sugar binding was obtained by homology modeling of hSGLT1 based on the structures of the Mhp1 obtained in the presence and absence of substrate (241). Figure 32 shows an outside view of hSGLT1 before and after sugar binding. In the outward facing open conformation (C2), the hydrophobic gating residues L87, F101, and F453 are open (12–20 Å apart), but these gates close after glucose binding (<6 Å apart) to trap the sugar. This occurs through a tilting of the external end of TM10 into the vestibule, facilitated by the double prolines in the middle of the helix (P465 and P466). This proline duplex is well conserved in the SLC5 family (Table 1) and Mhp1 (GP), but not in the LeuT family. In addition, the external ends of TM1 and TM2 tilt inward to bring the sugar coordinating residues into range. The unwound region in TM1 could facilitate the inward motion in all four families of Na^+ coupled transporters.

The predicted sugar-induced changes in tilt of the external end of TM10 is supported by cysteine scanning studies on vSGLT and hSGLT1 (67, 230). Specifically, sodium-dependent glucose binding induced changes in the fluorescence of probes covalently linked to cysteines at the external end of TM10 (A423C in vSGLT, and Q457C and D454C in hSGLT1). In addition, access of other mutants on the outer half of TM10, T460C and A468C, to MTS

reagents was also conformationally dependent (36, 67). Cysteine mutants lying outside the external vestibule also exhibit conformational changes, either access to MTS reagents (A439C, I443C, and Q445C at the top of TM9 and the linking loop to TM10, R499C at top of TM11, and L527C and Y528C at the top of TM12) (67). This indicates that there are sugar-induced structural changes throughout the protein.

Open structural questions still to be resolved include the following: 1) the identity of the second sodium binding site in hSGLT and determining whether it is a neutral (Na_2) or charged (Na^+) site (152); 2) the location of the inhibitor (phlorizin) binding site in hSGLT1 and hSGLT2. Phlorizin-like inhibitors are in development for treatment of diabetes (see Fig. 19). Phlorizin is a poor inhibitor of vSGLT ($K_i \sim 1 \text{ mM}$), but a potent inhibitor of human SGLTs ($K_i < 200 \text{ nM}$). 3) The structure of SGLTs in additional conformations, C1/C6, C2, and/or C4/C5, need to be determined.

XIII. MULTIFUNCTIONAL PROTEINS

SGLT1 does many things: it cotransports Na^+ and glucose, bringing an important nutrient into cells, but in doing so it depolarizes the plasma membrane, which can serve as a signal; in the absence of glucose, SGLT1 can still support a Na^+ current; the protein contains a water and urea channel; and it transports water and urea along with Na^+ and glucose (249). It is highly likely that these varied properties of SGLT1, and other cotransporters, have yet undiscovered physiological significance. It is a major challenge to identify the physiological functions of cloned proteins such as those in the human SGLT gene family. Even when genes have been cloned by expression cloning, e.g., SGLT1, it remains a nontrivial task to establish their physiological role in humans. Furthermore, there may be significant species differences, e.g., pig SGLT3 behaves as a $\text{Na}^+/\text{glucose}$ cotransporter in the *Xenopus laevis* oocyte expression system while human SGLT3 does not (34, 35, 138). It appears that in humans, SGLT3 is a glucose sensor expressed in the enteric nervous system and muscle. The first step in revealing the diverse functions of these proteins is to determine the properties of the cloned transporters in heterologous expression systems and to cast the net wide in terms of functional assays. A second step is to carefully phenotype patients with severe mutations in SGLT genes.

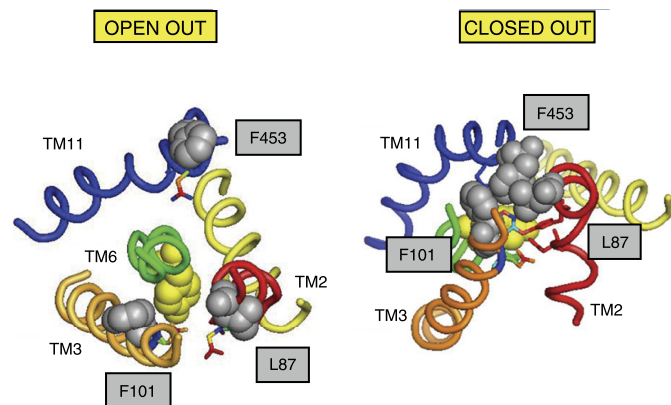


FIG. 32. Model of the hSGLT1 structural changes at the sugar site after glucose binding, and occlusion viewed from the external side of the membrane. The open out, sugar-free structure is based on Mhp1, and the closed out, sugar-occluded structure is based on vSGLT. Shown are TMs 1, 2, 6, and 10 along with the outer and inner gate residues [outer L87, F101, and F453 (grey spheres), inner Y290 (yellow sphere), and sugar coordinating (sticks)]. In the C2 conformation, the gates are open (10–20 Å apart) to expose the sugar binding residues. Upon sugar binding, the external gates close (4–6 Å apart) largely through an inward tilt of the external ends of TM10, TM1, and TM2. (From V. Chaptal, B. A. Hirayama, D. D. F. Loo, J. Abramson, and E. M. Wright, unpublished data.)

A. Na^+ Uniport

The first indication that SGLT behaved as a uniporter was the observation that phlorizin inhibited a current in the absence of glucose (see Fig. 4A) (226). This SGLT “leak” current was ~8% of the total $\text{Na}^+/\text{glucose}$ cotrans-

porter current and was not observed in control cells. Further experiments (131, 162) demonstrated that this current saturated with increasing external Na^+ concentration with a $K_{0.5}$ of 2.5 mM and a Hill coefficient of 2, and that both Li^+ and H^+ were able to substitute for Na^+ . The activation energy for the Na^+ leak current was similar to that for $\text{Na}^+/\text{glucose}$ cotransport, 21 versus 25 kcal/mol. It was concluded that the leak currents reflect Na^+ uniport through SGLT1.

B. Water and Urea Channels

SGLT1 provides a passive permeability pathway for water and other small molecules. Expressing SGLT1 in *Xenopus laevis* oocytes increased the osmotic water permeability of the cell (262). Expressed in terms of the number of SGLT1 proteins in the membrane, the osmotic water permeability is similar to that for the water channel AQP0, but only 5% of that for AQP1. The SGLT1 passive water permeability was independent of the direction and magnitude of the osmotic gradient, the presence or absence of ligands (Na^+ and sugar), but in Na^+ it was blocked by phlorizin with a K_i of $\sim 5 \mu\text{M}$ (124, 131, 134, 145, 262). Unlike the Na^+ uniport mode, the activation energy for water permeability is low (5 vs. 21 kcal/mol) and similar to that for water channels. It is concluded that SGLT1 behaves as a water channel, but unlike other water channels, permeation is dependent on the protein conformation, i.e., channel activity is blocked by phlorizin.

Urea uptake into SGLT1 expressing oocytes was also fourfold higher than in control oocytes (115, 165). The SGLT1-specific urea transport was blocked by phlorizin ($K_i 1 \mu\text{M}$), but only in Na^+ buffer as phlorizin only binds to SGLT1 in Na^+ . Phloretin also inhibits urea and water transport through SGLT1, but the K_i was 100–1,000 higher than that for phlorizin. As with SGLT1 water permeability, the urea uptake was not affected by the presence or absence of Na^+ , and the activation energy was 6 kcal/mol. The activation energy for both water and urea transport in control oocytes was 15 kcal/mol. There was no saturation of SGLT1 urea transport as uptake was not blocked by 100 mM concentrations of urea analogs, thiourea, 1,3-dimethyl urea, 1,1-dimethyl urea, or acetamide. It was concluded that SGLT1 behaves as a urea channel. Examination of the crystal structure of vSGLT and other members of the LeuT structural family does not reveal an obvious continuous pathway for water and urea across the protein, but the extracellular and intracellular aqueous vestibules suggest that pathway is through the sugar binding site. This is strengthened by molecular dynamic studies of vSGLT, showing that passive water fluxes cross the protein through the sugar transport pathway (20).

While the unitary conductance of SGLT1 for water and urea is low relative to other channels, SGLT1 may

play an important physiological role in water and urea transport in those cells with high levels of expression, e.g., 250,000 SGLT1 molecules/enterocyte. Thus SGLT1 may be a major pathway for water and urea transport across the intestinal brush-border membrane.

C. Coupled Water, Urea, and Glucose Transport

A surprising observation was that in oocytes expressing SGLT1, the addition of glucose immediately increased the transport of water into the cell (133, 134, 145, 263). The initial rate of sugar-coupled water transport was 1) directly proportional to the rate of $\text{Na}^+/\text{glucose}$ cotransport, i.e., the rate varied with changes in membrane potential, sugar concentration, and temperature (the activation energy for coupled water transport was identical to that for Na^+/sugar transport, 25–30 kcal/mol); 2) independent of the osmotic gradient and even occurred against an osmotic gradient; 3) coupling was independent of the ion used to drive sugar transport, Na^+ or H^+ ; and 4) the coupling coefficient varied by cotransporter subtype, e.g., rabbit SGLT1, human SGLT1, NIS, and a plant $\text{H}^+/\text{amino acid}$ cotransporter (AAP5) where the coupling ranged from 50 to 425 water molecules per turnover. This implied that water coupling was related to transporter architecture and not simply the rate of Na^+ and solute transport. While these experiments clearly demonstrated that there is a close relationship between $\text{Na}^+/\text{glucose}$ cotransport and the initial rate of water transport, controversy remains as to the interpretation of the results. We have favored the water cotransport hypothesis, while others favor a strict osmotic coupling, i.e., water flowed in response to the osmotic gradients set up by Na^+/sugar cotransport into the cell (15, 109, 133, 263–265). While there is no doubt that osmotic gradients do contribute to coupled water flow through SGLT1, the debate centers on the importance of unstirred layers during the initial (1–5 s) turning on of $\text{Na}^+/\text{glucose}$ cotransport. Potential unstirred layer effects are not likely to account for the observed coupling between urea and $\text{Na}^+/\text{glucose}$ cotransport (115). In molecular dynamic studies of vSGLT, 70–80 water molecules accompany galactose as it moves from the binding site into the intracellular space (20), consistent with the water pump hypothesis. Nevertheless, it is clear that there is coupling, direct or indirect, between water and $\text{Na}^+/\text{glucose}$ cotransport, and this is expected to play a major role in water transport across the intestinal brush border (133).

D. Glucose Sensor

Until 2003, it was widely assumed that all SGLT genes are expressed in intestinal and renal epithelial cells, where they are responsible for the accumulation of glu-

cose and galactose. However, hSGLT3 has proven not to be a Na^+ /glucose cotransporter, but instead a glucose sensor (35). The gene was initially found to be expressed in the human small intestine and muscle, and subsequent mRNA protection assays found that it was also expressed in uterus, lung, brain, spleen, thyroid, kidney, and trachea (Table 1). In the small intestine, immunocytochemical studies demonstrated that the hSGLT3 protein was present in the enteric neurons and not in intestinal epithelial cells. In skeletal muscle, the protein was confined to the neuromuscular junction. When expressed in *Xenopus laevis* oocytes, hSGLT3 was efficiently inserted into the plasma membrane, but it was unable to transport glucose.

Electrophysiological assays revealed that glucose caused a specific, phlorizin-sensitive, Na^+ -dependent depolarization of the membrane potential of up to 12 mV. Radioactive glucose uptake assays under voltage clamp revealed that the glucose-induced inward currents were not accompanied by glucose transport. The D-glucose affinity for hSGLT3 was low (K_m 20 mM), and D-galactose was not recognized. On the other hand, imino sugars, such as 1-deoxynojirimycin, were found to be highly potent agonists (K_m 4 μM ; Ref. 235). Based on these electrophysiological properties and the expression pattern of the gene, we have speculated that hSGLT3 is a glucose sensor and not a Na^+ /glucose cotransporter. This has been supported by studies that show glucose regulates intestinal motility in rodents and humans (103, 181) and that guinea pig enteric neurons are reported to be glucose sensitive (121).

Further strong evidence in support of SGLT3's function as a glucosensor came from a recent study where the gene was expressed in *C. elegans* ASK chemosensory neurons (9). On the basis of assays on chemotaxis plates, the transgenic animals were repulsed or attracted to 10 mM glucose depending on the pH, and the responses were blocked by 100 μM phlorizin. Wild-type worms were neither attracted nor repulsed by glucose.

E. Glucose Sensing in the Gut

Glucose sensors are present throughout the body, especially in the gastrointestinal tract. These range from the "sweet" receptors in the tongue to the glucose sensors in pancreatic beta cells and in the small intestine. These sensors are intimately involved in food intake, from coordinating the physiological response to an ingested carbohydrate meal, to regulating blood glucose levels, and regulating glucose transporter expression in response to changes in diet. It has long been recognized that one of the principal roles of the duodenum is to act as a sensory organ (see Ref. 180). Specifically, glucose in the duodenum inhibits gastric emptying, increases intestinal motility, and stimulates the release of glucose-dependent insulinotropic polypeptide (GIP), glucagon-like peptide-1 (GLP-1), and serotonin (5-HT)

from endocrine cells. The major function of GIP and GLP-1 is to stimulate pancreatic insulin secretion, whereas 5-HT acts to modulate enteric reflexes.

The glucose sensors lining the intestine have properties similar to those of SGLTs: 1) nonmetabolized substrates, 3-O-methyl glucoside and α -methyl-glucopyranoside, mimic glucose in reducing gastric emptying and stimulate the release of 5-HT and GLP-1 from the gut and 5-HT and GLP-1 from neuroendocrine cell models; 2) 5-HT and GLP-1 release are blocked by phlorizin; and 3) SGLT3 is expressed in an intestinal neuroendocrine cell line (57). It is now recognized that at least some of the intestinal glucose sensors are G protein-coupled receptors (GPCRs) found in enteroendocrine cells (40). Perhaps the strongest evidence for this is that mice lacking T1T3 and α -gustducin showed no upregulation of SGLT1 with increasing dietary carbohydrates. The finding that glucose sensors are expressed in different cells compared with the transporter suggests a chemical signaling pathway between cells, and this is consistent with neurogenin-3 mutations in human subjects, where a lack of enteroendocrine cells results in severe malabsorption (236).

F. Glucose Sensing in the Brain

The SGLT3 story now raises the possibility that other SGLTs may behave as glucose sensors especially since these genes are expressed throughout the body (Table 1). This is of particular relevance in the brain, where specialized neurons controlling sleep, appetite, and hormone secretion behave as glucose detectors (for review, see Ref. 56). There are two types of glucose-sensing neurons, glucose-excited and glucose-inhibited neurons in the hypothalamus and brain stem, whose rate of firing either increases or decreases in response to extracellular glucose. While the current dogma is that these glucose responses are mediated via K_{ATP} as in pancreatic β -cells, there is emerging evidence that SGLTs are involved. Namely, glucose-excited neurons are also stimulated by nonmetabolized SGLT substrates, such as α -MDG, and the response is blocked by the SGLT inhibitor phlorizin and the absence of Na^+ (Fig. 33) (154).

There is also RT-PCR evidence that SGLT1 and -3 are expressed in the hypothalamus (see also section V). Given the coexpression of SGLTs and GLUT3 in neurons, it is unlikely that the SGLTs in neurons are simply required for glucose uptake. It is more likely that these cells respond to changes in ambient glucose concentrations by depolarization of the membrane potential (see Fig. 3). The α MDG-stimulated firing of glucose-excited neurons is probably mediated by an increase in Ca^{2+} influx. In summary, SGLT genes may have important physiological roles throughout

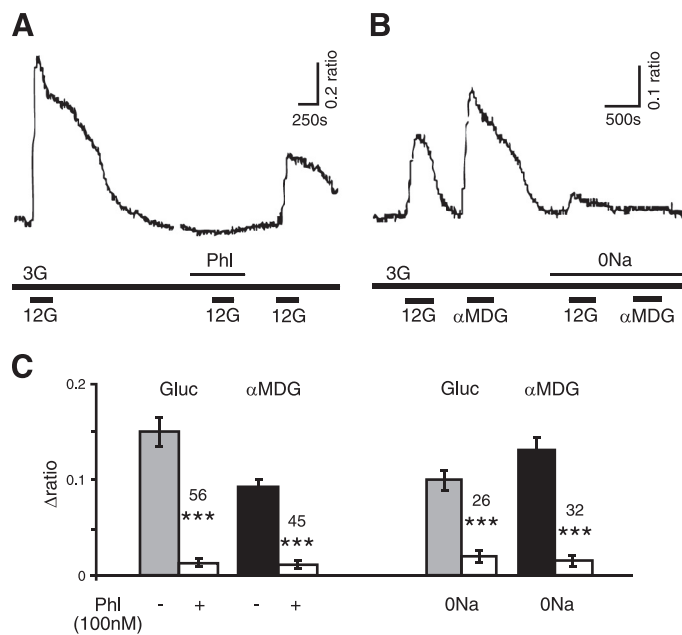


FIG. 33. Response of glucose-excited hypothalamic neurons to α MDG, phlorizin, and Na^+ . The intracellular $[\text{Ca}^{2+}]$ of cultured hypothalamic neurons was measured based on the ratiometric images of intracellular fura 2-AM (340/380 nm excitation, >510 nm emission). A: the responses to the addition of 12 mM glucose (G) in the presence and absence of 100 nM phlorizin (Phl). B: the responses to glucose and α MDG in the presence and absence of Na^+ . C: histogram of pooled data from A and B with the number of cells tested in the presence and absence of phlorizin or Na^+ . [From O'Malley et al. (154).]

the body not only as Na^+ /glucose cotransporters but as Na^+ uniporters, water and urea channels, and glucose sensors.

XIV. PHYSIOLOGY AND PATHOPHYSIOLOGY

A. Regulation of Expression

Ongoing studies are examining the regulation of SGLT1 and SGLT2 expression at the mRNA level, mostly in the kidney and intestine in diabetes and as a function of diet. The promoters of human and sheep SGLT1 have been mapped (143, 229) and, at least in the STC-1 cell line, sheep promoter activity is activated by glucose through a PKA pathway (41). Both the SGLT1 and SGLT2 promoters contain binding sites for human hepatocyte nuclear factor 1 (HNF-1) that enhance promoter activity (143, 172). Knockout mice ($\text{HNF1}\alpha^{-/-}$) suffered from a renal Fanconi syndrome where there was severe glucose, phosphate, and amino acid urinary wasting but there was no intestinal phenotype (172). The glucosuria was caused by a defect in SGLT2 expression. These results suggest that in the mouse $\text{HNF1}\alpha$ regulates renal SGLT2 expression but not intestinal SGLT1 expression.

Unfortunately, a lack of well-characterized antibodies means that there are a limited number of studies on

the regulation of protein expression in either the intestine or kidney. Arguably one of the most careful studies is that on the expression, SGLT1 and GLUT2 in the intestinal biopsies of diabetic and control human subjects (43). There was a three- to fourfold increase in SGLT1 and GLUT2 mRNA and protein levels, and the activity of Na^+ /glucose cotransport in brush-border membrane vesicles also increased threefold. The molecular mechanism underlying this increase is unknown and is complicated by the fact that mature enterocytes normally express SGLT1, and epithelial turnover occurs with a half-time of 3–4 days. In both the intestine and kidney of animals, the changes in SGLT1 and SGLT2 mRNA levels with different experimental protocols (diet, aging, diabetic model) were generally less than fivefold.

A notable exception is the change in intestinal transport activity and protein level in sheep, where the level of glucose transport decreased by two orders of magnitude on weaning (201, 243). Both the rate of Na^+ /glucose cotransport and SGLT1 protein in brush-border membranes drop by 200-fold when lambs are weaned and dietary carbohydrate fails to reach the small intestine, while there is a modest fourfold reduction in SGLT1 mRNA (114). Surprisingly, infusion of glucose into the intestine of adult sheep increased the level of transporter activity 100-fold, but the mRNA levels only increased 2-fold. This suggested translational or posttranslational regulation of the transporter in brush-border membrane. Infusion of 30 mM glucose, fructose, or 2-deoxy-glucose into the intestine of the ruminant sheep for 3 h returned the level of brush-border Na^+ /glucose cotransport and protein to the preruminant state after several days (42). This body of work has led to the conclusion that SGLT1 upregulation is mediated by a glucose sensor that initiates a signaling pathway linked to a cAMP-PKA pathway that takes several days to act.

Over the shorter term of minutes, activation of the cAMP pathway results in the recruitment of an intracellular pool of transporters to the plasma membrane. The experiments were performed on rabbit SGLT1 expressed in *Xenopus laevis* oocytes. With the use of membrane-permeable 8-BrcAMP to activate PKA, there was a reversible 30% increase in the maximum rate of Na^+ /glucose transport that occurred within minutes, whereas activating PKC with membrane-permeable *sn*-1,2-dioctyrtanoylglycerol (DOG) resulted in a decrease in the maximum rate of transport by 60% (72). There were no changes in the kinetics of SGLT1 apart from the increase in the maximum rate of transport. These changes in maximum transport rate were due to changes in the number of transporters in the plasma membrane. Both 8-BrcAMP and DOG increased the number of hSGLT1 molecules in the membrane, as did calyculin A, an inhibitor of phosphatases 1 and 2A. Even though there are four PKC and one PKA conser-

sus sites in human SGLT, we have suggested that this regulation occurs by regulated endo- and exocytosis and not phosphorylation of SGLT1.

Figure 34 shows thin-section and freeze-fracture electron micrographs of the 120-nm vesicles in the cytoplasm fusing with the plasma membrane of *Xenopus laevis* oocytes (248). Note the increase in intramembrane particles (SGLT1 proteins) in the SGLT1 expressing oocytes. The freeze-fracture images of vesicles isolated from the cytoplasm of SGLT1-expressing oocytes show that there are 10–20 SGLT1 proteins per vesicle. Given the rate of cotransporter insertion into the membrane ($250,000 \text{ s}^{-1}$), we estimate that 10,000 of these vesicles fuse with the oocyte plasma membrane per second. Since the membrane area increased by only $60 \mu\text{m}^2/\text{s}$, equivalent to fusion of 1,500 120-nm vesicles, we suggest that concurrent endocytosis accounts for the smaller increase in area. With an average number of transporters in the plasma membrane before stimulation of $2.5 \times 10^{11}/\text{oocyte}$, a 30% increase 30 min after 8-BrcAMP treatment represents an insertion rate of $1 \times 10^7 \text{ SGLT1/s}$. For the area of an oocyte plasma membrane, $30 \times 10^6 \mu\text{m}^2$, this is

equivalent to a fusion rate of $1 \text{ vesicle} \cdot \mu\text{m}^{-2} \cdot \text{s}^{-1}$ (248). This rapid insertion of SGLT1 into the plasma membrane indicates an intracellular reserve pool of vesicles within the cell poised to fuse with the cell membrane. There is evidence that cAMP and theophylline increase the maximum velocity of SGLT1 activity in enterocytes within 20 min (197), presumably by a similar mechanism.

One factor that may be involved in the regulation of transcription and trafficking of SGLT1 in the intestine is the regulatory gene RS1 (98, 101, 232, 233). In RS10 null mice, SGLT1 was upregulated and the mice became obese, apparently due to an increase in insertion of SGLT1 vesicles from the *trans*-Golgi network.

B. Intestinal Absorption

The currently accepted dogma is that glucose and galactose absorption occurs across mature enterocytes in two stages: the first is the uphill accumulation of these hexoses across the brush-border membrane by SGLT1, and the second is the downhill transport from the cell into

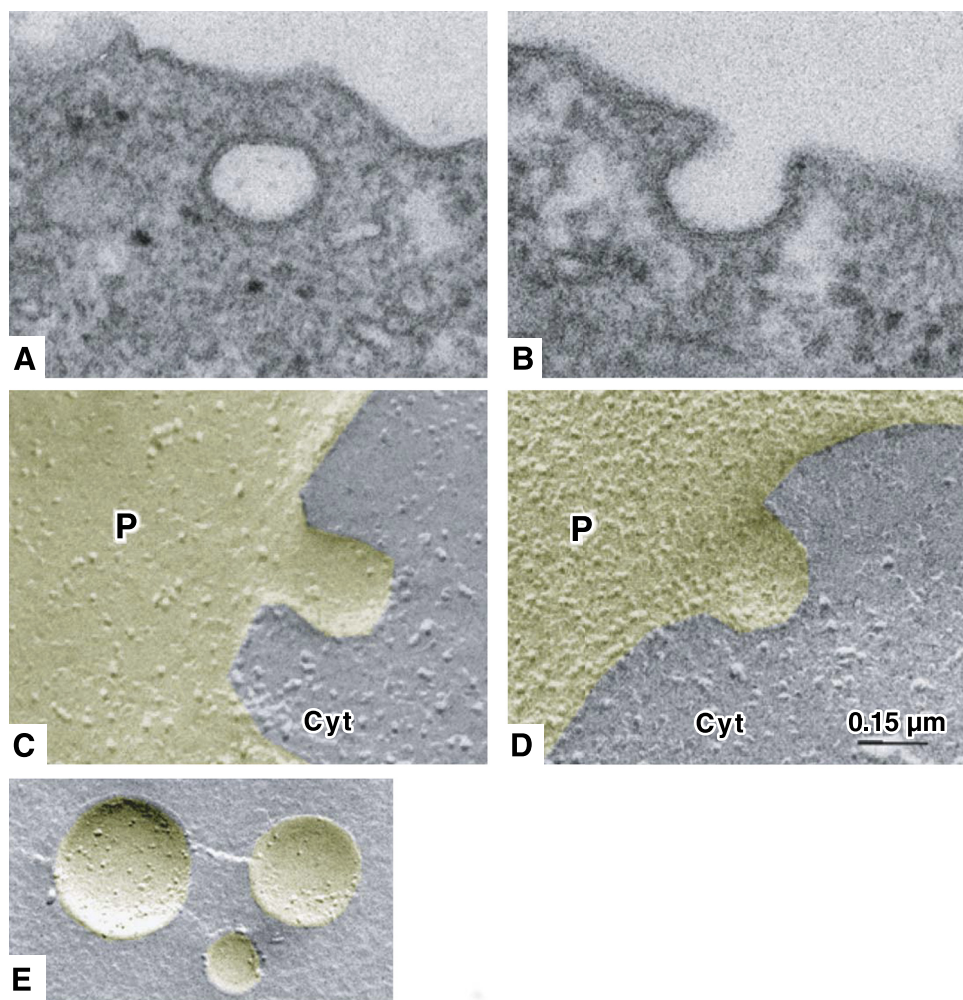


FIG. 34. Vesicle trafficking in oocytes. Thin-section electron micrographs (A and B) and freeze-fracture electron micrographs (C and D) showing membrane vesicles in *Xenopus laevis* oocytes expressing rabbit SGLT1. A and B show 120-nm-diameter vesicles approaching and fusing with the plasma membrane, and C and D show the P-face (P) of similar vesicles containing 7.5-nm-diameter SGLT1 intramembrane particles (see also Fig. 2). Cyt, cytoplasm. Magnification, $\times 150,000$; scale bar, $0.15 \mu\text{m}$. (248). E shows a freeze fracture of membrane vesicles isolated from oocytes expressing R427A-SGLT1 (a trafficking mutant, Ref. 135) using density gradient centrifugation. The fraction containing R427A-SGLT1 was identified using Western blotting. (From B. A. Hirayama, M. Kremann, G. Zampighi, and E. M. Wright, unpublished data.)

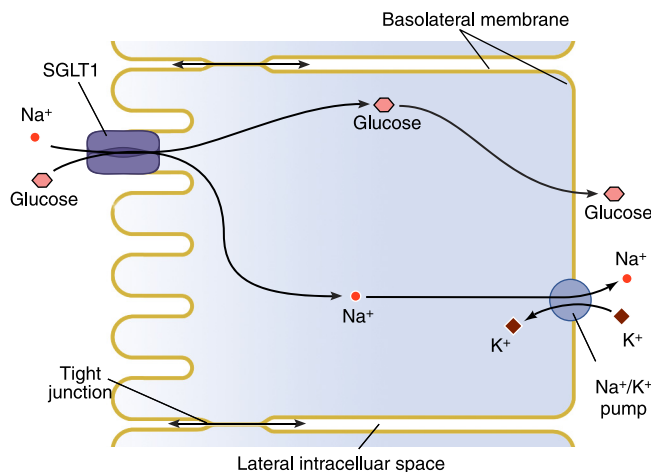


FIG. 35. Model for glucose and galactose transport across enterocytes. Glucose (and galactose) is accumulated within the cell from the gut lumen by SGLT1 in the brush-border membrane. The energy for uphill sugar transport is provided by the sodium electrochemical potential gradient across the brush-border membrane. The two sodium ions that enter the cell with each sugar molecule are pumped out across the basolateral membrane by the Na^+/K^+ pump. Sugar that accumulates within the cell exits across the basolateral membrane into the blood.

blood through GLUT2 present in the basolateral membrane (Fig. 35). Soon after the cloning of SGLT1 from the rabbit small intestine, it was shown using both Western blotting and immunocytochemistry that the protein is only expressed in the brush-border membrane (70, 209). The NH_2 -terminal domain of SGLT1 (amino acids 1–19) appears to determine the targeting of the protein to the brush-border membrane (207). There was some supranuclear positive staining in the enterocytes on the mid-villus region consistent with the biosynthetic pathway. Immunostaining of the human brush border is shown in Figure 36A.

Perhaps the most definitive evidence for the role of SGLT1 in sugar transport across the human brush-border membrane came from studies of the disorder glucose galactose malabsorption (see below), the result of mutations in the SGLT1 gene. Figure 36B shows immunocytochemical location of SGLT1 in the patient with a C292Y mutation on both alleles. In the duodenal biopsy, the C292Y-SGLT1 protein was trapped between the nucleus and the brush-border membrane (Fig. 36B). Studies of the mutant protein expressed in *Xenopus laevis* oocytes also showed that there is no $\text{Na}^+/\text{glucose}$ cotransport and that a trafficking defect prevents insertion of the mutant protein into the plasma membrane (142).

Although GLUT2 is expressed in the basolateral membrane of enterocytes, the role of this protein in glucose absorption is unclear based on studies of GLUT2 $^{-/-}$ mice and patients with the Fanconi-Bickel Syndrome (FBS), caused by mutations in GLUT2 (189, 206). Oral glucose tolerance tests were normal in both GLUT2 $^{-/-}$ knockout mice and FBS patients and cAMP increased

glucose absorption equally well in wild-type and GLUT2 $^{-/-}$ mice. In addition, in vivo experiments in rats showed that α MDG was absorbed across the intestine with kinetics similar to D-glucose and D-galactose (31) despite the fact that α MDG is not a substrate for GLUT2 (252). This suggests that a mechanism other than facilitated diffusion through GLUT2 is responsible for exit from the enterocyte. One yet-to-be explained result was the finding that absorption of 3-O-methyl-D-glucoside was abnormal in the GLUT2 $^{-/-}$ mice (206).

These observations on GLUT2 $^{-/-}$ mice and FBS patients raise doubts about the popular hypothesis that GLUT2 plays an important role in the regulation of glucose absorption across the intestine (see Ref. 89). A central tenet of this hypothesis is that in response to a glucose meal, GLUT2 is redirected into the brush-border membrane to account for the increase in sugar absorption. This is inconsistent with normal glucose absorption and regulation by cAMP in GLUT2 $^{-/-}$ mice and normal glucose absorption in FBS patients. There was a fundamental flaw in the design of Kellett's exper-

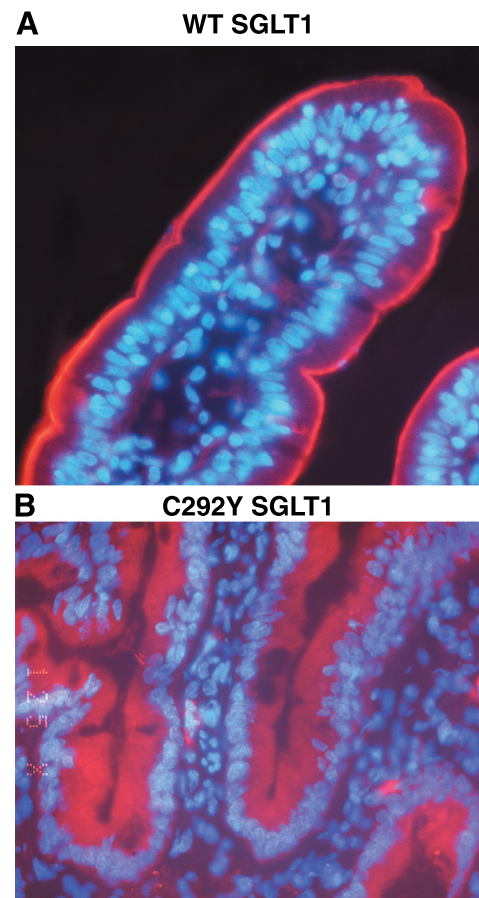


FIG. 36. SGLT1 immunostaining of intestinal biopsies from a control subject (A) and a glucose galactose malabsorption (GGM) patient with the homozygous C292Y-SGLT1 mutation (B). In each section, the nuclei are counterstained with DAPI. (From P. Lostao, B. A. Hirayama, and E. M. Wright, unpublished data.)

iments, where they dissected the contributions of SGLT1 and GLUT2 to glucose absorption in rats on the basis of the phloretin inhibition (90); they assumed that 1 mM phloretin only inhibited GLUT2; and the phloretin-insensitive fraction of glucose absorption was through SGLT1. It has been well known that phloretin is a potent noncompetitive SGLT1 inhibitor with a K_i of 50 μM , e.g., Refs. 66, 159. This means that Kelletts's laboratory grossly underestimated the importance of SGLT1, and this is reinforced by the observation that glucose absorption can be totally defective in patients with mutations in *SGLT1*.

C. Oral Rehydration Therapy

Perhaps the most important medical application of SGLT1 is its critical role in the treatment of secretory diarrhea in children, the elderly, and immunocompromised patients. According to the World Health Organization (WHO), diarrhea caused by cholera is the second leading cause of childhood mortality, killing some 1.5 million children <5 years of age. Cholera infection causes massive diarrhea, resulting in dehydration that can lead to death unless the patient is rehydrated, which in adults may require 80 liters of intravenous fluids over 5 days (73). The challenge of such heroic fluid replacement to save the patient was overcome by the discovery that one could simply administer an oral rehydration solution (ORS) containing salt and glucose. The glucose in the ORS is absorbed along with two sodium ions by SGLT1 on the brush-border membrane, and water is either cotransported with the sugar and sodium, or follows by osmosis (see sect. XIIIIC). We estimate that, directly or indirectly, SGLT1 can promote about 6 liters of water absorption daily in the normal adult intestine. The current WHO/UNICEF oral rehydration solution contains 75 mM NaCl, 75 mM glucose, 20 mM KCl, and 10 mM sodium citrate with an osmolarity of 245 mosM, and commercial formulations in the United States and Europe are usually flavored to make the solution more palatable. In the field where ORS is not available, there are several homemade recipes that use locally available supplies of carbohydrate, see, <http://rehydrate.org>. In all cases, the ORS is designed to increase intestinal salt, sugar, and water absorption to match or exceed the secretory diarrhea caused by the toxin (see Fig. 35).

Since the first successful clinical trials of ORT in 1968 at the Cholera Research Laboratory in Dhaka (74, 171), the number of deaths has decreased dramatically, and this therapy has been extended to even include diarrhea caused by other pathogens, including rotavirus, *E. coli*, and *Yersinia* infections (179) in both developed and underdeveloped countries worldwide. In

1978, an editorial in the British medical journal *The Lancet* (2: 300–301) hailed ORT as the “most important medical advance of this (20th) century.” Readers interested in the historical steps and missteps in the development of oral rehydration therapy are referred to the review by Ruxin (186).

D. Glucose Galactose Malabsorption

GGM was first described in two reports in 1962 as a watery and severe diarrhea in newborn children that is fatal within weeks unless lactose, glucose, and galactose are removed from the infant’s diet (108, 119). The diarrhea ceases immediately on removing sugar and promptly resumes when lactose, glucose, or galactose are added back into the diet (250). It was predicted that GGM is due to a defect in the brush-border $\text{Na}^+/\text{glucose}$ cotransporter. This was confirmed by Eric Turk following the cloning of human SGLT1 (64, 222), when a homozygous mutation, D28N, was found in two sisters with GGM, and that each parent was a carrier for this mutation. In *Xenopus laevis* oocytes, the D28N SGLT1 protein was shown to be unable to transport glucose. Prenatal screening in two subsequent pregnancies in this large consanguineous family revealed that the probands’ sibling was a carrier and a cousin did not carry the mutation (141). This study also confirmed that GGM was an autosomal recessive disorder. Patients with GGM remain intolerant of glucose and galactose for the rest of their lives, and our oldest subject, now 58, lives an apparently normal healthy life on a sugar-free diet. His blood chemistries are within normal limits, but malabsorption symptoms return immediately on ingesting food with the offending sugars. There have been a number of reports of nephrocalcinosis in GGM children (see Ref. 203). It is thought that this may arise due to hypercalcemia, metabolic acidosis, and dehydration as renal tubule dysfunction, and these symptoms often resolve on removing glucose and galactose from the diet.

Over 80 patients with a diagnosis of GGM have been screened for mutations in the SGLT1 gene (55, 87, 105, 140, 203, 213). The most clear diagnosis of GGM includes observations that 1) the diarrhea returns when glucose or galactose, but not fructose, is added to the diet; 2) oral glucose tolerance tests produce flat blood glucose curves; and 3) positive glucose hydrogen breath tests indicate glucose malabsorption. In all but a few patients, mutations have been identified in *SGLT1* that cause the defect in sugar absorption (87, 142, 250). In several cases where no mutations were found, the diarrhea was found to be due to the novel disorder enteric anendocrinosis due to mutations in the neurogenin 3 gene (236). This indicates that signals from endocrine cells are required for normal absorption.

About 65% of GGM patients tested have the same mutation on each allele, and the remainder have different mutations on each allele, i.e., they are compound heterozygotes. There are only a handful of cases where the same mutation is found in unrelated families, but these families are of similar ethnic backgrounds. This may reflect an increase in the frequency of these variants in a given population (see below). The majority of mutations are missense, but nonsense, frame shift, splice-site, and promoter mutations have also been documented. The nonsense, frame shift, and splice site mutations all produce truncated proteins that are predicted to be unstable and/or nonfunctional. To determine whether a mutation causes an actual defect in glucose and galactose transport or is simply a polymorphism, it is essential to measure the transport activity of the mutant protein. This has usually been carried out using the *Xenopus laevis* expression system (55, 87, 140, 142, 222). We have confirmed that two truncated proteins, Y191X and R359X, are nonfunctional when expressed in *Xenopus laevis* oocytes (142). The missense mutations are distributed throughout the protein (see Fig. 37) with no particular "hot spots." Of the 27 mutations tested, all but 3 show dramatically reduced Na^+ /glucose transport activity, and the most common cause is a failure in the insertion of the protein into the plasma membrane as determined from charge (Q_{\max}) measurements, freeze-fracture electron microscopy,

and/or immunohistochemistry. In several patients with these homozygous mutations, we have also found using intestinal biopsies that the transporter is not inserted into the brush-border membrane of enterocytes (see Fig. 36). There are three nonfunctional mutant proteins that are inserted into the plasma membrane, R135W, Q457R and T460P, and one of these, Q457, has been found to be important in binding sugar (38) (see Fig. 17). The residues that are mutated to produce nonfunctional proteins are conserved in the SGLT family of proteins (see Fig. 190–7 in Ref. 250).

Three missense mutations that did not significantly alter the function of SGLT1, N51S, A411T, and H615Q, are not conserved in the SGLT family of proteins, but they were found at a high frequency, 9%, in the European-American population. As part of the University of California San Francisco Pharmacogenetics of Membrane Transporters Project (www.pharmacogenetics.ucsf.edu), we have examined 552 alleles in the Coriell Institute genomic DNA collection for variations in hSGLT1 (Fig. 38). Only 12 nonsynonymous mutations were found, and only 6 are at a frequency of >1%. Although these three common variants were found in our pool of GGM patients, it was second mutations that produced the defect in glucose transport. None of the GGM mutations has been found in this sample of 552 alleles, as expected from the rarity of the disorder.

SGLT1 Mutations

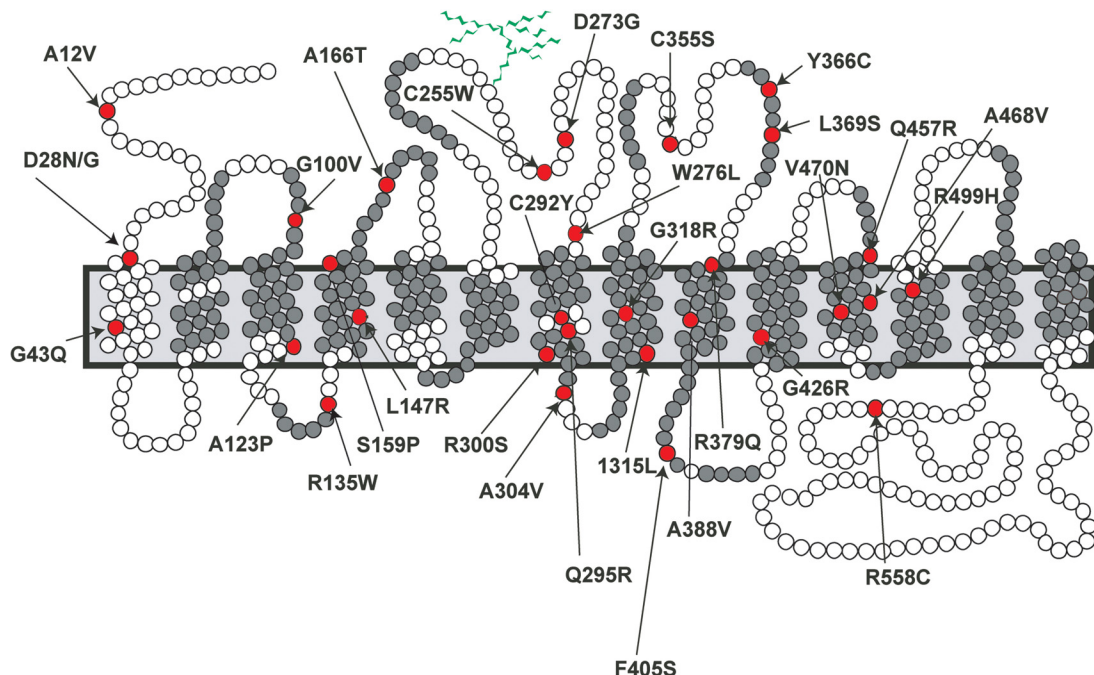
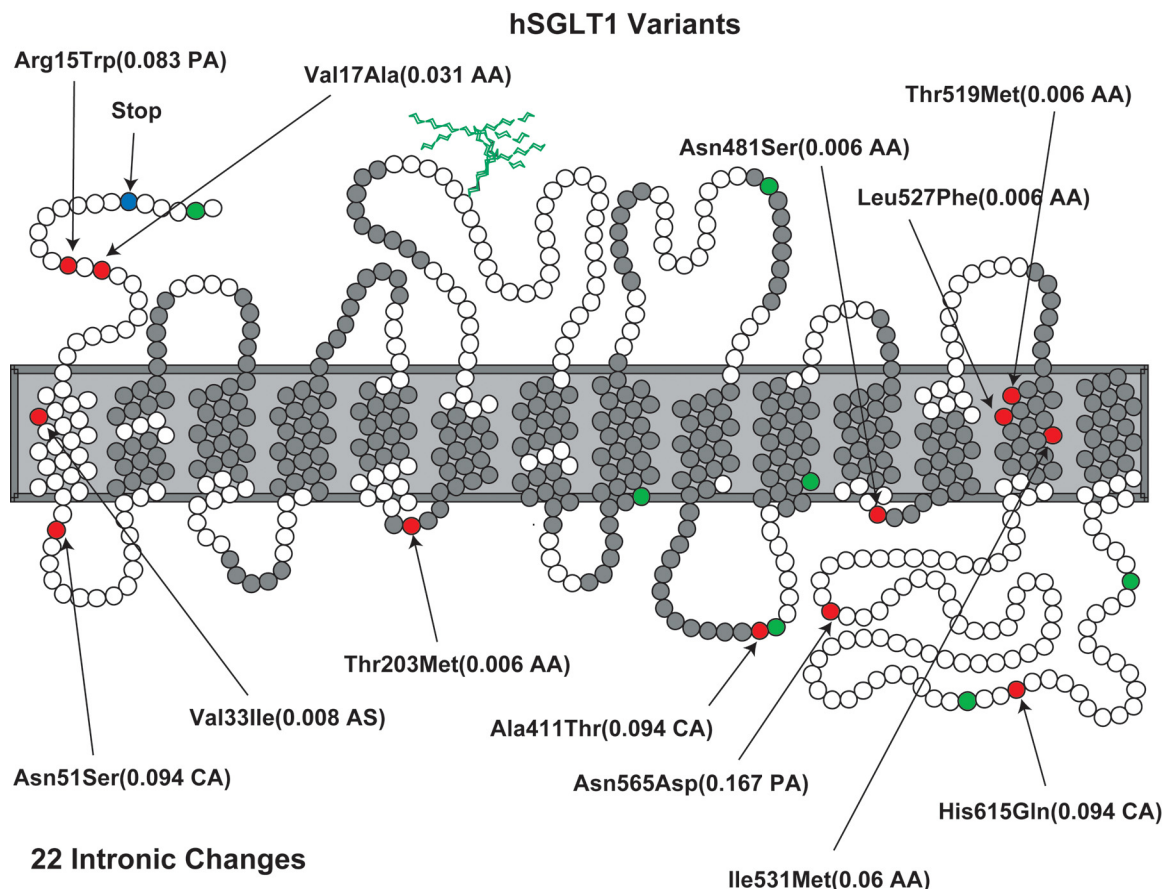


FIG. 37. Missense mutations of SGLT1 identified in patients with GGM. The mutations are shown on a secondary structure model with the transmembrane helices from the vSGLT structure highlighted in gray. [Revised from Wright (244).]



22 Intronic Changes

FIG. 38. Intronic changes in the hSGLT gene in 552 alleles. The 22 variants include 12 nonsynonymous changes. The frequency of each polymorphism in each population is included in parentheses. CA, Caucasian; AA, African American; AS, Asian; PA, Pacific Island. Synonymous variants are shown in green.

E. Enteric Infection

There is emerging evidence that upregulation of intestinal SGLT1 may afford protection against enteric infections. High glucose concentrations (25 mM) protected SGLT1 transfected Caco-2 cells against apoptosis induced by bacterial lipopolysaccharide (LPS) (259). Furthermore, LPS increased glucose transport activity in these cells. These studies have been applied to *Giardia duodenalis*-induced apoptosis in this system, and extended to demonstrate that *G. duodenalis* proteolytic fragments increased SGLT1 expression in the apical membrane (260). Arguably, the most convincing demonstration of the cytoprotective effects of SGLT1 was the demonstration that oral glucose gave 100% protection against lethal endotoxic shock in mice (160). Lethal endotoxic shock was induced by LPS and pretreatment with oral glucose, or the nonmetabolized SGLT1 substrate 3-O-methyl-D-glucose, resulted in 100% survival of mice against the insult. These studies suggest a novel immunological role for SGLT1 and new approaches to managing severe sepsis infections that result in chronic diseases such as inflammatory bowel disease (IBD).

F. Renal Reabsorption

Glucose is freely filtered across the renal glomerulus, amounting to $180 \text{ g} \cdot \text{day}^{-1} \cdot 1.73 \text{ m}^{-2}$ in adults (for a review, see Ref. 245). In healthy individuals, $<0.5 \text{ g/day}$ is lost in the urine, so $>97\%$ of the filtered load is reabsorbed. The urine remains virtually free of glucose within the normal range of blood (plasma) glucose levels (4–10 mM), but as the plasma concentration exceeds $\sim 14 \text{ mM}$, glucose appears in the urine and above 20 mM the excretion increases in proportion to the filtered load. In other words, the reabsorption of glucose from the glomerular filtrate saturates at $\sim 425 \text{ g/day}$ with an apparent K_m of $\sim 10 \text{ mM}$. The most common cause of glucose in the urine of patients is due to the high blood glucose levels associated with diabetes. Micropuncture studies of frog and rat nephrons have demonstrated that the glomerular filtrate is glucose-free when it reached the end of the proximal tubule (Fig. 39, A and B). Microperfusion experiments with isolated nephrons from rabbits established that active glucose reabsorption occurs in the “early” convoluted proximal tubule via a low-affinity (K_m 2 mM) high-capac-

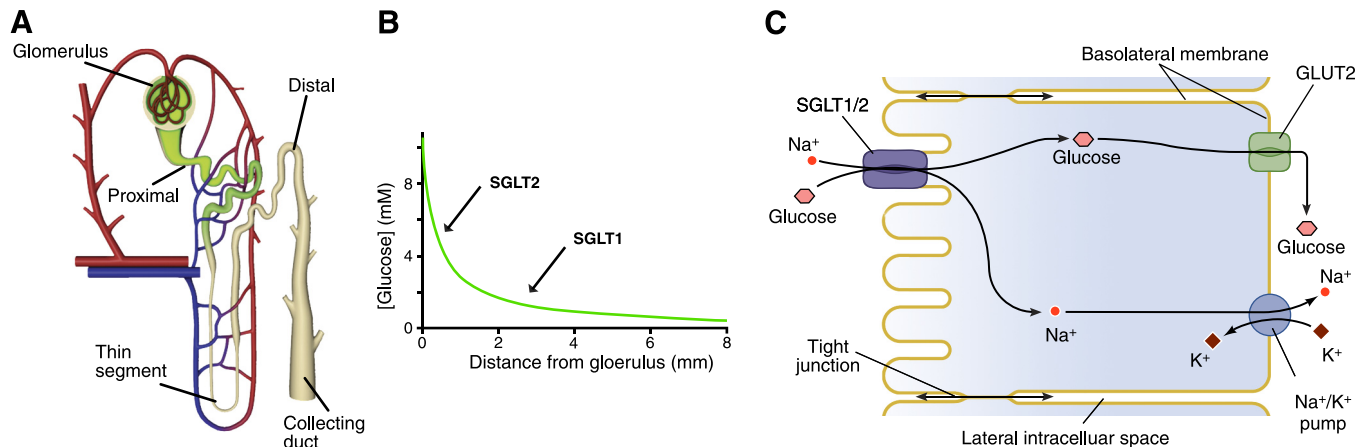


FIG. 39. Glucose reabsorption from the proximal tubule. *A*: anatomical arrangement of a kidney nephron with its blood supply. *B*: summary of the results of micropuncture experiments to measure the glucose concentration as fluid flows freely along the tubule from the glomerulus (244). *C*: a model for glucose reabsorption across the epithelium of the proximal tubule. Similar to that in enterocytes (Fig. 34), the Na^+ electrochemical potential gradient provides the energy source, and transport across the epithelium occurs in two steps. Glucose is transported across the apical membrane by SGLT1 and SGLT2. SGLT2 is predominantly located in the S1 and S2 segments and SGLT1 is in S3. GLUT2 is the major glucose transporter across the basolateral membrane.

ity system ($80 \text{ pmol} \cdot \text{min}^{-1} \cdot \text{mm}^{-1}$) system, whereas active reabsorption in the late proximal tubule occurred by a high-affinity (K_m 0.5 mM), low-capacity system ($10 \text{ pmol} \cdot \text{min}^{-1} \cdot \text{mm}^{-1}$) system.

Further evidence for two transport systems in the human kidney came from brush-border membrane vesicle experiments where there was a hint of low- and high-affinity Na^+ /glucose cotransport systems. Additional studies on brush-border membranes from the outer cortex and outer medulla of rabbit kidney provided additional support for two different SGLTs: one in the outer cortex had a glucose K_m of 6 mM and one in the outer medulla with a K_m of 0.3 mM, and the low-affinity one was more sensitive to phlorizin than the high-affinity one. These two transporters have come to be called SGLT2 and SGLT1 (245) (Fig. 39), and their properties are in close agreement with those of the cloned SGLT1 and SGLT2 proteins (Table 1) (81).

The cellular mechanism of renal glucose reabsorption is shown in Figure 39C. The two-step process is similar to that in enterocytes with uphill transport across the brush border into the epithelium and downhill facilitated diffusion from the cell into the blood across the basolateral membrane. Antibodies against the cloned rabbit SGLT1 were used to examine the location of SGLT1 in the rat kidney (22, 210), and it was found that the protein was present in the brush-border membrane of all three segments of the proximal tubule. This has been confirmed recently with another antibody (4). In proximal tubule, GLUT1 was only found in the basolateral membrane of the S3 segment (210). Basolateral GLUT2 colocalizes in cortical tubules expressing brush-border SGLT1 (22). Immunohistochemistry localized SGLT2 to the brush border of the early proximal tubule in mice, and this was absent in *SGLT2*^{-/-} animals (227). The *SGLT2*^{-/-} mice exhib-

ited glucosuria, and free-flow micropuncture studies showed that there was no glucose reabsorption in the early proximal tubule.

Unlike the small intestine, GLUT2 is very important in the normal reabsorption of glucose in the kidney, as patients with FBS exhibit massive renal glucosuria (244). Those patients who have a homozygous premature stop codon in the GLUT2 gene had a renal glycosuria of up to 200 g/day. This indicates that GLUT2 is the major basolateral glucose transporter involved in the reabsorption of the glucose filtered load. Basolateral GLUT1 and GLUT2 are also involved in the entry and exit of glucose into other segments of the nephron, e.g., in the release of glucose produced by gluconeogenesis.

Mutations in brush-border SGLT1 and SGLT2 also cause renal glucosuria, but in the case of SGLT1, the glucosuria that accompanies GGM is mild, e.g., one patient with severe SGLT1 mutations (G426R and S159P) lost only 1.5 g glucose/day in the urine (244).

G. Familial Renal Glucosuria

This is a rare autosomal recessive disorder where glucose is excreted into the urine, >1 g/day, when blood glucose levels and oral glucose tolerance tests are normal (244). There are no other renal abnormalities, even when the glucose excretion exceeds 100 g/day, and there are no other systemic consequences. In the case of one patient with severe renal glucosuria (>109 g/day), who was re-evaluated 20 years after glucosuria was first detected, there were no chronic nephrological complications (194). Table 6 contains a summary of the glucosuria and the SGLT2 mutations in five patients with severe FRG (13, 190, 244).

Glucose excretion ranges from 1 to 162 g·1.73 m⁻²·day⁻¹, and the mutations are those expected for an

TABLE 6. *Familial renal glucosuria*

Subject	Glucose Excretion, g·1.73 m ⁻² ·day ⁻¹	Allele 1	Allele 2
01-1	>126	P347X	P347X
06-1	69	W440X	W440X
15-1	202	R137H	Δ385-8
15-2	80	R137H	Δ 385-8
17	30-92	Y128X	Y128X

Renal glucose excretion and SGLT2 mutations in patients with familial renal glucosuria (13, 190, 244).

autosomal recessive inheritance: 12 homozygous and 7 compound heterozygous that include premature stops, frame shifts, and missense mutations. So far, none of the FRG mutations has been tested for functional SGLT2 effects, due to the low expression of SGLT2 in heterologous expression systems, so it is difficult to relate the mutations to the severity of the glucosuria. However, it is noteworthy that 1) in subjects with severely truncated proteins, one excretes most of the filtered load (374X) while two others reabsorb about half of the filtered load (W440X and Y128X) (Table 6); and 2) there is a huge discrepancy in the glucosuria between two siblings with the same mutations. In subject 15-1, the glucose excretion is 202 g·1.73 m⁻²·day⁻¹, while in subject 15-2 it is

only 80 g·1.73 m⁻²·day⁻¹. This, combined with the 50% inhibition of glucose reabsorption by SGLT2 inhibitors (95), suggests that SGLT2 may not be solely responsible for glucose reabsorption in the kidney. Phlorizin is known to inhibit reabsorption completely (16), and this points to the involvement of another SGLT. It is unlikely this is SGLT1, as the data suggest this transporter accounts for <10% of the normal amount absorbed. Another possibility is SGLT5, expressed exclusively in the renal cortex (Table 1).

SGLT2 mutations found in subjects with FRG are shown on a secondary structure model in Figure 40. These are distributed throughout the protein in both transmembrane domains and hydrophilic loops, and none is at the predicted sugar or Na⁺ coordination sites, although F453L is at a predicted outer gate residue (see above). Several SGLT2 mutations occur in similar locations to GGM mutations in SGLT1, e.g., R137H, R300C, G304K, and R499H (Fig. 37). While the effect of mutations on SGLT2 function has not yet been reported, we note that in SGLT1 mutations at R135W, R300S, A304V, and R499H produce defects in glucose transport, largely through trafficking problems (142, 250). The truncated SGLT2 proteins, 128X, 186X, 347X, and 440X, are not expected to produce stable functional proteins.

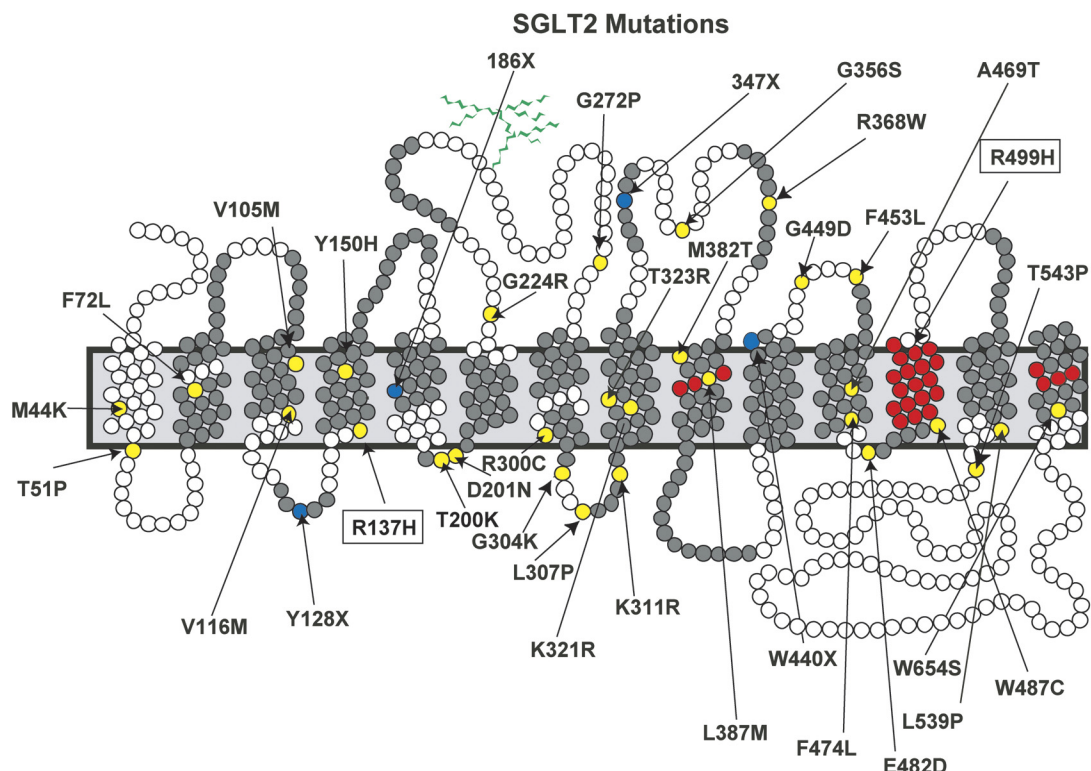


FIG. 40. The location of SGLT2 mutations on a secondary structure model of the protein. The gray circles indicate the location of TM2-TM14 based on the crystal structure of vSGLT (48). Missense mutations are highlighted in yellow, premature stops in blue, and deletions in red. As with GGM mutations in SGLT1, the mutations are distributed throughout the protein. [Modified from Wright (244).]

In summary, SGLTs play a major role in salvaging glucose from the glomerular filtrate to avoid loss of this nutrient to the urine. However, in terms of renal function, this is not deemed essential as subjects with the rare disorder known as FRG do not have any chronic kidney complications, nor do they become hypoglycemic. This has encouraged the pharmaceutical industry to develop SGLT2 inhibitors to lower blood glucose levels in diabetics (see below).

H. Bile, Milk, and Saliva

It has long been known that glucose enters the bile in the liver and then is reabsorbed in the interhepatic bile ducts by SGLT1 in the apical membrane and GLUT1 in the basolateral membrane of cholangiocytes (111). This was confirmed in studies of glucose transport in microperfused rat intrahepatic bile ducts and further demonstrated that glucose transport was accompanied by water transport (144). In vivo it was reported that as the rate of glucose absorption increased there was a reduction in bile flow, and when glucose absorption was inhibited by phlorizin, the bile flow increased. This relationship between glucose and bile flow may contribute to the low bile flow, and associated symptoms such as jaundice, in diabetes.

Glucose supply to the lactating mammary gland is important in providing energy and as precursor for lactose production and secretion. It has been argued that glucose transporters in the basolateral membrane of mammary epithelia are essential for milk production. The expression of glucose transporters in the human lactating mammary gland was examined in a novel manner by Obermeier et al. (155) when they examined the genes expressed in epithelial cells isolated from fresh milk. They found SGLT1 mRNA by RT-PCR and SGLT1 protein by Western Blot analysis, but did not find GLUT1. SGLT1 mRNA and protein was also found in rat lactating mammary gland tissue (198). A more complete analysis of glucose transporter gene expression has been reported for the bovine mammary gland (266). The largest increase in expression, from -40 to +7 days after parturition, was for GLUT1 and GLUT8 (10- to 100-fold), while there were more modest increases in SGLT1 and SGLT2 expression. At this time, we are unaware of any studies on the distribution of the SGLTs and GLUTs between the apical and basolateral membranes. Likewise, we are unaware of any mammary gland phenotype in women with severe mutations in SGLT1 (GGM) or SGLT2 (FRG).

There has been an increasing awareness of oral health complications in diabetes and the possible involvement of the salivary glands (187). Impaired salivary gland function has been reported in diabetes, including low rates of flow and high glucose concentrations. SGLT1 was first reported to be expressed in the

basolateral membrane of sheep parotid glands (212) and more recently in the apical membrane of intercalated ducts of the rat submandibular gland (4). We have also found SGLT1 in the apical membrane of human sublingual glands (Hirayama and Wright, unpublished data). What is the functional significance of SGLT1 expression in salivary glands, glucose secretion by the acinar cells, and glucose reabsorption in the ducts? It is possible that glucose reabsorption from the duct occurs by a two-stage process, i.e., apical Na^+ /glucose cotransport through SGLT1 followed by downhill transport across the basolateral membrane through a GLUT; this should be tested in microperfusion studies on isolated ducts from control and diabetic animals. Again, it would be informative to evaluate salivary secretion in subjects with GGM and with FRG.

I. Cancer

Glucose is a major source of energy, and the demand for glucose in cancer cells is even higher than normal cells. This is the basis for the detection and staging of tumors using 2FDG (see sect. VC). However, some tumors do not accumulate 2FDG, a substrate for GLUTs but not SGLTs, increasing interest in the expression of SGLTs in cancer. Inspection of the EST databases (www.ncbi.nlm.nih.gov/unigene) indicates that SGLT1 is expressed in colorectal, head and neck, and prostate tumors, and SGLT2 is expressed in colorectal, gastrointestinal, head and neck, and kidney tumors as well as in chondrosarcomas and leukemia. There are a handful of publications on the mRNA levels of SGLT1 and SGLT2 and immunohistochemistry of SGLT1 in primary tumors, and metastatic lesions of lung, pancreatic adenocarcinomas, and head and neck cancers (65, 84). SGLT1 was expressed in well-differentiated squamous cultures of head and neck carcinomas, SGLT2 was expressed in metastatic lesions of lung cancers, and SGLT1 protein was reported to be expressed in primary pancreatic adenocarcinomas (14). We were unable to detect specific SGLT1 expression in several samples of other tumors (lung, liver, testis, sarcomas, breast, colon, prostate, and squamous cell carcinomas of the mouth). No antibodies are yet available to screen for other SGLTs in these and other tumors.

Recently, an intriguing role for SGLT1 in the survival of cancer cells was postulated where epidermal growth factor receptor (EGFR) stabilizes SGLT1 to prevent autophagic cell death (239). This may explain the resistance of tumor cells to chemotherapeutic agents and tyrosine kinase inhibitors. A novel strategy has also been proposed to deliver chemotherapeutic agents into tumor cells through SGLTs. This involves covalently linking a nitrogen mustard reagent to D-glucose though the β -C1-OH

group, e.g., β -D-glucosylisphosphoramide mustard (glufosfamide). These drugs are currently in phase I and II trials for pancreatic adenocarcinomas and other solid tumors (19, 200).

J. Diabetes

This chronic disease is a disorder of glucose homeostasis where blood glucose levels greatly exceed the normal levels, $>>10$ mM, and there is reduction in insulin secretion and/or sensitivity. If the hyperglycemia is left untreated, it results in glucose toxicity, which damages blood vessels and peripheral nerves, leading to blindness, kidney failure, peripheral neuropathy, cardiovascular disease, and other serious complications. It is estimated that (25 million) patients have diabetes, close to 10% of the adult population in the United States, and the number is growing at an alarming rate. One of the earliest symptoms is a loss of glucose to the urine due to hyperglycemia overwhelming the reabsorption capacity of SGLTs in the proximal tubule (see sect. IXD). Current therapies to combat this disease are centered on controlling blood glucose levels by increasing insulin secretion, improving insulin sensitivity, and reducing liver glucose output and intestinal glucose absorption. As the disease progresses, patients require combinations of medicines and, unfortunately, adverse side effects compromise compliance and the health of the patient.

There is a growing interest in alternative therapies to manage diabetic patients, and one is to control blood glucose by inhibiting SGLT2 in the kidney. The pharmaceutical industry has been encouraged by 1) studies demonstrating that intravenous phlorizin decreased blood glucose levels without producing hypoglycemia in diabetic animals, and this was accompanied by an improvement in insulin resistance (185); 2) reports that FRG is a benign disorder with no long-term renal abnormalities (see sect. IXE); and 3) cloning of the "renal" SGLTs enabling in vitro studies (see above). The strategy has been to develop oral SGLT2 inhibitors. Oral phlorizin does not fit the bill as it blocks gastrointestinal absorption of glucose and thus produces osmotic diarrhea. Furthermore, phlorizin is hydrolyzed to glucose and phloretin by the intestinal brush-border lactase-hydrolase, so little of the intact molecule is absorbed.

The proof of concept for SGLT2 targeted therapy was provided by Oku et al. (156) who demonstrated that a prodrug, T-1095, was absorbed from the gut into the circulation; this resulted in renal glucose excretion in diabetic animals and lowered blood glucose levels. T1095 also suppressed postprandial hyperglycemia and reduced hyperinsulinemia and hypertriglyceridemia in diabetic rodents. In the decade since, there have been at least 21 SGLT2 inhibitors that entered the drug pipeline. Most

have exploited the same chemical space as phlorizin (see sect. VIIIC), and many of these compounds are in phase I to III clinical trials. To cite one example, we focus on the C-aryl glucoside dapagliflozin (Fig. 19). This drug had a SGLT2 inhibitor constant (EC_{50}) of 1 nM and a selectivity of $\sim 1,200$ for SGLT2 over SGLT1 (237).

Safety studies of dapagliflozin in healthy human subjects (95) indicated that the drug is well tolerated with minimal adverse events and no clinically relevant changes in vital signs relative to the placebo controls. The drug is rapidly absorbed with plasma levels reaching a maximum 2 h after oral administration and thereafter falling with a half-time of 17–18 h; unlike the O-glucosides, the C-aryl-glucosides are resistant to glucosidases. Ninety-seven percent of the drug stays bound to plasma proteins, and this probably accounts for the low renal clearance and urinary excretion. There was a dose-dependent excretion of glucose in urine up to a maximum of 60–80 grams/24 h, i.e., 50% inhibition of renal glucose reabsorption, and this persists with daily oral dosing for 2 wk. In these healthy volunteers, there was no reduction in serum glucose or insulin. The maximum reduction in glucose reabsorption of $\sim 50\%$ is surprising since dapagliflozin inhibits SGLT2 completely in vitro (see sect. VIIIC). This is probably related to the fact that in vivo 97% of the drug is bound to plasma proteins and $<2\%$ of the injected dose is recovered in the urine.

Phase II clinical trials with type 2 diabetic patients for 2–12 wk and phase III trials for up to 24 wk have been reported (51, 96, 120). In general, the highest doses of dapagliflozin produce a sustained 30–65 g/day urinary glucose excretion, a $22 \pm 10\%$ reduction in fasting serum glucose, and a $20 \pm 10\%$ reduction in postprandial glucose absorption (area under the plasma glucose concentration curve). The loss of urinary glucose, 200–300 kcal/day, results in weight loss (up to 2.5 kg), increases in urine volume (up to 470 ml/day) and hematocrit (up to 3%), and an associated modest reduction in diastolic blood pressure of 2–5 mmHg. The results so far suggest that anti-SGLT2 inhibitors may be useful in reaching the goals for low glycemic control in type 2 diabetic patients and reducing glycosylated hemoglobin (Hb A1C) levels to $<7\%$. According to these reports, the dapagliflozin treatment for up to 24 wk produces no remarkable clinical side effects relative to the placebo controls, as expected from the long-term follow up with one patient with massive FRG (194).

In summary, the pharmaceutical industry has in a remarkably short time advanced the proof of concept of SGLT2 inhibitors for managing hyperglycemia in diabetic patients to phase III clinical trials. Only time will tell if these novel drugs will be effective and safe in patients.

XV. OUTLOOK

To gain perspective into the future, we look at the past and ask: what have we learned since 1987?

First, SGLT1 was the initial member of a new gene family of 12 members, SLC5, only 4 of which are glucose transporters. Second, it was discovered that GGM and FRG, rare autosomal defects in glucose transport, are the result of mutations in SGLT1 and SGLT2. Third, in addition to the intestine and kidney, SGLT1 and -2 are widely distributed in the body, including brain, salivary glands, lactating mammary gland, and bile ducts. Fourth, SGLTs are multifunctional proteins behaving as Na^+ /glucose cotransporters, water and urea channels, glucose sensors, and coupled water and urea transporters. Fifth, an eight-state ordered kinetic model accounts quantitatively for the observed steady-state kinetics of SGLT1. Sixth, SGLT proteins can be overexpressed, purified, and reconstituted in liposomes for biochemical and functional studies. Seventh, SGLTs belong to a structural family of transporters in different gene families with common transport mechanisms. Eighth, the x-ray structure of vSGLT, and related Na^+ cotransporters, has begun to allow us to explain Na^+ /sugar cotransport at an atomic level. Ninth, the SGLTs are now drug targets for the treatment of chronic diseases, e.g., SGLT2 inhibitors to control blood glucose in diabetes.

XVI. UNRESOLVED PROBLEMS

Starting with our need to integrate structure and function, we must obtain high-resolution structures of human SGLTs to 1) identify the second Na^+ binding site in those transporters where the Na^+ /sugar coupling coefficient is 2. This together with being able to parse out the kinetics of Na^+ binding to each site will enable one to understand both the fast transporter kinetics, a major limitation with existing models, and how Na^+ binding alters transporter structure. 2) We must identify the origin of the “gating charge” of these transporters and unlock the origin of the voltage dependence of sugar transport. 3) We must determine the structure in different conformation states, e.g., Na^+ free, Na^+ bound, and inhibitor bound. This will provide more frames in the movie to understand the whole catalytic cycle. 4) We must resolve the structure of SGLTs with high-affinity inhibitors bound. This may explain the selectivity differences between SGLT1 and SGLT2 inhibitors. 5) We must identify differences in structure between hSGLT1 and hSGLT3 to let us know why hSGLT3 is a glucose sensor and not a glucose transporter. In addition, this may identify the gate that prevents sugar exit to the cytoplasm in hSGLT3 and the link coupling sugar and Na^+ in SGLT1. 6) High-resolution structures will indentify the pathway for water and urea through the transporters.

The second challenge is to understand substrate specificity, kinetics, and function of the poorly understood SGLT4 and SGLT5 given the hints we already have about their unique sugar specificity and/or expression profile. There is also a need to clarify the regulation of expression and function of alternatively spliced variants.

A third challenge is the physiology of SGLTs in diverse locations throughout the body. For example, 1) in the brain we need to determine why SGLTs are functionally expressed in the hippocampus, cerebral cortex, and hypothalamus (258). Surely it is not to provide glucose to neurons as they are amply endowed with GLUTs. Are the SGLTs acting as glucose sensors or water channels in these cells of the brain? 2) There are large gaps in our understanding of the mechanism of milk secretion in the lactating mammary gland. Are the SGLTs expressed in the gland on the basolateral membrane to provide glucose and galactose for lactose synthesis, or are the SGLTs important for water secretion? 3) Similar questions arise about the role of SGLTs in glucose secretion and absorption in salivary glands and interhepatic bile ducts. 4) What is the significance of reported SGLT gene expression in the heart, lung, muscle, testis, ovary, pancreas, and prostate? These questions are not just of physiological significance but are of vital interest in the pathophysiology of glucose homeostasis and the upcoming introduction of SGLT2 inhibitors to control blood glucose levels in diabetics.

It seems to us that we have just addressed the tip of the iceberg about the biology of human SGLTs, and we look forward to the entry of new investigators into this field.

NOTE ADDED IN PROOF

Further insight into the transport mechanism comes from our recent study using molecular dynamics, biochemistry, and a second crystal structure of vSGLT (238). In essence, it is postulated that the conformational change responsible for the transition from the outward to inward occluded states (C3 to C4) is a rigid body movement where the “hash” (TM3, 4, 8, and 9) and “sugar” bundles (TM 2, 6, and 7) rotate by 3° in the opposite direction. This results in a displacement of TM8 by 4 Å, and along with 13° kink in the inner half of TM1, that loosens the Na₂ site such that Na^+ leaves to the cytoplasm within 9 ns. This exit causes a disruption in the H-bond between Try-263 and Asn-64 permitting the Try-263 side chain to assume a transient rotamer position within 50–100 ns allowing sugar to escape into the internal hydrophilic vestibule. Moreover, the rigid body movements of the hash and sugar bundles increase the volume of the vestibule by 1,400 Å³, allowing free exit of the sugar to the cytoplasm.

ACKNOWLEDGMENTS

Virtually all of the advances we have made in understanding SGLT were done in the Department of Physiology at UCLA as a result of collaborative efforts by a team of talented people. We are indebted to those students, fellows, and colleagues in the team for their creative hard work. We also gratefully acknowledge the continuing collaborations with Jeff Abramson and his group on the structure of SGLTs, and with colleagues in other departments at UCLA, particularly Jorge Barrio in Medical and Molecular Pharmacology, Martin Martin in Pediatrics, and Guido Zampighi in Neurobiology. Thanks also to Thomas Zeuthen of the University of Copenhagen for his insights into water transport. We are thankful to Charles Hummel for his critical comments and to Wendy Ravenhill for drawing many of the figures and her assistance in preparing the manuscript.

This work is in honor of R. K. Crane, 12/20/1919–11/31/2010.

Address for reprint requests and other correspondence: E. M. Wright, Dept. of Physiology, David Geffen School of Medicine at UCLA, 10833 LeConte Ave., Los Angeles, CA 90095-1751 (e-mail: ewright@mednet.ucla.edu).

GRANTS

This work has been supported by various grants from the National Institutes of Health (National Institute of Diabetes and Digestive and Kidney Diseases) over the past 30 years, including DK-19567.

DISCLOSURES

No conflicts of interest, financial or otherwise, are declared by the authors.

REFERENCES

1. Abramson J, Wright EM. Structure and function of Na^+ -symporters with inverted repeats. *Curr Opin Struct Biol* 19: 425–432, 2009.
2. Alvarado F, Crane RK. Studies on the mechanism of intestinal absorption of sugars. VII. Phenylglycoside transport and its possible relationship to phlorizin inhibition of the active transport of sugars by the small intestine. *Biochim Biophys Acta* 93: 116–135, 1964.
3. Aouameur R, Da Cal S, Bissonnette P, Coady MJ, Lapointe JY. SMIT2 mediates all myo-inositol uptake in apical membranes of rat small intestine. *Am J Physiol Gastrointest Liver Physiol* 293: G1300–G1307, 2007.
4. Balen D, Ljubojevic M, Breljak D, Brzica H, Zlender V, Koepsell H, Sabolic I. Revised immunolocalization of the Na^+ -D-glucose cotransporter SGLT1 in rat organs with an improved antibody. *Am J Physiol Cell Physiol* 295: C475–C489, 2008.
5. Barfuss DW, Schafer JA. Differences in active and passive glucose transport along the proximal nephron. *Am J Physiol Renal Fluid Electrolyte Physiol* 241: F322–F332, 1981.
6. Barry RJ, Dikstein S, Matthews J, Smyth DH, Wright EM. Electrical potentials associated with intestinal sugar transfer. *J Physiol* 171: 316–338, 1964.
7. Bessell EM, Foster AB, Westwood JH. The use of deoxyfluorod-glucopyranoses and related compounds in a study of yeast hexokinase specificity. *Biochem J* 128: 199–204, 1972.
8. Bezanilla F, Perozo E, Papazian DM, Stefani E. Molecular basis of gating charge immobilization in Shaker potassium channels. *Science* 254: 679–683, 1991.
9. Bianchi L, Diez-Sampedro A. A single amino acid change converts the sugar sensor SGLT3 into a sugar transporter. *PLoS One* 5: e10241.
10. Birnir B, Lee HS, Hediger MA, Wright EM. Expression and characterization of the intestinal Na^+ /glucose cotransporter in COS-7 cells. *Biochim Biophys Acta* 1048: 100–104, 1990.
11. Birnir B, Loo DDF, Wright EM. Voltage-clamp studies of the Na^+ /glucose cotransporter cloned from rabbit small intestine. *Pflügers Arch* 418: 79–85, 1991.
12. Bormans GM, Van Oosterwyck G, De Groot TJ, Veyhl M, Mortelmans L, Verbrugge AM, Koepsell H. Synthesis and biologic evaluation of (11)c-methyl-D-glucoside, a tracer of the sodium-dependent glucose transporters. *J Nucl Med* 44: 1075–1081, 2003.
13. Calado J, Sznajer Y, Metzger D, Rita A, Hogan MC, Kattamis A, Scharf M, Tasic V, Greil J, Brinkert F, Kemper MJ, Santer R. Twenty-one additional cases of familial renal glucosuria: absence of genetic heterogeneity, high prevalence of private mutations and further evidence of volume depletion. *Nephrol Dial Transplant* 23: 3874–3879, 2008.
14. Casneuf VF, Fonteyne P, Van Damme N, Demetter P, Pauwels P, de Hemiptine B, De Vos M, Van de Wiele C, Peeters M. Expression of SGLT1, Bcl-2 and p53 in primary pancreatic cancer related to survival. *Cancer Invest* 26: 852–859, 2008.
15. Charron FM, Blanchard MG, Lapointe JY. Intracellular hypertonicity is responsible for water flux associated with Na^+ /glucose cotransport. *Biophys J* 90: 3546–3554, 2006.
16. Chasis H, Jolliffe N, Smith HW. The action of phlorizin on the excretion of glucose, xylose, sucrose, creatinine and urea by man. *J Clin Invest* 12: 1083–1090, 1933.
17. Chen XZ, Coady MJ, Jackson F, Berteloot A, Lapointe JY. Thermodynamic determination of the Na^+ :glucose coupling ratio for the human SGLT1 cotransporter. *Biophys J* 69: 2405–2414, 1995.
18. Chen XZ, Coady MJ, Lapointe JY. Fast voltage clamp discloses a new component of presteady-state currents from the Na^+ -glucose cotransporter. *Biophys J* 71: 2544–2552, 1996.
19. Chiorean EG, Dragovich T, Hamm J, Barrios CH, Gorini CF, Langmuir VK, Kroll S, Jung DT, Tidmarsh GT, Loehr PJ. A Phase 2 trial of glufosamide in combination with gemcitabine in chemotherapy-naïve pancreatic adenocarcinoma. *Am J Clin Oncol* 33: 111–116, 2010.
20. Choe S, Rosenberg JM, Abramson J, Wright EM, Grabe M. Water permeation through the sodium-dependent galactose cotransporter vSGLT. *Biophys J* 99: 56–58, 2010.
21. Coady MJ, Wallendorff B, Gagnon DG, Lapointe JY. Identification of a novel Na^+ /myo-inositol cotransporter. *J Biol Chem* 277: 35219–35224, 2002.
22. Cramer SC, Pardridge WM, Hirayama BA, Wright EM. Colocalization of GLUT2 glucose transporter, sodium/glucose cotransporter, and gamma-glutamyl transpeptidase in rat kidney with double-peroxidase immunocytochemistry. *Diabetes* 41: 766–770, 1992.
23. Crane RK, Miller D, Bihler I. The restrictions on possible mechanisms of intestinal active transport of sugars. In: *Membrane Transport and Metabolism*. Prague: Academic, 1960.
24. Crane RK. The gradient hypothesis and other models of carrier-mediated active transport. *Rev Physiol Biochem Pharmacol* 78: 99–159, 1977.
25. Crane RK. Questions. In: *Ion Gradient-Coupled Transport*, edited by Alvarado F, Van Os CH. New York: Elsevier, 1986, p. 431–438.
26. Crane RK. The road to ion-coupled membrane processes. In: *Comprehensive Biochemistry*, edited by Neuberger A, Van Deenen LLM, Semenza G. New York: Elsevier Science, 1983, p. 43–69.
27. Crane RK. Na^+ -dependent transport in the intestine and other annual tissues. *Federation, Proc* 24: 1000–1006, 1965.
28. Dahlin A, Royall J, Hohmann JG, Wang J. Expression profiling of the solute carrier gene family in the mouse brain. *J Pharmacol Exp Ther* 329: 558–570, 2009.
29. Dai G, Levy O, Carrasco N. Cloning and characterization of the thyroid iodide transporter. *Nature* 379: 458–460, 1996.
30. De Groot TJ, Veyhl M, Terwinghe C, Vanden Bempt V, Dupont P, Mortelmans L, Verbrugge AM, Bormans GM, Koepsell H. Synthesis of ^{18}F -fluoroalkyl-beta-D-glucosides and their evaluation as tracers for sodium-dependent glucose transporters. *J Nucl Med* 44: 1973–1981, 2003.

31. Debnam ES, Levin RJ. An experimental method of identifying and quantifying the active transfer electrogenic component from the diffusive component during sugar absorption measured in vivo. *J Physiol* 246: 181–196, 1975.
32. Diedrich DF. The comparative effects of some phlorizin analogs on the renal reabsorption of glucose. *Biochim Biophys Acta* 71: 688–700, 1963.
33. Diez-Sampedro A. Involvement of amino acid 36 in TM1 in voltage sensitivity in mouse Na^+ /glucose cotransporter SGLT1. *J Membr Biol* 227: 57–66, 2009.
34. Diez-Sampedro A, Eskandari S, Wright EM, Hirayama BA. Na^+ -to-sugar stoichiometry of SGLT3. *Am J Physiol Renal Physiol* 280: F278–F282, 2001.
35. Diez-Sampedro A, Hirayama BA, Osswald C, Gorboulev V, Baumgarten K, Volk C, Wright EM, Koepsell H. A glucose sensor hiding in a family of transporters. *Proc Natl Acad Sci USA* 100: 11753–11758, 2003.
36. Diez-Sampedro A, Loo DDF, Wright EM, Zampighi GA, Hirayama BA. Coupled sodium/glucose cotransport by SGLT1 requires a negative charge at position 454. *Biochemistry* 43: 13175–13184, 2004.
37. Diez-Sampedro A, Lostao MP, Wright EM, Hirayama BA. Glycoside binding and translocation in Na^+ -dependent glucose cotransporters: comparison of SGLT1 and SGLT3. *J Membr Biol* 176: 111–117, 2000.
38. Diez-Sampedro A, Wright EM, Hirayama BA. Residue 457 controls sugar binding and transport in the Na^+ /glucose cotransporter. *J Biol Chem* 276: 49188–49194, 2001.
39. Dunham I, Shimizu N, Roe BA, Chissoe S, Hunt AR, Collins JE, Bruskiewich R, Beare DM, Clamp M, Smink LJ, Ainscough R, Almeida JP, Babbage A, Bagguley C, Bailey J, Barlow K, Bates KN, Beasley O, Bird CP, Blakey S, Bridgeman AM, Buck D, Burgess J, Burrill WD, O'Brien KP. The DNA sequence of human chromosome 22. *Nature* 402: 489–495, 1999.
40. Dyer J, Daly K, Salmon KS, Arora DK, Kokashvili Z, Margolskee RF, Shirazi-Beechey SP. Intestinal glucose sensing and regulation of intestinal glucose absorption. *Biochem Soc Trans* 35: 1191–1194, 2007.
41. Dyer J, Vayro S, King TP, Shirazi-Beechey SP. Glucose sensing in the intestinal epithelium. *Eur J Biochem* 270: 3377–3388, 2003.
42. Dyer J, Vayro S, Shirazi-Beechey SP. Mechanism of glucose sensing in the small intestine. *Biochem Soc Trans* 31: 1140–1142, 2003.
43. Dyer J, Wood IS, Palejwala A, Ellis A, Shirazi-Beechey SP. Expression of monosaccharide transporters in intestine of diabetic humans. *Am J Physiol Gastrointest Liver Physiol* 282: G241–G248, 2002.
44. Ehrenkranz JR, Lewis NG, Kahn CR, Roth J. Phlorizin: a review. *Diabetes Metab Res Rev* 21: 31–38, 2005.
45. Elfeber K, Kohler A, Lutzenburg M, Osswald C, Galla HJ, Witte OW, Koepsell H. Localization of the Na^+ -D-glucose cotransporter SGLT1 in the blood-brain barrier. *Histochem Cell Biol* 121: 201–207, 2004.
46. Eskandari S, Wright EM, Kreman M, Starace DM, Zampighi GA. Structural analysis of cloned plasma membrane proteins by freeze-fracture electron microscopy. *Proc Natl Acad Sci USA* 95: 11235–11240, 1998.
47. Eskandari S, Wright EM, Loo DDF. Kinetics of the reverse mode of the Na^+ /glucose cotransporter. *J Membr Biol* 204: 23–32, 2005.
48. Faham S, Watanabe A, Besserer GM, Cascio D, Specht A, Hirayama BA, Wright EM, Abramson J. The crystal structure of a sodium galactose transporter reveals mechanistic insights into Na^+ /sugar symport. *Science* 321: 810–814, 2008.
49. Falk S, Guay A, Chenu C, Patil SD, Berteloot A. Reduction of an eight-state mechanism of cotransport to a six-state model using a new computer program. *Biophys J* 74: 816–830, 1998.
50. Fang Y, Jayaram H, Shane T, Kolmakova-Partensky L, Wu F, Williams C, Xiong Y, Miller C. Structure of a prokaryotic virtual proton pump at 3.2 Å resolution. *Nature* 460: 1040–1043, 2009.
51. Ferrannini E, Jimenez Ramos S, Salsali A, Tang W, List JF. Dapagliflozin monotherapy in type 2 diabetic patients with inadequate glycemic control by diet and exercise: a randomized, double-blind, placebo-controlled, phase III trial. *Diabetes Care*. In press.
52. Fuhrmann GF, Dernedde S, Frenking G. Phloretin keto-enol tautomerism and inhibition of glucose transport in human erythrocytes (including effects of phloretin on anion transport). *Biochim Biophys Acta* 1110: 105–111, 1992.
53. Gagnon DG, Holt A, Bourgeois F, Wallendorff B, Coady MJ, Lapointe JY. Membrane topology of loop 13–14 of the Na^+ /glucose cotransporter (SGLT1): a SCAM and fluorescent labelling study. *Biochim Biophys Acta* 1712: 173–184, 2005.
54. Gao X, Lu F, Zhou L, Dang S, Sun L, Li X, Wang J, Shi Y. Structure and mechanism of an amino acid antiporter. *Science* 324: 1565–1568, 2009.
55. Gok F, Aydin HI, Kurt I, Gokcay E, Maeda M, Kasahara M. A novel mutation of Na^+ /glucose cotransporter in a Turkish newborn with congenital glucose-galactose malabsorption. *J Pediatr Gastroenterol Nutr* 40: 508–511, 2005.
56. Gonzalez JA, Reimann F, Burdakov D. Dissociation between sensing and metabolism of glucose in sugar sensing neurones. *J Physiol* 587: 41–48, 2009.
57. Griddle FM, Williams L, Simpson AK, Reimann F. A novel glucose-sensing mechanism contributing to glucagon-like peptide-1 secretion from the GLUTag cell line. *Diabetes* 52: 1147–1154, 2003.
58. Hager K, Hazama A, Kwon HM, Loo DDF, Handler JS, Wright EM. Kinetics and specificity of the renal Na^+ /myo-inositol cotransporter expressed in *Xenopus* oocytes. *J Membr Biol* 143: 103–113, 1995.
59. Hazama A, Loo DDF, Wright EM. Presteady-state currents of the rabbit Na^+ /glucose cotransporter (SGLT1). *J Membr Biol* 155: 175–186, 1997.
60. Hediger MA, Budarf ML, Emanuel BS, Mohandas TK, Wright EM. Assignment of the human intestinal Na^+ /glucose cotransporter gene (SGLT1) to the q11.2-qter region of chromosome 22. *Genomics* 4: 297–300, 1989.
61. Hediger MA, Coady MJ, Ikeda TS, Wright EM. Expression cloning and cDNA sequencing of the Na^+ /glucose co-transporter. *Nature* 330: 379–381, 1987.
62. Hediger MA, Ikeda T, Coady M, Gundersen CB, Wright EM. Expression of size-selected mRNA encoding the intestinal Na⁺/glucose cotransporter in *Xenopus laevis* oocytes. *Proc Natl Acad Sci USA* 84: 2634–2637, 1987.
63. Hediger MA, Mendlein J, Lee HS, Wright EM. Biosynthesis of the cloned intestinal Na^+ /glucose cotransporter. *Biochim Biophys Acta* 1064: 360–364, 1991.
64. Hediger MA, Turk E, Wright EM. Homology of the human intestinal Na^+ /glucose and *Escherichia coli* Na^+ /proline cotransporters. *Proc Natl Acad Sci USA* 86: 5748–5752, 1989.
65. Helmke BM, Reisser C, Idzko M, Dyckhoff G, Herold-Mende C. Expression of SGLT-1 in preneoplastic and neoplastic lesions of the head and neck. *Oral Oncol* 40: 28–35, 2004.
66. Hirayama BA, Diez-Sampedro A, Wright EM. Common mechanisms of inhibition for the Na^+ /glucose (hSGLT1) and Na^+/Cl^- /GABA (hGAT1) cotransporters. *Br J Pharmacol* 134: 484–495, 2001.
67. Hirayama BA, Loo DDF, Diez-Sampedro A, Leung DW, Meinild AK, Lai-Bing M, Turk E, Wright EM. Sodium-dependent reorganization of the sugar-binding site of SGLT1. *Biochemistry* 46: 13391–13406, 2007.
68. Hirayama BA, Loo DDF, Wright EM. Cation effects on protein conformation and transport in the Na^+ /glucose cotransporter. *J Biol Chem* 272: 2110–2115, 1997.
69. Hirayama BA, Lostao MP, Panayotova-Heiermann M, Loo DD, Turk E, Wright EM. Kinetic and specificity differences between rat, human, and rabbit Na^+ -glucose cotransporters (SGLT-1). *Am J Physiol Gastrointest Liver Physiol* 270: G919–G926, 1996.
70. Hirayama BA, Wong HC, Smith CD, Hagenbuch BA, Hediger MA, Wright EM. Intestinal and renal Na^+ /glucose cotransporters share common structures. *Am J Physiol Cell Physiol* 261: C296–C304, 1991.
71. Hirayama BA, Wright EM. Glycosylation of the rabbit intestinal brush border Na^+ /glucose cotransporter. *Biochim Biophys Acta* 1103: 37–44, 1992.
72. Hirsch JR, Loo DDF, Wright EM. Regulation of Na^+ /glucose cotransporter expression by protein kinases in *Xenopus laevis* oocytes. *J Biol Chem* 271: 14740–14746, 1996.

73. Hirschhorn N, Greenough WB 3rd. Progress in oral rehydration therapy. *Sci Am* 264: 50–56, 1991.
74. Hirschhorn N, Kinzie JL, Sachar DB, Northrup RS, Taylor JO, Ahmad SZ, Phillips RA. Decrease in net stool output in cholera during intestinal perfusion with glucose-containing solutions. *N Engl J Med* 279: 176–181, 1968.
75. Hopfer U. Membrane transport mechanisms for hexoses and amino acids in the small intestine. In: *Physiology of the Gastrointestinal Tract* (2nd ed.), edited by Johnson LR, Christensen J, Jackson MJ, Jacobson ED, Walsh JH. New York: Raven, 1987, p. 1499–1526.
76. Hopfer U, Nelson K, Perrotto J, Isselbacher KJ. Glucose transport in isolated brush border membrane from rat small intestine. *J Biol Chem* 248: 25–32, 1973.
77. Horiba N, Masuda S, Ohnishi C, Takeuchi D, Okuda M, Inui K. Na⁺-dependent fructose transport via rNaGLT1 in rat kidney. *FEBS Lett* 546: 276–280, 2003.
78. Horiba N, Masuda S, Takeuchi A, Takeuchi D, Okuda M, Inui K. Cloning and characterization of a novel Na⁺-dependent glucose transporter (NaGLT1) in rat kidney. *J Biol Chem* 278: 14669–14676, 2003.
79. Hosang M, Gibbs EM, Diederich DF, Semenza G. Photoaffinity labeling and identification of (a component of) the small-intestinal Na⁺,D-glucose transporter using 4-azidophlorizin. *FEBS Lett* 130: 244–248, 1981.
80. Huang SC, Truong D, Wu HM, Chatzioannou AF, Shao W, Wu AM, Phelps ME. An internet-based “kinetic imaging system” (KIS) for MicroPET. *Mol Imaging Biol* 7: 330–341, 2005.
81. Hummel C, Lu C, Loo DDF, Hirayama BA, Voss AA, Wright EM. Glucose transport by human renal Na⁺/D-glucose cotransporters SGLT1 and SGLT2. *Am J Physiol Cell Physiol* 300: C14–C21, 2011.
82. Ikeda TS, Hwang ES, Coady MJ, Hirayama BA, Hediger MA, Wright EM. Characterization of a Na⁺/glucose cotransporter cloned from rabbit small intestine. *J Membr Biol* 110: 87–95, 1989.
83. Isaji M. Sodium-glucose cotransporter inhibitors for diabetes. *Curr Opin Invest Drugs* 8: 285–292, 2007.
84. Ishikawa N, Oguri T, Isobe T, Fujitaka K, Kohno N. SGLT gene expression in primary lung cancers and their metastatic lesions. *Jpn J Cancer Res* 92: 874–879, 2001.
85. Kaback HR, Stadtman ER. Proline uptake by an isolated cytoplasmic membrane preparation of *Escherichia coli*. *Proc Natl Acad Sci USA* 55: 920–927, 1966.
86. Kanai Y, Lee WS, You G, Brown D, Hediger MA. The human kidney low affinity Na⁺/glucose cotransporter SGLT2. Delineation of the major renal reabsorptive mechanism for D-glucose. *J Clin Invest* 93: 397–404, 1994.
87. Kasahara M, Maeda M, Hayashi S, Mori Y, Abe T. A missense mutation in the Na⁺/glucose cotransporter gene SGLT1 in a patient with congenital glucose-galactose malabsorption: normal trafficking but inactivation of the mutant protein. *Biochim Biophys Acta* 1536: 141–147, 2001.
88. Katsuno K, Fujimori Y, Takemura Y, Hiratomi M, Itoh F, Komatsu Y, Fujiwara H, Isaji M. Serglyllofloxin, a novel selective inhibitor of low-affinity sodium glucose cotransporter (SGLT2), validates the critical role of SGLT2 in renal glucose reabsorption and modulates plasma glucose level. *J Pharmacol Exp Ther* 320: 323–330, 2007.
89. Kellett GL, Brot-Laroche E. Apical GLUT2: a major pathway of intestinal sugar absorption. *Diabetes* 54: 3056–3062, 2005.
90. Kellett GL, Helliwell PA. The diffusive component of intestinal glucose absorption is mediated by the glucose-induced recruitment of GLUT2 to the brush-border membrane. *Biochem J* 350: 155–162, 2000.
91. Kessler M, Semenza G. The small-intestinal Na⁺,D-glucose cotransporter: an asymmetric gated channel (or pore) responsive to delta psi. *J Membr Biol* 76: 27–56, 1983.
92. Kimmich GA. Intestinal absorption of sugar. In: *Physiology of the Gastrointestinal Tract*, edited by Johnson LR, Christensen J, Grossman MI, Jacobson ED, Schultz SG. New York: Raven, 1981, p. 1035–1061.
93. Kimmich GA, Randles J. Sodium-sugar coupling stoichiometry in chick intestinal cells. *Am J Physiol Cell Physiol* 247: C74–C82, 1984.
94. Kleinzelerr AKA. *Membrane Transport and Metabolism*. Praha: Publishing House of the Czechoslovak Academy of Sciences, 1961, p. 608.
95. Komoroski B, Vachharajani N, Boulton D, Kornhauser D, Geroldes M, Li L, Pfister M. Dapagliflozin, a novel SGLT2 inhibitor, induces dose-dependent glucosuria in healthy subjects. *Clin Pharmacol Ther* 85: 520–526, 2009.
96. Komoroski B, Vachharajani N, Feng Y, Li L, Kornhauser D, Pfister M. Dapagliflozin, a novel, selective SGLT2 inhibitor, improved glycemic control over 2 weeks in patients with type 2 diabetes mellitus. *Clin Pharmacol Ther* 85: 513–519, 2009.
97. Kopito RR, Lodish HF. Primary structure and transmembrane orientation of the murine anion exchange protein. *Nature* 316: 234–238, 1985.
98. Korn T, Kuhlmann T, Track C, Schatz I, Baumgarten K, Gorboulev V, Koepsell H. The plasma membrane-associated protein RS1 decreases transcription of the transporter SGLT1 in confluent LLC-PK₁ cells. *J Biol Chem* 276: 45330–45340, 2001.
99. Krofchick D, Huntley SA, Silverman M. Transition states of the high-affinity rabbit Na⁺/glucose cotransporter SGLT1 as determined from measurement and analysis of voltage-dependent charge movements. *Am J Physiol Cell Physiol* 287: C46–C54, 2004.
100. Krofchick D, Silverman M. Investigating the conformational states of the rabbit Na⁺/glucose cotransporter. *Biophys J* 84: 3690–3702, 2003.
101. Kroiss M, Leyrer M, Gorboulev V, Kuhlmann T, Kipp H, Koepsell H. Transporter regulator RS1 (RSC1A1) coats the trans-Golgi network and migrates into the nucleus. *Am J Physiol Renal Physiol* 291: F1201–F1212, 2006.
102. Kumar A, Tyagi NK, Arevalo E, Miller KW, Kinne RK. A proteomic study of sodium/D-glucose cotransporter 1 (SGLT1): topology of loop 13 and coverage of other functionally important domains. *Biochim Biophys Acta* 1774: 968–974, 2007.
103. Kunze WA, Furness JB. The enteric nervous system and regulation of intestinal motility. *Annu Rev Physiol* 61: 117–142, 1999.
104. Kwon HM, Yamauchi A, Uchida S, Preston AS, Garcia-Perez A, Burg MB, Handler JS. Cloning of the cDNA for a Na⁺/myo-inositol cotransporter, a hypertonicity stress protein. *J Biol Chem* 267: 6297–6301, 1992.
105. Lam JT, Martin MG, Turk E, Hirayama BA, Bosshard NU, Steinmann B, Wright EM. Missense mutations in SGLT1 cause glucose-galactose malabsorption by trafficking defects. *Biochim Biophys Acta* 1453: 297–303, 1999.
106. Lambotte S, Veyhl M, Kohler M, Morrison-Shetlar AI, Kinne RK, Schmid M, Koepsell H. The human gene of a protein that modifies Na⁺-D-glucose co-transport. *DNA Cell Biol* 15: 769–777, 1996.
107. Landau BR, Bernstein L, Wilson TH. Hexose transport by hamster intestine in vitro. *Am J Physiol* 203: 237–240, 1962.
108. Laplane R, Polonovski C, Etienne M, Debray P, Lods JC, Pissarro B. L'intolerance aux sucres a un transfert intestinal actif. *Arch Pr Pediatr* 19: 895–944, 1962.
109. Lapointe JY. Response to Zeuthen and Zeuthen's comment to the editor: enough local hypertonicity is enough. *Biophys J* 93: 1417–1419, 2007.
110. Lauger P, Jauch P. Microscopic description of voltage effects on ion-driven cotransport systems. *J Membr Biol* 91: 275–284, 1986.
111. Lazaridis KN, Pham L, Vroman B, de Groen PC, LaRusso NF. Kinetic and molecular identification of sodium-dependent glucose transporter in normal rat cholangiocytes. *Am J Physiol Gastrointest Liver Physiol* 272: G1168–G1174, 1997.
112. Le Coutre J, Turk E, Kaback HR, Wright EM. Ligand-induced differences in secondary structure of the *Vibrio parahaemolyticus* Na⁺/galactose cotransporter. *Biochemistry* 41: 8082–8086, 2002.
113. Leicht S, Grohmann S, Page K, Streicher R, Mark M, Eichelmann P. hSGLT5 (SLC5A10) is a sodium-dependent sugar transporter exclusively expressed in the kidney. *Am Diabetes Assoc* 66: 1512-P, 2006.
114. Lescale-Matys L, Dyer J, Scott D, Freeman TC, Wright EM, Shirazi-Beechey SP. Regulation of the ovine intestinal Na⁺/glu-

- cose co-transporter (SGLT1) is dissociated from mRNA abundance. *Biochem J* 291: 435–440, 1993.
115. Leung DW, Loo DDF, Hirayama BA, Zeuthen T, Wright EM. Urea transport by cotransporters. *J Physiol* 528: 251–257, 2000.
 116. Leung DW, Turk E, Kim O, Wright EM. Functional expression of the *Vibrio parahaemolyticus* Na⁺/galactose (vSGLT) cotransporter in *Xenopus laevis* oocytes. *J Membr Biol* 187: 65–70, 2002.
 117. Li J, Tajkhorshid E. Ion-releasing state of a secondary membrane transporter. *Biophys J* 97: 29–31, 2009.
 118. Lin X, Ma L, Fitzgerald RL, Ostlund RE Jr. Human sodium/inositol cotransporter 2 (SMIT2) transports inositol but not glucose in L6 cells. *Arch Biochem Biophys* 481: 197–201, 2009.
 119. Lindquist B, Meeuwisse GW. Chronic diarrhoea caused by monosaccharide malabsorption. *Acta Paediatr* 51: 674–685, 1962.
 120. List JF, Woo V, Morales E, Tang W, Fiedorek FT. Sodium-glucose cotransport inhibition with dapagliflozin in type 2 diabetes. *Diabetes Care* 32: 650–657, 2009.
 121. Liu M, Seino S, Kirchgessner AL. Identification and characterization of glucosensitive neurons in the enteric nervous system. *J Neurosci* 19: 10305–10317, 1999.
 122. Liu T, Speight P, Silverman M. Reanalysis of structure/function correlations in the region of transmembrane segments 4 and 5 of the rabbit sodium/glucose cotransporter. *Biochem Biophys Res Commun* 378: 133–138, 2009.
 123. Lo B, Silverman M. Cysteine scanning mutagenesis of the segment between putative transmembrane helices IV and V of the high affinity Na⁺/glucose cotransporter SGLT1. Evidence that this region participates in the Na⁺ and voltage dependence of the transporter. *J Biol Chem* 273: 29341–29351, 1998.
 124. Loike JD, Hickman S, Kuang K, Xu M, Cao L, Vera JC, Silverstein SC, Fischberg J. Sodium-glucose cotransporters display sodium- and phlorizin-dependent water permeability. *Am J Physiol Cell Physiol* 271: C1774–C1779, 1996.
 125. Loo DDF, Hirayama BA, Sala-Rabanal M, Wright EM. How drugs interact with transporters: SGLT1 as a model. *J Membr Biol* 223: 87–106, 2008.
 126. Loo DDF, Eskandari S, Boorer KJ, Sarkar HK, Wright EM. Role of Cl⁻ in electrogenic Na⁺-coupled cotransporters GAT1 and SGLT1. *J Biol Chem* 275: 37414–37422, 2000.
 127. Loo DDF, Hazama A, Supplisson S, Turk E, Wright EM. Relaxation kinetics of the Na⁺/glucose cotransporter. *Proc Natl Acad Sci USA* 90: 5767–5771, 1993.
 128. Loo DDF, Hirayama BA, Cha A, Bezanilla F, Wright EM. Perturbation analysis of the voltage-sensitive conformational changes of the Na⁺/glucose cotransporter. *J Gen Physiol* 125: 13–36, 2005.
 129. Loo DDF, Hirayama BA, Gallardo EM, Lam JT, Turk E, Wright EM. Conformational changes couple Na⁺ and glucose transport. *Proc Natl Acad Sci USA* 95: 7789–7794, 1998.
 130. Loo DDF, Hirayama BA, Karakossian MH, Meinild AK, Wright EM. Conformational dynamics of hSGLT1 during Na⁺/glucose cotransport. *J Gen Physiol* 128: 701–720, 2006.
 131. Loo DDF, Hirayama BA, Meinild AK, Chandy G, Zeuthen T, Wright EM. Passive water and ion transport by cotransporters. *J Physiol* 518: 195–202, 1999.
 132. Loo DDF, Hirayama BA, Sala-Rabanal M, Wright EM. How drugs interact with transporters: SGLT1 as a model. *J Membr Biol* 223: 87–106, 2008.
 133. Loo DDF, Wright EM, Zeuthen T. Water pumps. *J Physiol* 542: 53–60, 2002.
 134. Loo DDF, Zeuthen T, Chandy G, Wright EM. Cotransport of water by the Na⁺/glucose cotransporter. *Proc Natl Acad Sci USA* 93: 13367–13370, 1996.
 135. Loo DDF, Hirayama BA, Karakossian MH, Meinild AK, Wright EM. Conformational dynamics of hSGLT1 during Na⁺/glucose cotransport. *J Gen Physiol* 128: 701–720, 2006.
 136. Lostao MP, Hirayama BA, Loo DDF, Wright EM. Phenylglucosides and the Na⁺/glucose cotransporter (SGLT1): analysis of interactions. *J Membr Biol* 142: 161–170, 1994.
 137. Lostao MP, Hirayama BA, Panayotova-Heiermann M, Sampogna SL, Bok D, Wright EM. Arginine-427 in the Na⁺/glucose cotransporter (SGLT1) is involved in trafficking to the plasma membrane. *FEBS Lett* 377: 181–184, 1995.
 138. Mackenzie B, Loo DDF, Panayotova-Heiermann M, Wright EM. Biophysical characteristics of the pig kidney Na⁺/glucose cotransporter SGLT2 reveal a common mechanism for SGLT1 and SGLT2. *J Biol Chem* 271: 32678–32683, 1996.
 139. Mackenzie B, Loo DDF, Wright EM. Relationships between Na⁺/glucose cotransporter (SGLT1) currents and fluxes. *J Membr Biol* 162: 101–106, 1998.
 140. Martin MG, Lostao MP, Turk E, Lam J, Kreman M, Wright EM. Compound missense mutations in the sodium/d-glucose cotransporter result in trafficking defects. *Gastroenterology* 112: 1206–1212, 1997.
 141. Martin MG, Turk E, Kerner C, Zabel B, Wirth S, Wright EM. Prenatal identification of a heterozygous status in two fetuses at risk for glucose-galactose malabsorption. *Prenat Diagn* 16: 458–462, 1996.
 142. Martin MG, Turk E, Lostao MP, Kerner C, Wright EM. Defects in Na⁺/glucose cotransporter (SGLT1) trafficking and function cause glucose-galactose malabsorption. *Nat Genet* 12: 216–220, 1996.
 143. Martin MG, Wang J, Solorzano-Vargas RS, Lam JT, Turk E, Wright EM. Regulation of the human Na⁺-glucose cotransporter gene, SGLT1, by HNF-1 and Sp1. *Am J Physiol Gastrointest Liver Physiol* 278: G591–G603, 2000.
 144. Masuyuk AI, Masuyuk TV, Tietz PS, Splinter PL, LaRusso NF. Intrahepatic bile ducts transport water in response to absorbed glucose. *Am J Physiol Cell Physiol* 283: C785–C791, 2002.
 145. Meinild A, Klaerke DA, Loo DDF, Wright EM, Zeuthen T. The human Na⁺-glucose cotransporter is a molecular water pump. *J Physiol* 508: 15–21, 1998.
 146. Meinild AK, Hirayama BA, Wright EM, Loo DDF. Fluorescence studies of ligand-induced conformational changes of the Na⁺/glucose cotransporter. *Biochemistry* 41: 1250–1258, 2002.
 147. Meng W, Ellsworth BA, Nirschl AA, McCann PJ, Patel M, Girotra RN, Wu G, Sher PM, Morrison EP, Biller SA, Zahler R, Deshpande PP, Pullockaran A, Hagan DL, Morgan N, Taylor JR, Obermeier MT, Humphreys WG, Khanna A, Disenza L, Robertson JG, Wang A, Han S, Wetterau JR, Janovitz EB, Flint OP, Whaley JM, Washburn WN. Discovery of dapagliflozin: a potent, selective renal sodium-dependent glucose cotransporter 2 (SGLT2) inhibitor for the treatment of type 2 diabetes. *J Med Chem* 51: 1145–1149, 2008.
 148. Mitchell P. Molecule, group and electron translocation through natural membrane. In: *The Structure of Function of the Membrane*, edited by Grant JK, Bell DJ. London: Biochemical Society, 1963, Symposium 22, p. 142–168.
 149. Mizuma T, Ohta K, Hayashi M, Awazu S. Intestinal active absorption of sugar-conjugated compounds by glucose transport system: implication of improvement of poorly absorbable drugs. *Biochem Pharmacol* 43: 2037–2039, 1992.
 150. Mueckler M, Caruso C, Baldwin SA, Panico M, Blench I, Morris HR, Allard WJ, Lienhard GE, Lodish HF. Sequence and structure of a human glucose transporter. *Science* 229: 941–945, 1985.
 151. Nishimura M, Naito S. Tissue-specific mRNA expression profiles of human ATP-binding cassette and solute carrier transporter superfamilies. *Drug Metab Pharmacokinet* 20: 452–477, 2005.
 152. Noskov SY, Roux B. Control of ion selectivity in LeuT: two Na⁺ binding sites with two different mechanisms. *J Mol Biol* 377: 804–818, 2008.
 153. O'Malley D, Reimann F, Simpson AK, Gribble FM. Sodium-coupled glucose cotransporters contribute to hypothalamic glucose sensing. *Diabetes* 55: 3381–3386, 2006.
 154. Obermeier S, Huselweh B, Tinel H, Kinne RH, Kunz C. Expression of glucose transporters in lactating human mammary gland epithelial cells. *Eur J Nutr* 39: 194–200, 2000.
 155. Oku A, Ueta K, Arakawa K, Ishihara T, Nawano M, Kuronuma Y, Matsumoto M, Saito A, Tsujihara K, Anai M, Asano T, Kanai Y, Endou H. T-1095, an inhibitor of renal Na⁺-glucose cotransporters, may provide a novel approach to treating diabetes. *Diabetes* 48: 1794–1800, 1999.
 156. Page MJ, Carrell CJ, Di Cera E. Engineering protein allostery: 1.05 Å resolution structure and enzymatic properties of a Na⁺-activated trypsin. *J Mol Biol* 378: 666–672, 2008.

158. **Page MJ, Di Cera E.** Role of Na^+ and K^+ in enzyme function. *Physiol Rev* 86: 1049–1092, 2006.
159. **Pajor AM, Randolph KM, Kerner SA, Smith CD.** Inhibitor binding in the human renal low- and high-affinity $\text{Na}^+/\text{glucose}$ cotransporters. *J Pharmacol Exp Ther* 324: 985–991, 2008.
160. **Palazzo M, Gariboldi S, Zanobbio L, Selleri S, Dusio GF, Mauro V, Rossini A, Balsari A, Rumio C.** Sodium-dependent glucose transporter-1 as a novel immunological player in the intestinal mucosa. *J Immunol* 181: 3126–3136, 2008.
161. **Panayotova-Heiermann M, Loo DDF, Kong CT, Lever JE, Wright EM.** Sugar binding to $\text{Na}^+/\text{glucose}$ cotransporters is determined by the carboxyl-terminal half of the protein. *J Biol Chem* 271: 10029–10034, 1996.
162. **Panayotova-Heiermann M, Loo DDF, Lam JT, Wright EM.** Neutralization of conservative charged transmembrane residues in the $\text{Na}^+/\text{glucose}$ cotransporter SGLT1. *Biochemistry* 37: 10522–10528, 1998.
163. **Panayotova-Heiermann M, Loo DDF, Lostao MP, Wright EM.** Sodium/d-glucose cotransporter charge movements involve polar residues. *J Biol Chem* 269: 21016–21020, 1994.
164. **Panayotova-Heiermann M, Loo DDF, Wright EM.** Kinetics of steady-state currents and charge movements associated with the rat $\text{Na}^+/\text{glucose}$ cotransporter. *J Biol Chem* 270: 27099–27105, 1995.
165. **Panayotova-Heiermann M, Wright EM.** Mapping the urea channel through the rabbit $\text{Na}^+/\text{glucose}$ cotransporter SGLT1. *J Physiol* 535: 419–425, 2001.
166. **Parent L, Supplisson S, Loo DDF, Wright EM.** Electrogenic properties of the cloned $\text{Na}^+/\text{glucose}$ cotransporter. I. Voltage-clamp studies. *J Membr Biol* 125: 49–62, 1992.
167. **Parent L, Supplisson S, Loo DDF, Wright EM.** Electrogenic properties of the cloned $\text{Na}^+/\text{glucose}$ cotransporter. II. A transport model under nonrapid equilibrium conditions. *J Membr Biol* 125: 63–79, 1992.
168. **Parent L, Wright EM.** Electrophysiology of the $\text{Na}^+/\text{glucose}$ cotransporter. *Soc Gen Physiol Ser* 48: 263–281, 1993.
169. **Peerce BE, Wright EM.** Conformational changes in the intestinal brush border sodium-glucose cotransporter labeled with fluorescein isothiocyanate. *Proc Natl Acad Sci USA* 81: 2223–2226, 1984.
170. **Phelps ME.** *PET Molecular Imaging and Its Biological Applications*. New York: Springer, 2004.
171. **Pierce NF, Banwell JG, Rupak DM, Mitra RC, Caranasos GJ, Keimowitz RI, Mondal A, Manji PM.** Effect of intragastric glucose-electrolyte infusion upon water and electrolyte balance in Asiatic cholera. *Gastroenterology* 55: 333–343, 1968.
172. **Pontoglio M, Prie D, Cheret C, Doyen A, Leroy C, Froguel P, Velho G, Yaniv M, Friedlander G.** HNF1alpha controls renal glucose reabsorption in mouse and man. *EMBO Rep* 1: 359–365, 2000.
173. **Poppe R, Karbach U, Gambaryan S, Wiesinger H, Lutzenburg M, Kraemer M, Witte OW, Koepsell H.** Expression of the $\text{Na}^+/\text{d-glucose}$ cotransporter SGLT1 in neurons. *J Neurochem* 69: 84–94, 1997.
174. **Prasad PD, Wang H, Kekuda R, Fujita T, Fei YJ, Devoe LD, Leibach FH, Ganapathy V.** Cloning and functional expression of a cDNA encoding a mammalian sodium-dependent vitamin transporter mediating the uptake of pantothenate, biotin, and lipoate. *J Biol Chem* 273: 7501–7506, 1998.
175. **Quick M, Loo DDF, Wright EM.** Neutralization of a conserved amino acid residue in the human $\text{Na}^+/\text{glucose}$ transporter (hSGLT1) generates a glucose-gated H^+ channel. *J Biol Chem* 276: 1728–1734, 2001.
176. **Quick M, Tomasevic J, Wright EM.** Functional asymmetry of the human $\text{Na}^+/\text{glucose}$ transporter (hSGLT1) in bacterial membrane vesicles. *Biochemistry* 42: 9147–9152, 2003.
177. **Quick M, Wright EM.** Employing *Escherichia coli* to functionally express, purify, and characterize a human transporter. *Proc Natl Acad Sci USA* 99: 8597–8601, 2002.
178. **Quiocho FA.** Protein-carbohydrate interactions: basic molecular features. *Pure Appl Chem* 61: 1293–1306, 1989.
179. **Rao MC.** Oral rehydration therapy: new explanations for an old remedy. *Annu Rev Physiol* 66: 385–417, 2004.
180. **Raybould HE.** Visceral perception: sensory transduction in visceral afferents and nutrients. *Gut* 51 Suppl 1: i11–i14, 2002.
181. **Raybould HE, Zittel TT.** Inhibition of gastric motility induced by intestinal glucose in awake rats: role of $\text{Na}^+/\text{glucose}$ co-transporter. *Neurogastroenterol Motil* 7: 9–14, 1995.
182. **Reinhardt J, Veyhl M, Wagner K, Gambaryan S, Dekel C, Akhounova A, Korn T, Koepsell H.** Cloning and characterization of the transport modifier RS1 from rabbit which was previously assumed to be specific for $\text{Na}^+/\text{d-glucose}$ cotransport. *Biochim Biophys Acta* 1417: 131–143, 1999.
183. **Ressl S, Terwisscha van Scheltinga AC, Vonrhein C, Ott V, Ziegler C.** Molecular basis of transport and regulation in the $\text{Na}^+/\text{betaine}$ symporter BetP. *Nature* 458: 47–52, 2009.
184. **Robinson J.** *Moving Question: A History of Membrane Transport and Bioenergetics*. Bethesda, MD: Am. Physiol. Soc., 1997.
185. **Rossetti L, Smith D, Shulman GI, Papachristou D, DeFranzo RA.** Correction of hyperglycemia with phlorizin normalizes tissue sensitivity to insulin in diabetic rats. *J Clin Invest* 79: 1510–1515, 1987.
186. **Ruxin JN.** Magic bullet: the history of oral rehydration therapy. *Med Hist* 38: 363–397, 1994.
187. **Sabino-Silva R, Freitas HS, Lamers ML, Okamoto MM, Santos MF, Machado UF.** $\text{Na}^+/\text{glucose}$ cotransporter SGLT1 protein in salivary glands: potential involvement in the diabetes-induced decrease in salivary flow. *J Membr Biol* 228: 63–69, 2009.
188. **Sala-Rabanal M, Loo DDF, Hirayama BA, Turk E, Wright EM.** Molecular interactions between dipeptides, drugs and the human intestinal $\text{H}^+/\text{oligopeptide}$ cotransporter hPEPT1. *J Physiol* 574: 149–166, 2006.
189. **Santer R, Groth S, Kinner M, Dombrowski A, Berry GT, Brodehl J, Leonard JV, Moses S, Norgren S, Skovby F, Schneppenheim R, Steinmann B, Schaub J.** The mutation spectrum of the facilitative glucose transporter gene SLC2A2 (GLUT2) in patients with Fanconi-Bickel syndrome. *Hum Genet* 110: 21–29, 2002.
190. **Santer R, Kinner M, Lassen CL, Schneppenheim R, Eggert P, Bald M, Brodehl J, Daschner M, Ehrich JH, Kemper M, Li Volti S, Neuhaus T, Skovby F, Swift PG, Schaub J, Klaerke D.** Molecular analysis of the SGLT2 gene in patients with renal glucosuria. *J Am Soc Nephrol* 14: 2873–2882, 2003.
191. **Sauer GA, Nagel G, Koepsell H, Bamberg E, Hartung K.** Voltage and substrate dependence of the inverse transport mode of the rabbit $\text{Na}^+/\text{glucose}$ cotransporter (SGLT1). *FEBS Lett* 469: 98–100, 2000.
192. **Schmidt UM, Eddy B, Fraser CM, Venter JC, Semenza G.** Isolation of (a subunit of) the $\text{Na}^+/\text{d-glucose}$ cotransporter(s) of rabbit intestinal brush border membranes using monoclonal antibodies. *FEBS Lett* 161: 279–283, 1983.
193. **Schneider AJ, Kinter WB, Stirling CE.** Glucose-galactose malabsorption. Report of a case with autoradiographic studies of a mucosal biopsy. *N Engl J Med* 274: 305–312, 1966.
194. **Scholl-Burgi S, Santer R, Ehrich JH.** Long-term outcome of renal glucosuria type 0: the original patient and his natural history. *Nephrol Dial Transplant* 19: 2394–2396, 2004.
195. **Schultz SG.** Ion-coupled transport of organic solutes across biological membranes. In: *Physiology of Membrane Disorders*, edited by Andreoli TE, Hoffman JF, Fanestil DD. 1985, New York: Plenum, p. 283–294.
196. **Schultz SG, Curran PF.** Coupled transport of sodium and organic solutes. *Physiol Rev* 50: 637–718, 1970.
197. **Sharp PA, Debnam ES.** The role of cAMP in the control of sugar transport across the brush-border and basolateral membranes of rat jejunal enterocytes. *Exp Physiol* 79: 203–214, 1994.
198. **Shennan DB, Beechey RB.** Mechanisms involved in the uptake of d-glucose into the milk producing cells of rat mammary tissue. *Biochem Biophys Res Commun* 211: 986–990, 1995.
199. **Shimamura T, Weyand S, Beckstein O, Rutherford NG, Hadden JM, Sharples D, Sansom MS, Iwata S, Henderson PJ, Cameron AD.** Molecular basis of alternating access membrane transport by the sodium-hydantoin transporter Mhp1. *Science* 328: 470–473, 2010.
200. **Shimizu T, Okamoto I, Tamura K, Satoh T, Miyazaki M, Akashi Y, Ozaki T, Fukuoka M, Nakagawa K.** Phase I clinical and pharmacokinetic study of the glucose-conjugated cytotoxic

- agent D: -19575 (glufosfamide) in patients with solid tumors. *Cancer Chemother Pharmacol* 65: 243–250, 2010.
201. Shirazi-Beechey SP, Hirayama BA, Wang Y, Scott D, Smith MW, Wright EM. Ontogenetic development of lamb intestinal sodium-glucose co-transporter is regulated by diet. *J Physiol* 437: 699–708, 1991.
 202. Smith CD, Hirayama BA, Wright EM. Baculovirus-mediated expression of the Na⁺/glucose cotransporter in Sf9 cells. *Biochim Biophys Acta* 1104: 151–159, 1992.
 203. Soylu OB, Ecevit C, Altinoz S, Ozturk AA, Temizkan AK, Maeda M, Kasahara M. Nephrocalcinosis in glucose-galactose malabsorption: nephrocalcinosis and proximal tubular dysfunction in a young infant with a novel mutation of SGLT1. *Eur J Pediatr* 167: 1395–1398, 2008.
 204. Stefani E, Bezanilla F. Cut-open oocyte voltage-clamp technique. *Methods Enzymol* 293: 300–318, 1998.
 205. Stevens BR, Fernandez A, Hirayama B, Wright EM, Kempner ES. Intestinal brush border membrane Na⁺/glucose cotransporter functions in situ as a homotetramer. *Proc Natl Acad Sci USA* 87: 1456–1460, 1990.
 206. Stumpel F, Burcelin R, Jungermann K, Thorens B. Normal kinetics of intestinal glucose absorption in the absence of GLUT2: evidence for a transport pathway requiring glucose phosphorylation and transfer into the endoplasmic reticulum. *Proc Natl Acad Sci USA* 98: 11330–11335, 2001.
 207. Suzuki T, Fujikura K, Koyama H, Matsuzaki T, Takahashi Y, Takata K. The apical localization of SGLT1 glucose transporter is determined by the short amino acid sequence in its N-terminal domain. *Eur J Cell Biol* 80: 765–774, 2001.
 208. Taglialatela M, Toro L, Stefani E. Novel voltage clamp to record small, fast currents from ion channels expressed in *Xenopus* oocytes. *Biophys J* 61: 78–82, 1992.
 209. Takata K, Kasahara T, Kasahara M, Ezaki O, Hirano H. Immunohistochemical localization of Na⁺-dependent glucose transporter in rat jejunum. *Cell Tissue Res* 267: 3–9, 1992.
 210. Takata K, Kasahara T, Kasahara M, Ezaki O, Hirano H. Localization of Na⁺-dependent active type and erythrocyte/HepG2-type glucose transporters in rat kidney: immunofluorescence and immunogold study. *J Histochem Cytochem* 39: 287–298, 1991.
 211. Taroni C, Jones S, Thornton JM. Analysis and prediction of carbohydrate binding sites. *Protein Eng* 13: 89–98, 2000.
 212. Tarpey PS, Wood IS, Shirazi-Beechey SP, Beechey RB. Amino acid sequence and the cellular location of the Na⁺-dependent D-glucose symporters (SGLT1) in the ovine enterocyte and the parotid acinar cell. *Biochem J* 312: 293–300, 1995.
 213. Tasic V, Slaveska N, Blau N, Santer R. Nephrolithiasis in a child with glucose-galactose malabsorption. *Pediatr Nephrol* 19: 244–246, 2004.
 214. Tazawa S, Yamato T, Fujikura H, Hiratouchi M, Itoh F, Tomae M, Takemura Y, Maruyama H, Sugiyama T, Wakamatsu A, Isogai T, Isaji M. SLC5A9/SGLT4, a new Na⁺-dependent glucose transporter, is an essential transporter for mannose, 1,5-anhydro-D-glucitol, and fructose. *Life Sci* 76: 1039–1050, 2005.
 215. Toggenburger G, Kessler M, Semenza G. Phlorizin as a probe of the small-intestinal Na⁺,D-glucose cotransporter. A model. *Biochim Biophys Acta* 688: 557–571, 1982.
 216. Turk E, Gasymov OK, Lanza S, Horwitz J, Wright EM. A reinvestigation of the secondary structure of functionally active vSGLT, the *Vibrio* sodium/galactose cotransporter. *Biochemistry* 45: 1470–1479, 2006.
 217. Turk E, Kerner CJ, Lostao MP, Wright EM. Membrane topology of the human Na⁺/glucose cotransporter SGLT1. *J Biol Chem* 271: 1925–1934, 1996.
 218. Turk E, Kim O, le Coutre J, Whitelegge JP, Eskandari S, Lam JT, Kreman M, Zampighi G, Faull KF, Wright EM. Molecular characterization of *Vibrio parahaemolyticus* vSGLT: a model for sodium-coupled sugar cotransporters. *J Biol Chem* 275: 25711–25716, 2000.
 219. Turk E, Klisak I, Bacallao R, Sparkes RS, Wright EM. Assignment of the human Na⁺/glucose cotransporter gene SGLT1 to chromosome 22q13. *I Genomics* 17: 752–754, 1993.
 220. Turk E, Martin MG, Wright EM. Structure of the human Na⁺/glucose cotransporter gene SGLT1. *J Biol Chem* 269: 15204–15209, 1994.
 221. Turk E, Wright EM. Membrane topology motifs in the SGLT cotransporter family. *J Membr Biol* 159: 1–20, 1997.
 222. Turk E, Zabel B, Mundlos S, Dyer J, Wright EM. Glucose/galactose malabsorption caused by a defect in the Na⁺/glucose cotransporter. *Nature* 350: 354–356, 1991.
 223. Turner RJ, Moran A. Further studies of proximal tubular brush border membrane D-glucose transport heterogeneity. *J Membr Biol* 70: 37–45, 1982.
 224. Turner RJ, Moran A. Heterogeneity of sodium-dependent D-glucose transport sites along the proximal tubule: evidence from vesicle studies. *Am J Physiol Renal Fluid Electrolyte Physiol* 242: F406–F414, 1982.
 225. Tyagi NK, Goyal P, Kumar A, Pandey D, Siess W, Kinne RK. High-yield functional expression of human sodium/D-glucose cotransporter1 in *Pichia pastoris* and characterization of ligand-induced conformational changes as studied by tryptophan fluorescence. *Biochemistry* 44: 15514–15524, 2005.
 226. Umbach JA, Coady MJ, Wright EM. Intestinal Na⁺/glucose cotransporter expressed in *Xenopus* oocytes is electrogenic. *Bioophys J* 57: 1217–1224, 1990.
 227. Vallon V, Platt KA, Cunard R, Schroth J, Whaley J, Thomson SC, Koepsell H, Rieg T. SGLT2 mediates glucose reabsorption in the early proximal tubule. *J Am Soc Nephrol* 1–36, 2010.
 228. Vayro S, Lo B, Silverman M. Functional studies of the rabbit intestinal Na⁺/glucose carrier (SGLT1) expressed in COS-7 cells: evaluation of the mutant A166C indicates this region is important for Na⁺-activation of the carrier. *Biochem J* 332: 119–125, 1998.
 229. Vayro S, Wood IS, Dyer J, Shirazi-Beechey SP. Transcriptional regulation of the ovine intestinal Na⁺/glucose cotransporter SGLT1 gene. Role of HNF-1 in glucose activation of promoter function. *Eur J Biochem* 268: 5460–5470, 2001.
 230. Veenstra M, Lanza S, Hirayama BA, Turk E, Wright EM. Local conformational changes in the *Vibrio* Na⁺/galactose cotransporter. *Biochemistry* 43: 3620–3627, 2004.
 231. Veenstra M, Turk E, Wright EM. A ligand-dependent conformational change of the Na⁺/galactose cotransporter of *Vibrio parahaemolyticus*, monitored by tryptophan fluorescence. *J Membr Biol* 185: 249–255, 2002.
 232. Veyhl M, Keller T, Gorboulev V, Vernaleken A, Koepsell H. RS1 (RSC1A1) regulates the exocytotic pathway of Na⁺-D-glucose cotransporter SGLT1. *Am J Physiol Renal Physiol* 291: F1213–F1223, 2006.
 233. Veyhl M, Wagner K, Volk C, Gorboulev V, Schmitt BM, Lang F, Koepsell H. Downregulation of the Na⁺-D-glucose cotransporter SGLT1 by protein RS1 (RSC1A1) is dependent on dynamin and protein kinase C. *J Membr Biol* 196: 71–81, 2003.
 234. Veyhl M, Wagner K, Volk C, Gorboulev V, Baumgarten K, Weber WM, Schaper M, Bertram B, Wiessler M, Koepsell H. Transport of the new chemotherapeutic agent beta-D-glucosyliso-phosphoramide mustard (D-19575) into tumor cells is mediated by the Na⁺-D-glucose cotransporter SAAT1. *Proc Natl Acad Sci USA* 95: 2914–2919, 1998.
 235. Voss AA, Diez-Sampedro A, Hirayama BA, Loo DDF, Wright EM. Imino sugars are potent agonists of the human glucose sensor SGLT3. *Mol Pharmacol* 71: 628–634, 2007.
 236. Wang J, Cortina G, Wu SV, Tran R, Cho JH, Tsai MJ, Bailey TJ, Jamrich M, Ament ME, Treem WR, Hill ID, Vargas JH, Gershman G, Farmer DG, Reyen L, Martin MG. Mutant neurogenin-3 in congenital malabsorptive diarrhea. *N Engl J Med* 355: 270–280, 2006.
 237. Washburn WN. Development of the renal glucose reabsorption inhibitors: a new mechanism for the pharmacotherapy of diabetes mellitus type 2. *J Med Chem* 52: 1785–1794, 2009.
 238. Wanatabe A, Choe S, Chaptal V, Rosenberg JM, Wright EM, Grabe M, Abramson J. The mechanism of sodium and substrate release from the binding pocket of vSGLT. *Nature* 468: 988–991, 2010.
 239. Weihua Z, Tsan R, Huang WC, Wu Q, Chiu CH, Fidler IJ, Hung MC. Survival of cancer cells is maintained by EGFR independent of its kinase activity. *Cancer Cell* 13: 385–393, 2008.

240. Wells RG, Pajor AM, Kanai Y, Turk E, Wright EM, Hediger MA. Cloning of a human kidney cDNA with similarity to the sodium-glucose cotransporter. *Am J Physiol Renal Fluid Electrolyte Physiol* 263: F459–F465, 1992.
241. Weyand S, Shimamura T, Yajima S, Suzuki S, Mirza O, Krusong K, Carpenter EP, Rutherford NG, Hadden JM, O'Reilly J, Ma P, Saidijam M, Patching SG, Hope RJ, Norbertszak HT, Roach PC, Iwata S, Henderson PJ, Cameron AD. Structure and molecular mechanism of a nucleobase-cation-sympot-1 family transporter. *Science* 322: 709–713, 2008.
242. Wielert-Badt S, Lin JT, Lorenz M, Fritz S, Kinne RK. Probing the conformation of the sugar transport inhibitor phlorizin by 2D-NMR, molecular dynamics studies, and pharmacophore analysis. *J Med Chem* 43: 1692–1698, 2000.
243. Wood IS, Dyer J, Hofmann RR, Shirazi-Beechey SP. Expression of the Na^+ /glucose co-transporter (SGLT1) in the intestine of domestic and wild ruminants. *Pflügers Arch* 441: 155–162, 2000.
244. Wright EM. Diseases of renal glucose handling. In: *Genetic Diseases of the Kidney*, edited by Lifton R. New York: Elsevier, 2008, p. 1130–1140.
245. Wright EM. Renal Na^+ -glucose cotransporters *Am J Physiol Renal Physiol* 280: F10–F18, 2001.
246. Wright EM, Hirayama BA, Loo DDF. Active sugar transport in health and disease. *J Intern Med* 261: 32–43, 2007.
247. Wright EM, Hirayama BA, Loo DDF, Turk E, Hager K. Intestinal sugar transport. In: *Physiology of Gastrointestinal Tract* (3rd ed.), edited by Johnson E. New York: Raven, 1994, p. 1751–1772.
248. Wright EM, Hirsch JR, Loo DDF, Zampighi GA. Regulation of Na^+ /glucose cotransporters. *J Exp Biol* New York: 200: 287–293, 1997.
249. Wright EM, Loo DDF, Hirayama BA, Turk E. Surprising versatility of Na^+ -glucose cotransporters: SLC5. *Physiology* 19: 370–376, 2004.
250. Wright EM, Martin MG, Turk E. Familial glucose-galactose malabsorption and hereditary renal glycosuria. In: *The Metabolic and Molecular Bases of Inherited Disease*, edited by Scriver CR, Beaudet AL, Sly WS, Valle D, Childs B, Kinzler KW, Vogelstein B. New York: McGraw-Hill, p. 4891–4908.
251. Wright EM, Turk E. The sodium/glucose cotransport family SLC5. *Pflügers Arch* 447: 510–518, 2004.
252. Wright EM, van Os CH, Mircheff AK. Sugar uptake by intestinal basolateral membrane vesicles. *Biochim Biophys Acta* 597: 112–124, 1980.
253. Wright EM, Turk E. The sodium glucose cotransport family SLC5. *Pflügers Arch* 510–518, 2004.
254. Xie Z, Turk E, Wright EM. Characterization of the *Vibrio parahaemolyticus* Na^+ /glucose cotransporter. A bacterial member of the sodium/glucose transporter (SGLT) family. *J Biol Chem* 275: 25959–25964, 2000.
255. Xu B, Lv B, Feng Y, Xu G, Du J, Welihinda A, Sheng Z, Seed B, Chen Y. O-Spiro C-aryl glucosides as novel sodium-dependent glucose co-transporter 2 (SGLT2) inhibitors. *Bioorg Med Chem Lett* 19: 5632–5635, 2009.
256. Yamashita A, Singh SK, Kawate T, Jin Y, Gouaux E. Crystal structure of a bacterial homologue of Na^+/Cl^- -dependent neurotransmitter transporters. *Nature* 437: 215–223, 2005.
257. You G, Lee WS, Barros EJ, Kanai Y, Huo TL, Khawaja S, Wells RG, Nigam SK, Hediger MA. Molecular characteristics of Na^+ -coupled glucose transporters in adult and embryonic rat kidney. *J Biol Chem* 270: 29365–29371, 1995.
258. Yu AS, Hirayama BA, Timbol G, Liu J, Basarab E, Kepe V, Satyamurthy N, Wright EM, Huang SC, Barrio JR. Functional expression of SGLTs in rat brain. *Am J Physiol Cell Physiol* 299: C1277–C1284, 2010.
259. Yu LC, Flynn AN, Turner JR, Buret AG. SGLT-1-mediated glucose uptake protects intestinal epithelial cells against LPS-induced apoptosis and barrier defects: a novel cellular rescue mechanism? *FASEB J* 19: 1822–1835, 2005.
260. Yu LC, Huang CY, Kuo WT, Sayer H, Turner JR, Buret AG. SGLT-1-mediated glucose uptake protects human intestinal epithelial cells against *Giardia duodenalis*-induced apoptosis. *Int J Parasitol* 38: 923–934, 2008.
261. Zagotta WN, Hoshi T, Aldrich RW. Shaker potassium channel gating. III. Evaluation of kinetic models for activation. *J Gen Physiol* 103: 321–362, 1994.
262. Zampighi GA, Kreman M, Boorer KJ, Loo DDF, Bezanilla F, Chandy G, Hall JE, Wright EM. A method for determining the unitary functional capacity of cloned channels and transporters expressed in *Xenopus laevis* oocytes. *J Membr Biol* 148: 65–78, 1995.
263. Zeuthen T. Water-transporting proteins. *J Membr Biol* 234: 57–73, 2010.
264. Zeuthen T, Belhage B, Zeuthen E. Water transport by Na^+ -coupled cotransporters of glucose (SGLT1) and of iodide (NIS). The dependence of substrate size studied at high resolution. *J Physiol* 570: 485–499, 2006.
265. Zeuthen T, Zeuthen E. The mechanism of water transport in Na^+ -coupled glucose transporters expressed in *Xenopus* oocytes. *Biophys J* 93: 1413–1419, 2007.
266. Zhao FQ, Keating AF. Expression and regulation of glucose transporters in the bovine mammary gland. *J Dairy Sci* 90 Suppl 1: E76–E86, 2007.